Theses and Dissertations

Spring 2019

Nanoparticles with Tunable Fluorophobic Effect Towards Multimodal Coassembly with Block Copolymers

Zachary Michael Marsh

NANOPARTICLES WITH TUNABLE FLUOROPHOBIC EFFECT TOWARDS MULTIMODAL COASSEMBLY WITH BLOCK COPOLYMERS

by

Zachary Michael Marsh

Bachelor of Arts
Washington & Jefferson College, 2014

Submitted in Partial Fulfillment of the Requirements

For the Degree of Doctor of Philosophy in

Chemistry

College of Arts and Sciences

University of South Carolina

2019

Accepted by:

Morgan Stefik, Major Professor

Brian Benicewicz, Committee Member

Hui Wang, Committee Member

William Mustain, Committee Member

Cheryl L. Addy, Vice Provost and Dean of the Graduate School

DEDICATION

To my family

ACKNOWLEDGEMENTS

I would like to thank Amrita Sarkar for being my lab mentor and a great friend, your help was invaluable for helping me succeed. I would especially like to thank Kayla Lantz for making this journey a lot easier. You have been so kind and helpful to me and I am lucky to have a friend like you. Lastly, I want to thank Andrew Pingitore, for being by my side for nine years. You are like a brother to me and I could not have done this without you.

Finally, I want to thank my brother Jacob, sister Andrea, grandmother Imogene, and parents Mike and Sandy for your constant love and support. You always believed in me and gave me the will to succeed. Agnes Bucko, I could not have done this without your love and support. I am so grateful for everything you have done for me. I love you.

ABSTRACT

Nanomaterials are often fabricated using block polymers to direct the placement of nanoparticles via selective intermolecular interactions such as hydrogen bonding. Fluorophobic interactions have emerged as a promising handle to control nanoparticle placement independently from typical hydrophilic approaches. A series of nanoparticles with tunable fluorophobicity were prepared to elucidate the key parameters for harnessing fluorophobic interactions in this context. Mixed ligand fluorinated nanoparticles (ML-FNPs) where prepared to examine the competing roles of each ligand towards fluorophobicity and solubility. The ML-FNP intermolecular interactions were first studied using a custom-made Quartz Crystalline Microbalance (QCM) based technique. The ML-FNPs were then examined for compatibility with polymer processing using homopolymers and block copolymers. Strong repulsion of all ML-FNPs was observed in all lipophilic polymer domains while increasing the fluorine content continually enhanced dispersion in the perfluorinated domains. With as little as 25% fluorine in the ligand shell ML-FNPs were assembled in the PFOA domain near the interface, as the fluorine content exceeded 75% the ML-FNPs assembled at the interface and within the center of small PFOA domains. Finally, preliminary experiments combining ML-NPs with hydrophilic NPs led to the first ordered composite film with distinct control over two different NP types.

TABLE OF CONTENTS

LIST OF TABLES

LIST OF FIGURES

LIST OF ABBREVIATIONS

ARGET .... Activator regenerated electron transfer

ATRP .... Atom transfer radical polymerization

DDA .... Dodecylamine

DLS……………………………………………………………Dynamic light scattering

FOA .... Perfluorooctyl acrylate

GISAXS .... Grazing incidence small angle X-ray scattering

GPC………………………………………………………Gel permeation chromatography

H-PFOA .... Homopolyperfluorooctyl acrylate

H-PS .... Homopolystyrene

ML-FNPs .... Mixed ligand fluorinated nanoparticles

NPs .... Nanoparticles

NMR……………………………………………………………Nuclear magnetic resonance

PFOT .... Perfluorooctyl thiol

PEO-*b*-PS-*b*-PFOA .... Poly(ethylene oxide-*block*-styrene-*block*-perfluorooctyl acrylate)

PS-*b*-PFOA .... Poly(styrene-*block*-perfluorooctyl acrylate)

QCM .... Quartz Crystalline Microbalance

SAXS .... Small angle X-ray scattering

TEM .... Transmission electron microscopy

TFT .... α,α,α-Trifluorotoluene

UV-Vis .... Ultraviolet-visible spectroscopy

WAXS .... Wide angle X-ray scattering

CHAPTER 1

OBJECTIVE AND INTRODUCTION

1.1 Research Objective

The ability to control the size and structure of materials on the nanometer length scale is crucial for understanding and controlling the resulting properties. Therefore, having a range of methodologies that enable precision control at these length scales is advantageous for the advancement of nanomaterial research. Bottom up methods rely on the self-assembly of small building blocks to generate larger and more complex structures similar to using the individual letters of the alphabet to create increasingly complex paragraphs.[1] Non-covalent interactions such as hydrogen bonding, hydrophobic interactions, electrostatic interactions, and many others are used to direct the small building blocks during the self-assembly process. Amphiphilic block copolymers have been employed as structure directing agents to cooperatively organize with inorganic building blocks since the 1990's to generate designer materials.[2] Here, hydrophilic interactions have been the sole handle enabling control. In order to expand the capabilities of block copolymer self-assembly towards more complex designer materials another handle must be employed.

The discovery and implementation of a new intermolecular interaction would open the door to Multimodal coassembly. Here, two separate populations of inorganic
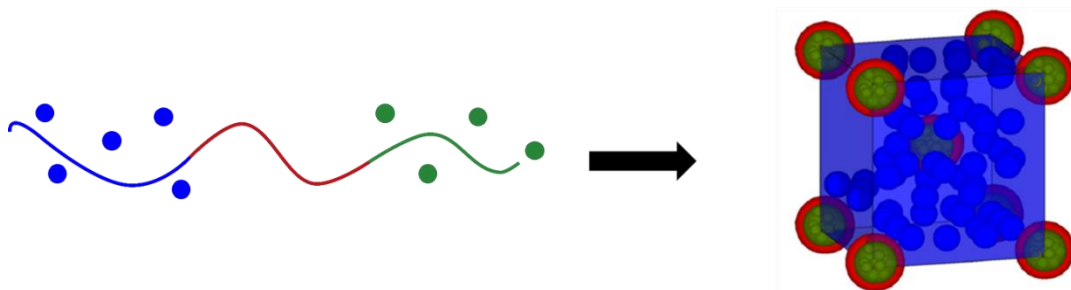
Figure 1.1 Multimodal coassembly of an amphiphilic triblock terpolymer with two populations of inorganic material. Color coding represents chemical dissimilarity.

2

building blocks, such as nanoparticles, could be directed to two distinct polymer domains as shown in Figure 1.1. For this to be possible the new interaction needs to have orthogonality to hydrophilic interactions to avoid cross-loading. In hydrophilic based systems a donor-acceptor approach is used as the acceptor, a hydrophilic polymer block, will "pull" the donor, inorganic nanoparticle, into its domain. One possible design is to utilize a "push" mechanism that does not require a built-in donor-acceptor pairing instead relying on an inherently large mismatch with all but one domain of the amphiphilic block copolymer. The design and implementation of a new coassembly handle utilizing a "push" interaction is the objective for this thesis.

1.2 Background

Amphiphilic block copolymers (BCPs) consist of two or more chemically dissimilar polymer blocks that are linked by a covalent bond. The chemical difference between the blocks produces excess free energy contributions that are unfavorable for mixing. The free energy cost per interaction is normally represented by the interaction parameter (χ).[3] If χ is positive there is an increase in the energy of mixing for each contact between the dissimilar blocks. The more positive the value of χ the more expensive the interaction becomes. If the energy of mixing becomes too expensive the blocks will phase separate to reduce the number of interactions lowering the energy of the system. However, the covalent linkages prevent macrophase separation between the blocks leading to the formation of distinct domains on the nanometer length scale.[3-6] This spontaneous process is referred to as self-assembly since the interactions of the polymer blocks drives the formation of an ordered structure.

Current synthetic methods have enabled high amounts of control over the structure, composition, and architecture of BCPs. Since the dissimilarity between the blocks drives self-assembly controlling the chemistry is crucial. Methods like reversible-addition fragmentation chain transfer polymerization,[7] nitroxide mediated polymerization,[8] atom transfer radical polymerization,[9] and ionic methods allow for numerous functional groups to be incorporated into BCPs. Using these techniques hydrophilic functional groups like ethers, alcohols, acids, esters, and amines can be combined with hydrophobic blocks. The addition of these polar functional groups not only assist in microphase separation as they can increase χ, but they also enable interactions with other materials through strong polar forces. The attractive polar forces have been used to direct and order small organic and inorganic precursors during the BCP self-assembly process. This cooperative self-assembly between the BCP and added small molecules has allowed for the generation of numerous designer organic/inorganic hybrid materials.

For nearly three decades BCP coassembly has been used to generate designer hybrid materials. The first BCP like cooperative self-assembly occurred in 1990 when ammonium surfactants were used to structure the polysilicate kanemite through cation exchange.[10] The ordered composite material was then calcined to generate a porous silica network with small 2-4 nm pores. A similar cation exchange approach with ammonium surfactants was used to generate aluminosilicate structures with 5 nm hexagonally arranged pores.[11] In 1995 neutral poly(ethylene oxide) based surfactants were used to structure silicate precursors into a mesoporous network through hydrogen bonding interactions.[12] This eliminated the need for ionically charged structuring agents providing

4

a general pathway for structuring materials through hydrogen bonding interactions. Although the use of surfactants as structure directing agents was successful it limited the size of the nanocomposite features. Finally, in 1997 poly(isoprene-*block*-ethylene oxide) (PI-*b*-PEO) was used to cooperatively organize aluminosilicates using hydrogen bonding interactions.[2] This was the first time a BCP had been used as a structure directing agent allowing for 20-40 nm features to be obtained. Another important observation was that as the amount of inorganic was increased the resulting morphology of the nanocomposite changed from a hexagonal to a lamellar phase. Thus, the term coassembly was adopted as the resulting structure was determined by the BCP and amount of inorganic material.

In the following years BCPs were used to order numerous inorganic and organic materials. An amphiphilic PEO based triblock copolymer was used to generate mesoporous silicon oxide with uniform 30 nm pores.[13] This was more than three times the pore size achieved using surfactants as structuring agents. Until 1998 silicate or aluminosilicates were the only inorganic material used in the coassembly process until Stucky *et. al.* generated the first porous transition metal oxides from BCPs.[14] Utilizing hydrogen bonding interactions with the PEO block, metal oxides of zirconium, titanium, tantalum, niobium, tungsten, and tin were coassembled using the same general procedure. The use of metal oxides in the coassembly process has since been expanded to multi-metal oxide systems due to greater control over the condensation kinetics of sol-gel processes.[15,16]

As BCP coassembly grew as a tool for structuring small building blocks carbon precursors were added to the mix. In 2004 a poly(styrene-*block*-4-vinylpyridine) (PS-*b*-P4VP) BCP was combined with a resorcinol-formaldehyde (RF) resin to generate large-

5

scale crack-free mesoporous carbon films with 30 nm pores.[17] The resorcinol hydrogen bonded to the P4VP block during self-assembly to form a hexagonally structured BCP film that was exposed to formaldehyde gas inducing polymerization of the RF resin inside the P4VP domain. Remarkably, the RF resin formation did not disrupt the hexagonal structure and was able to be carbonized to form a free-standing mesoporous film up to 6cm^2. Similar strategies using PEO based triblock copolymers and phenolic resins were able to generate a family of high surface area mesoporous carbons with lamellar, hexagonal, cubic, and 3D bicontinuous network structures.[18,19]

The methodologies of BCP coassembly developed with inorganic and organic precursors was combined in 2006 for the first triconstituent coassembly.[20] A PEO based triblock copolymer was mixed with organosilicate precursors and phenolic resins to generate heterogeneous mesoporous nanocomposites. The strong hydrogen bonding interactions between the hydrogen bond acceptor (PEO) and the donor (silica/resin) favored the formation of an ordered nanocomposite without the expulsion of either precursor. The film could then be calcined to form a carbon-silica nanocomposite with ~7 nm pores. The nanocomposite could then undergo combustion or acid etching to selectively remove the carbon or silica, respectively. This study had shown that BCPs could structure multiple inorganic or organic materials cooperatively. Thus, opening the door to more complex and advanced nanomaterials.

Metal nanoparticles (NPs) were then introduced as another building block that could successfully coassemble with BCPs. In 2008 platinum NPs were coassembled with a poly(isoprene-*block*-dimethylaminoethyl methacrylate) (PI-*b*-PDMAEMA) BCP to generate nanocomposites containing platinum loadings as high as 79%.[21] The platinum

NPs were stabilized using thiols functionalized with ammonium surfactants making them highly hydrophilic which directed them to the hydrophilic PDMAEMA block. Once the NPs and PDMAEMA coassembled the amine functional group of the PDMAEMA block would bind to the platinum freezing the NP in place.[22] The nanocomposites were then pyrolyzed to form free-standing mesoporous platinum with carbon. Before this study metal NPs had been coassembled with BCPs but none were able to achieve high metal loadings making free-standing metal structures unattainable. Most metal NPs were insoluble in the BCP systems or had weak interactions. If NPs were soluble large bulky ligands that restricted the volume fraction of the metal to under 3% were used.[23] This highlighted the need for NPs stabilized with small ligands that promote strong interactions with the BCP. Watkins *et. at.* used a similar approach with PEO to coassemble gold and silica nanoparticles in the same domain.[24] By using small thiol ligands functionalized with alcohols and amines which act as hydrogen bond donors BCPs with a hydrogen bond acceptor could be used. Thus, simpler block copolymer systems that utilized the same hydrogen bonding interactions implemented in previous coassembly studies could be used.

To this point all BCP coassembly had used diblock or triblock systems with only two unique polymer blocks. This limited the nanocomposites to two polymer domains and a handful of possible nanostructures. The first triblock terpolymer with three unique polymer blocks was introduced in 2009.[25] A poly(isoprene-*block*-styrene-*block*-ethylene oxide) (PI-*b*-PS-*b*-PEO) BCP was coassembled with aluminosilicate or niobia NPs to form highly ordered nanocomposites with three distinct polymer domains. Four morphologies were obtained including a core-shell hexagonal, core-shell double gyroid,

7

three-domain lamellae, and an inverse core-shell hexagonal structure. The same PI-*b*-PS-*b*-PEO BCP was coassembled with niobia and titania NPs to form multiple networked morphologies that could be transformed into mesoporous materials by removal of the BCP one of which was chiral.[26] These studies show the complex and unique nanostructured materials that can be formed by using a BCP with three distinct domains.

The control over composition, structure, and size enabled by BCP coassembly is remarkable. Even more astonishing is the fact that all of the previously described research has been accomplished with a single intermolecular interaction. All have used hydrophilic interactions between a BCP and the small building blocks, mainly hydrogen bonding. In these systems there is a donor-acceptor pairing that pulls the two materials together. This donor-acceptor system is still used successfully for the development of new nanomaterials today. However, over the three decades of research into BCP coassembly an intermolecular interaction that does not rely on hydrophilic systems has yet to be employed successfully. Although, triconstituent coassembly has enabled control over two populations of building blocks with a BCP both have the same hydrophilic chemistry and are loaded into the same polymer domain.[20] If this approach was applied to a triblock terpolymer system with three distinct polymer domains the added building blocks would still be limited to only the hydrophilic polymer domain. Thus, control over multiple materials with different chemistries is unattainable.

The implementation of hydrophobic interactions as a handle for BCP coassembly has been attempted. Metal nanoparticles coated with long chain alkyl thiols or grafted polymer chains have been combined with BCPs generating ordered structures. Smaller alkyl ligands have resulted in macrophase separation of the NPs and no dispersion in the

8

polymer matrix.[27] The need for sizable stabilizing ligands has restricted the volume fraction of the metal in the nanocomposite which is crucial for material development.[21] For example gold NPs were assembled with a BCP containing no hydrophilic block by using alkyl thiols that are 18 carbons in length.[28] The NPs were incorporated but all were found at the interface signaling a mismatch between the NP and BCP. The use of polymer grafted NPs has enabled greater compatibilization as the grafted polymer is often the same chemistry as one of the polymer blocks. Utilizing thiol functionalized PS ligands gold NPs were successfully coassembled with a poly(styrene-*block*-2 vinylpyridine) BCP.[29] The NPs were found assembling in the PS domain and away from the interface indicating a successful match. However, the greatest inorganic loading achieved was 0.32 volume % which is far too low for metal NP loading.[21]

Another approach to enable greater control over assembling alkyl thiol stabilized NPs with BCPs utilizes small molecule additives.[30] Here, cadmium-selenide and lead-sulfide NPs stabilized with alkyl thiol ligands, 18 carbons in length, were blended with a PS-*b*-P4VP BCP and 3-n-pentadecylphenol (PDP), a small molecule with hydrogen bonding capabilities. Both NPs were aligned into lamellae or hexagonal structures with inorganic volume fractions up to 7 volume %. However, the NPs were not truly assembling into the BCP domains. The small PDP molecules were added to generate a hydrogen bonding network with the P4VP block. The hydrophobic pentadecyl chains of PDP phase separated generating a microdomain inside the P4VP block. The NPs were then segregated to this domain during assembly of the BCP. If the PDP was removed from the system macrophase separation and aggregation of the metal NPs was observed. In 2015 this approach was employed again to assemble 1-dodecane thiol stabilized gold

9

NPs up to 70 volume % in the same PS-*b*-P4VP BCP.[31] This was the first time a small alkyl ligand was used in BCP coassembly as 1-dodecane thiol is just 10 carbons in length. However, without significant concentrations of the hydrogen bonding PDP the NPs aggregated as described previously. Therefore, this approach relies on hydrogen bonding interactions to overcome the mismatch of hydrophobic NPs with BCPs. This further indicates that hydrophobic interactions alone are not selective enough for coassembly. It also highlights the inherent mismatch of hydrophobic ligands with hydrophobic BCP domains.

The large volume of work promoting BCP coassembly has discovered four main criteria crucial to the process. First, the inorganic/organic building block must be soluble in common solvent systems. Without high solubility the building blocks cannot be combined with the BCP system. Second, the building block must have selective interactions with one block of the BCP. Hydrogen bonding has met this criterion as the donor-acceptor "pull" system is strong and selective while hydrophobic interactions fail here. Third, if an inorganic molecule is added the ligands used to stabilize it must remain small to increase the volume of metal added to the system. If a large organic ligand is used it will lower the amount of inorganic in the final nanostructure.[21] Finally, the building block used must be small enough to be incorporated into the selected block of the BCP. If the building block has a large diameter it may induce chain stretching as it is assembled. Chain stretching is entropically unfavorable leading to an increase in the total energy. In these cases, the BCP will expel the building block to reduce chain stretching leading to aggregation and disruption of the BCP self-assembly.[32] If another

intermolecular interaction is to be deployed as a handle to control BCP coassembly simultaneously with the hydrophilic interactions it must meet the four major criteria.

The design of a new interaction begins with orthogonality to hydrogen bonding. Coassembly relies on the unfavorable interactions between chemically dissimilar polymer blocks. Hydrophobic interactions were the first logical step as amphiphilic block copolymer systems have largely utilized a hydrophilic-*block*-hydrophobic structure to facilitate self-assembly. One possible solution is to create a greater mismatch in the chemistry used by utilizing fluorinated materials. The addition of fluorine into BCPs has enabled the creation of incredibly high χ systems. Even low molecular weight BCPs that contain a hydrophobic block and a fluorinated block have exhibited strong microphase separation.[33] Fluorinated materials are amphiphobic meaning they strongly phase separate from both hydrophilic and lipophilic materials. This behavior has been deemed the fluorophobic effect. The usage of the fluorophobic effect alongside hydrophilic blocks would create orthogonality.

This can be represented through the Hildebrand solubility parameter (δ) which is a representation of a material's chemical energy. Using the δ of common materials an approximation of χ can be made as the greater difference in δ resulting in an increase in χ. A simple example showcasing the amphiphobic nature of fluorinated materials is shown in Figure 1.2. Hydrophilic materials are represented by the common polymer block PEO which has a $\delta \sim 20$. Lipophilic materials are represented by PS which has a $\delta \sim 18$. PEO-*b*-PS is a common BCP that does self-assemble and has been used for coassembly. Fluorinated materials are represented by poly(tetrafluoroethylene) (PTFE) which has a $\delta \sim$ 12.7. That translates to a very large difference in δ and χ for PTFE with PS and especially

11

PEO. Although PTFE is not used in BCPs all fluorinated materials have been shown to have incredibly low energies and fluorinated polymer blocks have been shown to have a very large χ with common polymer blocks like PS.[33,34] Therefore, fluorinated BCPs should self-assemble and fluorinated building blocks should be strongly repelled from hydrophilic domains through the fluorophobic effect making them orthogonal to hydrogen bonding.

With orthogonality to hydrogen bonding rationalized through the fluorophobic effect the four criteria of coassembly can be discussed. The most important criterion is the selective intermolecular interaction. This was the downfall of hydrophobic
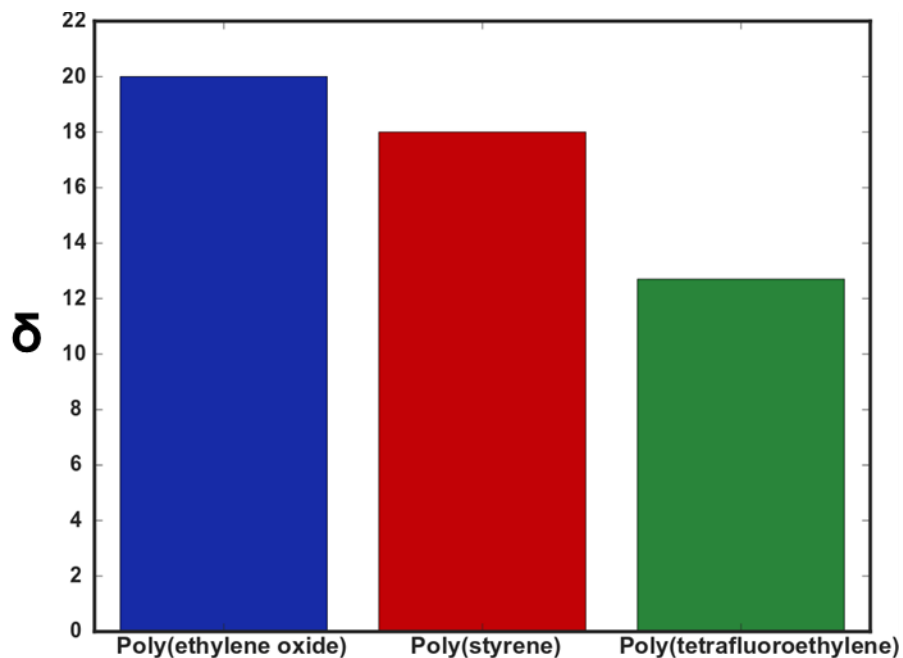
Figure 1.2 Hildebrand solubility parameter of three polymer blocks with blue representing hydrophilic, red representing lipophilic, and green representing fluorophilic, respectively.

interactions as the lack of a donor-acceptor "pull" system and the minimal repulsion or "push" force lead to aggregation and non-dispersion. The fluorophobic effect would also lack the donor-acceptor pairing found with hydrogen bonding. However, the strong phase

separation, or "push", of fluorinated materials has been used in the past to assemble large systems with minimal fluorine content. In 2008 the phase separation of a small 7 carbon alkyl tail containing 15 fluorine atoms was enough to pull together two immiscible homopolymers that normally show macrophase separation.[35] The strong segregation of the fluorinated tails form the homopolymers caused a blend of 20,000 g/mol PS and 20,000 g/mol poly(*n*-butyl methacrylate) (PnBMA) to exhibit BCP like behavior forming a lamellar structure. Without the small fluorinated tails, the PS and PnBMA would de-mix similar to oil in water. Similarly, perfluorinated gold NPs were combined with modified sugar molecules containing a small fluorinated tail making them soluble in aqueous media.[36] The addition of the fluorinated tail on the sugar induced phase separation forcing the tail to associate with the ligands on the NPs. As the fluorinated tails and ligands were pushed to the same domain the sugar molecules encapsulate the NPs making them soluble in water. The strong segregation of the fluorinated materials from the hydrophilic sugar and water enabled mixing of the system. These examples highlight the repulsion of the fluorophobic effect being used to associate fluorinated materials. Thus, the "push" of the fluorophobic effect should be selective and allow the fluorinated building blocks to assemble with the fluorinated block of the BCP.

The second criterion of using small organic ligands would also be met. The previous examples used small 7-8 carbon long fluorinated molecules to induce phase separation through the fluorophobic effect. This strategy could be used to synthesize metal NPs stabilized with small 7-8 carbon fluorinated thiols. These small ligands would facilitate coassembly while maintaining a high metal percentage. Synthetic routes affording ~2 nm perfluorinated gold NPs with moderate control over the size dispersity

exist.[37] Thus, the third criterion requiring a small diameter to avoid unfavorable chain stretching is also met. The fourth and final criterion needed for BCP coassembly is the solubility of the building blocks in common organic systems. All of the promising aspects of the fluorophobic effect rely on the immiscibility with both hydrophilic and lipophilic materials. This represents a large hurdle as fluorinated metal NPs are insoluble in most solvent systems. If multimodal coassembly is to be attained with the fluorophobic effect the solubility of fluorinated materials must be improved.

One possible solution is through mixed ligand shells containing perfluorinated thiols. The ligand shell is the ultimate interface with the local environment and NP behavior is largely determined by the ligand shells interactions with its surroundings. By incorporating two chemically dissimilar ligands the behavior of the NP can be tuned. For example, NPs containing mixtures of hydrophilic ligands with fluorinated thiols have shown solubility in water.[38] Here, long hydrophilic ligands and short fluorinated ligands were employed to enable solubility. However, the fluorine content in the system needed to be kept near 10% to avoid aggregation. Similar approaches have enabled solubility in organic media and a variety of aqueous environments.[39,40] For coassembly a mixture of alkyl and fluorinated thiols could be used to increase solubility while maintaining orthogonality to hydrogen bonding. This would be a powerful tool enabling fine tuning of the NP properties and precise control over the behavior. However, the chemistry of the ligand shell alone cannot explain the volume of behavior observed with mixed ligand shell NPs (ML-NPs).

Similar to BCP systems mixed ligand shells containing dissimilar ligands exhibit phase separated domains. This behavior was first observed for thiol mixtures on a flat

14

surface which formed separated islands to reduce the number of unfavorable interactions.[41] Despite the high surface curvature of a metal NP phase separation can occur in a similar fashion. In fact, the curvature has been shown to influence how phase separation occurs leading to domain structures not possible on a flat film. This was observed in 2004 when ripple-like structures were found on the surface of a metal NP.[42] The ripple-like structures were found when the ratio of the ligands was nearly equivalent and disappeared when the composition was adjusted to a majority of one ligand. This discovery was highly debated as the formation of ripple-like morphology would increase the interface between the two ligands coinciding with an increase in the overall energy. If the number of interactions alone influenced phase separation the domains on the NP surface would have been Janus-like as the interface would be reduced.

The debate over morphology formation in ML-NPs continued until the factors influencing non-enthalpy mediated phase separation were determined. Theoretical studies of ML-NPs determined that ripple, now referred to as stripes, formation is a factor of the surface curvature, chemical dissimilarity, and ligand length.[43] The NP must have a mixture of ligands chemically dissimilar enough to promote phase separation. The NP must also have fairly high surface curvature with an optimal range generated with NPs between 2-8 nm in diameter. Lastly, the ligands in the ligand shell must have a 4-6 carbon difference. This turned out to be the main determining factor for stripe formation in the ligand shell. If one ligand is taller than it has greater tail mobility. By forming striped or stripe-like domains the interface between the two ligands grows creating an increase in the amount of free volume. The increased free volume allows the taller ligands to have even greater mobility. This leads to a gain in the conformational entropy

15

of the system which leads to a minimization in the energy. The gain in conformation entropy lead to a lower energy system than if bulk phase separation occurred.

In the following years research on ML-NP morphology formation and its impact on the behavior of the NP rapidly increased. Using the information provided by theoretical methods Stellacci *et al.* synthesized ML-NPs that formed stripe-like domains.[44] The behavior of the NPs was then probed using concentration studies in a range of solvents with differing chemistries and shapes. The stripe-like domains were found to influence the behavior in a non-monotonic fashion as NPs with 67% of the ligand shell being hydrophobic were most soluble in polar alcohols. The term non-monotonic is used to describe behavior that deviates from a thin film of mixed ligands on a flat substrate.[45] Work of adhesion measurements of mixed monolayers on a flat gold surface show a monotonic increase in the work of adhesion as the amount of hydrophilic ligand is increased. Measurements of ML-NPs show non-monotonic behavior with large increases in work of adhesion until a decrease when the amount of hydrophilic ligand reached 50%. The work of adhesion exhibited another significant decrease when 83% of the ligand shell was composed of the hydrophilic ligand. This behavior is hypothesized to be a mixture of two competing mechanisms termed cavitation and confinement.[45] Cavitation is the encapsulation by solvent molecule of a solvophobic solute within a solvent cage. The solvophilic ligands will pull the solvent to the surface of the ligand shell while the solvophobic ligand will push the solvent away. Cavitation mainly relates to the width of the solvophobic domains, if the domains are large the interactions with the solvent will decrease as it is actively repelled from the ligand shell. Confinement relates to the width of the solvophilic domains and the conformational entropy of the solvent. If

16

the width of the solvophilic domain is small, then the solvent trying to enter the domain will have restricted movement. This decreases the conformational entropy of the solvent leading to repulsion from the domain. The balance of these two mechanisms is still difficult to predict as it will be unique for every ligand mixture and local environment. Therefore, methods to determine the morphology of the ligand shell and the resulting behavior with the local environment are needed.

Currently numerous methods are available for determining the morphology of the ligand shell. Electron microscopy methods have been employed though the accuracy is still debated.[44,46,47] Nuclear magnetic resonance (NMR) spectroscopy methods have also been used in the determination of the morphology as it is highly sensitive to the local environment of the ligands.[48] This has further been expanded to nuclei like fluorine which has a more intense signal and greater resolution due to the large chemical shift window.[49] Mass spectroscopy and MALDI-TOF have been used to detect NP fragments which have a characteristic mass depending on the mixture of ligands on the fragments.[50,51] These methods rely on fragmenting the NPs as a Janus particles fragments will mainly be fragments containing only one type of ligand, patchy particles will have a large population of similar fragments with an increase of mixed ligand fragments due to the slight increase in the interface, and stripe-like particles will mainly be fragments containing mixtures of ligands due to the large interface on the ML-NP. The most recent method utilizes small angle neutron scattering to determine the structure of the ligand shell.[52] However, deuterated ligands and access to a neutron line are needed for this method so it is not viable for most studies.

The largest limitation in the field of ML-NP research is the lack of quantitative methods that can determine the interactions with the local environment. Common solubility measurements are often used although these are tedious and require each ML-NP be dispersed in a large array of solvents. The ML-NPs are then left in solution for a week and analyzed using UV-Vis to determine the concentration of solvated ML-NPs.[44] Work of adhesion experiments have also been used to determine the interactions of the ML-NPs. These methods use contact angle measurements and AFM to measurement the work of adhesion of various solvents.[45] Currently these are the few tools available to determine the interactions of ML-NPs. The development of quantitative and easy tools to analyze the interactions of ML-NPs is needed.

1.3 Outlook

The success of BCP coassembly has allowed for the development of numerous nanomaterials ranging from mesoporous carbons to bicontinuous transition metal oxide networks. All have relied on the strength of a donor-acceptor pairing to direct the building block to the desired polymer domain. Using this design handle materials like platinum, cadmium-selenide, titania, niobia, silica, tungsten, and many more have been ordered into hexagonal, lamellar, bicontinuous networks, and even core-shell versions of the structures listed. One cannot deny the usefulness of this strong "pull" interaction in the field of BCP coassembly. However, hydrogen bonding interactions can only control added materials to a single polymer phase. This is most apparent in triconstituent coassembly where multiple materials can be directed but all go to the same hydrophilic domain. If one is to control two materials and selectively direct to two different domains another interaction is needed. Fluorophobic interactions are a promising choice for filling

18

the current void in BCP coassembly. To do this the interactions of fluorinated BCPs and fluorinated NPs would need to be investigated and the largest obstacle of insolubility would need to be overcome.

The primary goal of this thesis is to develop and implement the fluorophobic effect as a new interaction for BCP coassembly. To accomplish this the insolubility of fluorinated materials will need to be overcome while maintaining the strength of the fluorophobic effect. To this end, mixed ligand fluorinated nanoparticles (ML-FNPs) with short perfluorinated thiol and long alkyl thiol ligands will be synthesized to simultaneously tune the solubility and fluorophobicity. The behavior of these ML-FNPs will be influenced by the chemical composition and morphology of the ligand shell and will need to be determined in both small molecule and polymeric environments. We hypothesize that the combination of a short-fluorinated ligand and a long lipophilic ligand will form stripe-like domains. The morphology of the ligand shell will largely determine the ability to disperse the ML-FNPs in fluorinated homopolymers and coassemble with fluorinated BCPs.

In chapter 2 the synthesis and characterization of the ML-FNPs will be discussed. Using a ligand exchange approach a series of ML-FNPs with varying fluorine content in the ligand shell were synthesized. The chemical composition and ligand density were determined through quantitative ^{1}H NMR measurements. An in-depth explanation of utilizing ^{19}F NMR to determine the morphology of ML-FNPs will be presented followed by an evaluation of the ML-FNPs synthesized. Finally, we present a new quartz crystal microbalance (QCM) approach to quantify the interactions of the ML-FNPs. Using the new QCM based method the behavior of the ML-FNPs as a function of fluorine content

was determined and found to be highly non-monotonic. At low (%F < 30) and high (%F > 70) fluorine content we form patchy morphologies and observe an increase in the amount of interactions will all molecules tested. At moderate fluorine content (30 < %F < 70) we form stripe-like domains and see a decrease in the amount of interactions with all of the molecules tested. These results suggest that the patchy and stripe-like morphologies formed in the ligand shell have significant impacts on the interactions of the ML-FNPs. More importantly the new QCM method developed is a tool for the wider NP community that is currently lacking quantitative methods of determining the interactions of ML-NPs.

In chapter 3 the dispersion and coassembly of the ML-FNPs will be discussed as a function of fluorine content in the ligand shell. A series of polymers were synthesized for the dispersion experiments to probe the fluorophobic effect. A fluorinated poly(perfluorooctyl acrylate) (PFOA) and a non-fluorinated PS homopolymer were combined with the series of ML-FNPs at various loading percentages to determine the dispersion capabilities. The quality of the dispersion was determined by the presence of a structure factor peak by SAXS. SAXS experiments show that even small fluorine content aggregates the ML-FNPs in the PS homopolymer as a structure factor is observed even at the lowest loadings. In the PFOA all of the ML-FNPs with fluorine in the ligand shell disperse at low loading content. As the amount of fluorine is increased form factor signals are observed even at the highest loading percentage suggesting that the composition not the morphology determines the strength of the fluorophobic effect. Coassembly experiments of the ML-FNPs with a PS-*b*-PFOA BCP show successful assembly with small fluorinated ligands by SAXS and TEM. TEM shows the ML-FNPs

do not aggregate unlike systems utilizing hydrophobic forces with small hydrophobic ligands. The images show the ML-FNPs were pushed from the PS domain and into the PFOA domain as fluorine content was added to the ligand shell. It was also determined that ML-FNPs with higher fluorine content assembled within the PFOA domain and not at the interface further confirming the composition not morphology determined the strength of the fluorophobic effect. Overall these experiments show that the fluorophobic effect can be used to coassembled fluorinated materials.

Lastly, the first ever multimodal coassembly experiment was attempted using the fluorophobic effect in tandem with hydrogen bonding interactions. To do this an amphiphilic PEO-*b*-PS-*b*-PFOA BCP was combined with titania NPs that would be coassembled to the PEO domain through hydrogen bonding interactions and the ML-FNPs that would be coassembled using the fluorophobic effect. The 75F-NPs were chosen as the QCM studies determined these patchy particles have enhanced interactions with small molecules and the dispersion/coassembly experiments revealed the fluorine content was sufficient to induce assembly. These preliminary experiments are promising toward attaining multimodal coassembly.

1.4 References

1. Zhang, S. *Mater. Today* 2003, 6 , 20–27.

2. Templin, M.; Franck, A.; Du Chesne, A.; Leist, H.; Zhang, Y.; Ulrich, R.; Schädler, V.; Wiesner, U. *Science* **1997**, *278*, 1795–1798.

3. Bates, F. S.; Fredrickson, G. H. *Phys. Today* **1999**, *52*, 32–38.

4.Thomas, E. L.; Anderson, D. M.; Henkee, C. S.; Hoffman, D. *Nature* **1988**, *34*, 598–601.

4. Bates, F. S. *Science* **1991**, *251*, 898–905.

5. Matsen, M. W.; Schick, M. *Phys. Rev. Lett.* **1994**, *72*, 2660–2663.

6. Matesen, M. W.; Bates, F. S. *Macromolecules* **1996**, *29*, 1091–1098.

7. Keddie, D. J. *Chem. Soc. Rev.* **2014**, 43, 496–505.

8. Hawker, C. J.; Bosman, A. W.; Harth, E. *Chem. Rev.* **2001**, *101*, 3661–3688.

9. Matyjaszewski, K.; Xia, J. *Chem. Rev.* **2001**, *101*, 2921–2990.

10. Yanagisawa, T.; Shimizu, T.; Kuroda, K.; Kato, C. *Bull. Chem. Soc. Jpn.* **1990**, *63*, 988–992.

11. Beck, J. S.; Vartuli, J. C.; Roth, W. J.; Leonowicz, M. E.; Kresge, C. T.; Schmitt, K. D.; Chu, C. T. W.; Olson, D. H.; Sheppard, E. W.; McCullen, S. B.; Higgins, J. B.; Schlenker, J. L. *J. Am. Chem. Soc.* **1992**, *114*, 10834–10843.

12. Bagshaw, S. A.; Prouzet, E.; Pinnavaia, T. J. *Science* **1995**, *269*, 1242–1244.

13. Zhao, D.; Feng, J.; Huo, Q.; Melosh, N.; Fredrickson, G. H.; Chmelka, B. F.; Stucky, G. D. *Science.* **1998**, *279*, 548-552.

14. Yang, P.; Zhao, D.; Margolese, D. I.; Chmelka, B. F.; Stucky, G. D. *Nature* **1998**, *396*, 152.

15. Fan, J.; Boettcher, S. W.; Stucky, G. D. *Chem. Mater.* **2006**, *18*, 6391–6396.

16. Boettcher, S. W.; Fan, J.; Tsung, C.-K.; Shi, Q.; Stucky, G. D. *Acc. Chem. Res.* **2007**, *40*, 784–792.

17. Liang, C.; Hong, K.; Guiochon, G. A.; Mays, J. W.; Dai, S. *Angew. Chem. Int. Ed.* **2004**, *43*, 5785–5789.

18. Meng, Y.; Gu, D.; Zhang, F.; Shi, Y.; Cheng, L.; Feng, D.; Wu, Z.; Chen, Z.; Wan, Y.; Stein, A.; Zhao, D. *Chem. Mater.* **2006**, *18*, 4447–4464.

19. Wan, Y.; Shi, Y.; Zhao, D. *Chem. Mater.* **2008**, *20*, 932–945.

20. Liu, R.; Shi, Y.; Wan, Y.; Meng, Y.; Zhang, F.; Gu, D.; Chen, Z.; Tu, B.; Zhao, D. *J. Am. Chem. Soc.* **2006**, *128*, 11652–11662.

21. Warren, S. C.; Messina, L. C.; Slaughter, L. S.; Kamperman, M.; Zhou, Q.; Gruner, S. M.; DiSalvo, F. J.; Wiesner, U. *Science* **2008**, *320*, 1748–1753

22. Li, Z.; Sai, H.; Warren, S. C.; Kamperman, M.; Arora, H.; Gruner, S. M.; Wiesner, U. *Chem. Mater.* **2009**, *21*, 5578–5584.

23. Warren, S. C.; Banholzer, M. J.; Slaughter, L. S.; Giannelis, E. P.; DiSalvo, F. J.; Wiesner, U. B. *J. Am. Chem. Soc.* **2006**, *128*, 12074–12075.

24. Lin, Y.; Daga, V. K.; Anderson, E. R.; Gido, S. P.; Watkins, J. J. *J. Am. Chem. Soc.* **2011**, *133*, 6513–6516.

25. Stefik, M.; Mahajan, S.; Sai, H.; Epps, T. H.; Bates, F. S.; Gruner, S. M.; DiSalvo, F. J.; Wiesner, U. *Chem. Mater.* **2009**, *21*, 5466–5473.

26. Stefik, M.; Wang, S.; Hovden, R.; Sai, H.; Tate, M. W.; Muller, D. A.; Steiner, U.; Gruner, S. M.; Wiesner, U. *J. Mater. Chem.* **2012**, *22*, 1078–1087.

27. Balazs, A. C.; Emrick, T.; Russell, T. P. *Science.* **2006**, *314*, 1107–1111.

28. Bockstaller, M. R.; Lapetnikov, Y.; Margel, S.; Thomas, E. L. *J. Am. Chem. Soc.* **2003**, *125*, 5276–5277.

29. Chiu, J. J.; Kim, B. J.; Yi, G.-R.; Bang, J.; Kramer, E. J.; Pine, D. J. *Macromolecules* **2007**, *40*, 3361–3365.

30. Zhao, Y.; Thorkelsson, K.; Mastroianni, A. J.; Schilling, T.; Luther, J. M.; Rancatore, B. J.; Matsunaga, K.; Jinnai, H.; Wu, Y.; Poulsen, D.; Fréchet, J. M. J.; Paul Alivisatos, A.; Xu, T. *Nat. Mater.* **2009**, *8*, 979.

31. Kao, J.; Xu, T. *J. Am. Chem. Soc.* **2015**, *137*, 6356–6365.

32. Warren, S. C.; DiSalvo, F. J.; Wiesner, U. *Nat. Mater.* **2007**, *6*, 156–161.

33. Hillmyer, M. a.; Lodge, T. P. *J. Polym. Sci. Part A Polym. Chem.* **2002**, *40*, 1–8.

34. Berger, R.; Resnati, G.; Metrangolo, P.; Weber, E.; Hulliger, J. *Chem. Soc. Rev.* **2011**, *40*, 3496–3508.

35. Shen, J.; Hogen-Esch, T. *J. Am. Chem. Soc.* **2008**, *130*, 10866–10867.

36. Chen, Z.; Chen, G. *Chinese J. Chem.* **2013**, *31*, 695–700.

37. Dass, A.; Guo, R.; Tracy, J. B.; Balasubramanian, R.; Douglas, A. D. Murray, R. J. *Langmuir* **2008**, *1995*, 310–315.

38. Niu, H.; Wang, S.; Zhou, Z.; Ma, Y.; Ma, X.; Cai, Y. *Anal. Chem.* **2014**, *86*, 4170–4177.

39. Uzun, O.; Hu, Y.; Verma, A.; Chen, S.; Centrone, A.; Stellacci, F. *Chem. Commun.* **2008**, *2*, 196–198.

40. Bidoggia, S.; Milocco, F.; Polizzi, S.; Canton, P.; Saccani, A.; Sanavio, B.; Krol, S.; Stellacci, F.; Pengo, P.; Pasquato, L. *Bioconjugate Chem.* **2017**, *28*, 43–52.

41. Stranick, S. J.; Parikh, A. N.; Tao, Y. T.; Allara, D. L.; Weiss, P. S. *J. Phys. Chem.* **1994**, *98*, 7636–7646.

42. Jackson, A. M.; Myerson, J. W.; Stellacci, F. *Nat. Mater.* **2004**, *3*, 330–336.

43. Singh, C.; Ghorai, P. K.; Horsch, M. A.; Jackson, A. M.; Larson, R. G.; Stellacci, F.; Glotzer, S. C. *Phys. Rev. Lett.* **2007**, *99*, 1–4.

44. Centrone, A.; Penzo, E.; Sharma, M.; Myerson, J. W.; Jackson, A. M.; Marzari, N.; Stellacci, F. *Proc. Natl. Acad. Sci. U. S. A.* **2008**, *105*, 9886–9891.

45. Kuna, J. J.; Voïtchovsky, K.; Singh, C.; Jiang, H.; Mwenifumbo, S.; Ghorai, P. K.; Stevens, M. M.; Glotzer, S. C.; Stellacci, F. *Nat. Mater.* **2009**, *8*, 837–842.

46. Hu, Y.; Wansch, B. H.; Sahni, S.; Stellacci, F. *J. Scanning Probe Microsc.* **2009**, *4*, 24–35.

47. Centrone, A.; Hu, Y.; Jackson, A. M.; Zerbi, G.; Stellacci, F. *Small* **2007**, *3*, 814–817.

48. Pradhan, S.; Brown, L. E.; Konopelski, J. P.; Chen, S. *J. Nanopart. Res.*, **2009**, *11*, 1895-1903.

49. Şologan, M.; Marson, D.; Polizzi, S.; Pengo, P.; Boccardo, S.; Pricl, S.; Posocco, P.; Pasquato, L. *ACS Nano* **2016**, *10*, 9316–9325.

50. Harkness, K. M.; Balinski, A.; McLean, J. A.; Cliffel, D. E. *Angew. Chem. Int. Ed.* **2011**, *50*, 10554–10559.

51. Luo, Z.; Hou, J.; Menin, L.; Ong, Q. K.; Stellacci, F. *Angew. Chem. Int. Ed.* **2017**, *56*, 13521–13525.

52. Luo, Z.; Marson, D.; Ong, Q. K.; Loiudice, A.; Kohlbrecher, J.; Radulescu, A.; Krause-Heuer, A.; Darwish, T.; Balog, S.; Buonsanti, R.; Svergun, D. I.; Posocco, P.; Stellacci, F. *Nat. Commun.* **2018**, *9*, 1343.

CHAPTER 2

QCM DETECTION OF MOLECULE-NANOPARTICLE INTERACTIONS FOR LIGAND SHELLS OF VARYING MORPHOLOGY[1]

Marsh, Z. M.; Lantz, K. A.; Stefik, M. QCM Nanoscale 2018, 10, 19107–19116.
Reprinted with permission from The Royal Society of Chemistry.[1]

2.1 Abstract

Nanoparticles (NP) have widespread applications from sensing to drug delivery where much behavior is determined by the nature of the surface and the resulting intermolecular interactions with the local environment. Ligand mixtures enable continuously tunable behavior where both the composition and morphology influence molecular interactions. Mixed ligand shells form multiple morphologies ranging from Janus to patchy and stripe-like with varying domain dimensions. Solvent-NP interactions are generally measured by solubility measures alone. Here we develop a quartz crystal microbalance (QCM) approach to more broadly quantify molecule-NP interactions via vapor phase uptake into solid NP-films independent from solvation constraints. The composition and morphology of mixed ligand shells were found to exhibit pronounced non-monotonic behavior that deviated from continuum thermodynamics, highlighting the influence of ligand morphology upon absorption/adsorption. Alkyl and perfluorinated thiols were used as a model case with constant core-size distribution. The ligand morphology was determined by 19F NMR. Molecule uptake into NPs was measured with five benzene derivatives with varied degree of fluorination. For the cases examined, QCM measurements revealed enhanced uptake for patchy morphologies and suppressed uptake for stripe-like morphologies. These results contrast with insights from solubility measurements alone where QCM sometimes identified significant molecular uptake with poor solvents. This QCM method thus provides new insights to molecule-NP interactions independent of the solvation shell.

2.2 Introduction

Nanoparticles (NPs) have gained widespread interest for a wide array of applications[1] such as chemical and biological sensing,[2] drug delivery for nanomedicine,[3] self-assembly,[4] and removal of contaminants.[5,6] The performance of a NP for an application is largely influenced by its intermolecular interactions with the local environment as determined by the character of the ligand shell. The ligand shell is the ultimate interface of the NP with the outside world and thus governs interactions with other objects. The properties affected by the ligand shell thus range from solubility, to self-assembly, drug delivery, biocompatibility, and targeted molecular uptake. Mixtures of ligands have been shown to enable hybrid behaviors, *e.g.* NPs with extensive hydrophobic or fluorine content can exhibit solubility in water and other aqueous media.[7,8]

The morphology of mixed ligand shells also significantly modifies NP behavior. On flat substrates,[9] ligand mixtures phase separates to reduce the enthalpic interfacial area[10] where the surface tension has a monotonic dependence on the ensemble composition.[11,12] Here, the molecular environment within each phase is identical to the mono-ligand film. Janus NPs are analogously phase separated with ligand domains on opposite sides of each NP, exhibiting a monotonic continuum of behavior[13] principally corresponding to the ensemble of two mono-ligand environments. Due to high curvature, mixed ligand NPs can also exhibit patchy and stripe-like ligand morphologies when coupled with appropriate pairs of ligands having different length.[14] The lowest free-energy configuration can promote mixed ligand interfaces to increase conformation-al entropy of the longer ligand.[15] Here the longer ligands explore additional conformational space when proximal to the shorter ligands. This remarkable entropy-

27

driven ordering[16] is widely documented to occur under specific conditions.[17] Patchy and stripe-like NPs are dominated by the mixed ligand interface and thus exhibit non-monotonic trends in behavior where the local molecular environment behaves distinctly from the bulk ensemble. The changes in molecule-NP interactions are not yet predictable *a priori* and are tedious to measure where each molecule-NP interaction is tested individually, typically with a solubility limit measurement.[18-20] The non-monotonic behavior exhibited by patchy and stripe-like nanoparticles has been explained by a combination of cavitation suppressing selective-solvent uptake or by confinement enhancing solvent uptake into appropriately matched molecular environments.[19] Cavitation and confinement thus work in opposing directions where the balance between the two leads to variable non-monotonic molecule-NP behaviors.[13] For example, a recent report with mixed ligand amphiphilic NPs having 67% hydrophobic ligand were most soluble in polar alcohols and this alcohol solubility was reduced when increasing the hydrophilic ligand content.[19]

NP saturation experiments with different solvents or solvation conditions are widely used to quantify solvent-NP interactions.[21-23] In contrast, more general measurements of molecule-NP interactions do not necessarily require a solvation shell. For example, NP drug loading is a separate criterion from solvation in the delivery medium. Here, we develop a quartz crystal microbalance (QCM) method to quantify molecule-NP interactions via vapor phase uptake into solid NP thin films. QCM has previously been used on NP films to monitor chemiresistence,[24-27] detect various biomaterials,[28-30] and to analyze cellular interactions[31] due to its high sensitivity. The approach uses miniscule NP quantities and can uniquely quantify molecule-NP

28

interactions with non-solvents. Here we examine a model system consisting of 1.8 nm gold NPs with a variable combination of short fluorophilic ligands and long lipophilic ligands that were expected to form patchy and stripe-like ligand morphologies.[32] The molecule-NP interactions were examined for a systematic series of fluorinated benzene derivatives as a function of NP ligand composition and morphology. Non-monotonic trends in solvent uptake were correlated to the ligand shell morphologies as a function of confinement and cavitation effects. The identification of ML-FNP-molecule interactions enable a detailed look at the ligand shell compositions that enable enhanced interactions with small molecules. This will be crucial for overcoming the insolubility of fluorinated materials and enabling the implementation of the fluorophobic effect for multimodal coassembly.

2.3 Experimental Methods

Materials

Gold trichloride (99.9%) was obtained from Strem Chemical and stored under inert atmosphere. α,α,α-Trifluorotoluene (≥ 99%, TFT) and anhydrous iodine lumps (99.99%, under argon) were obtained from BeanTown Chemical. Tetrabutylammonium borohydride (≥ 98%) and didodecyldimethylammonium borohydride (≥ 98%) were purchased from TCI America and stored under argon atmosphere before use. Potassium thioacetate (98%), benzene (99%), and 1-dodecane thiol (98%, DDT) were obtained from Alfa Aesar and used as received. 1H,1H,2H,2H-Perfluoro-1-iodooctane iodide (≥ 95%) and 1,3,5-trifluorobenzene (97%) were obtained from Matrix Scientific and used as received. Hexafluorobenzene (97%), 1,2,4,5-tetrafluorobenzene, and 1,4-difluorobenzene were obtained from Oakwood Chemical and used as received. Chloroform-D (99.8%) and

29

benzene-D$_6$ were purchased from Cambridge Isotope Laboratories Inc. and used as received. Toluene ($\geq$ 99.5%) obtained from Fisher Chemical was subjected to four cycles of freeze-pump-thaw and dried over molecular sieves prior to use.

1H,1H,2H,2H-Perfluoro-1-octanethiol (PFOT) synthesis

In a round bottom flask, potassium thioacetate was combined with 2-(perfluorohexyl)ethyl iodide in a 1.1 : 1 molar ratio along with THF. A condenser was connected to the flask and the reaction vessel was sealed and subjected to three cycles of freeze-pump-thaw to remove excess oxygen. It was then filled with inert nitrogen gas and heated for 5 h at 50 °C. The product was collected through filtration and the excess THF was removed by evaporation. The crude 1H,1H,2H,2H-perfluoro-octyl thioacetate was purified through vacuum distillation at 70 °C, purity and structure was verified with ^{1}H NMR spectroscopy. To obtain the deprotected thiol the purified thioacetate was added to a flask charged with 90 mL of ethanol and 40 mL of concentrated hydrochloric acid. A condenser was connected to the flask and the reaction vessel was sealed and subjected to three cycles of freeze-pump-thaw to remove dissolved oxygen. The vessel was filled with inert nitrogen gas and the reaction was heated for 13 hours at 90 °C. The crude thiol was extracted three times with 100 mL of hexanes and washed with 100 mL of deionized water and then dried overnight with magnesium sulfate. The magnesium sulfate was removed through filtration and the excess hexanes was removed through evaporation before the crude thiol was purified through vacuum distillation. The final purity and structure were verified using ^{1}H NMR spectroscopy.

Amine-stabilized NP (Am. NP) synthesis

In an inert argon glovebox atmosphere, 90 mg of gold(III) chloride was combined with a 0.1 M didodecyldimethylammonium bromide (DDAB) in toluene surfactant solution in a 125 mL Erlenmeyer flask. The solution was gently stirred until the precursor dissolved turning the solution a dark orange color. To this solution 216 μL of dodecylamine was added while stirring, it was then stirred until the dark orange color turned to a light-yellow. In a separate vessel 300 mg of tetra-*n*-butylammonium bromide (TBAB) was dissolved in 12 mL of the 0.1 M DDAB stock solution, the TBAB solution was then placed in a syringe. Both the flask and syringe were sealed under argon and taken out of the inert atmosphere. The gold precursor solution was then stirred at 1500 rpm. Once the solution reached 1500 rpm the TBAB solution was injected into the stirring flask, it immediately changed from a light-yellow color to a deep red. The resulting Am. NP solution was immediately used for ligand displacement.

Ligand displacement procedure

In a typical procedure, a premade ligand solution containing the desired ratio of DDT/PFOT was injected added to the Am. NPs immediately after synthesis. For mixed ligand NPs, the premade ligand solution was kept at a 1:1 total thiol:gold molar ratio and the proportion of each ligand in the solution was adjusted based on the desired shell composition. Post injection, the AuNPs were stirred for fifteen minutes at room temperature and then boiled at 120 °C for 20 min for the thiols to displace the dodecylamine ligands. Post boiling, the NPs were immediately washed six times using four toluene washes and two α,α,α -trifluorotoluene (TFT) washes to remove excess surfactant and excess ligands. After the washing cycles were complete, the particles were

www.manaraa.com

collected by centrifugation from methanol and stored as a powder. The resulting NP batches were termed xF according to the final ligand shell composition, *vide infra*, where the NPs had x mol% PFOT.

NMR experiments

^{1}H NMR experiments were carried out on a Bruker Avance III-HD 300 MHz. [19]F experiments were carried out on a Bruker Avance III-HD 400A MHz NMR. The ^{1}H chemical shifts are referenced to deuterated chloroform, while ^{19}F chemical shifts are referenced to TFT. An external reference of $CFCl_3$ was used to shift-correct the ^{19}F spectra to ensure correct peak positioning.

NP purity was analyzed using ^{1}H NMR to determine the presence of excess surfactant and unreacted ligand. A typical procedure involved dissolving 5 mg of NPs in either deuterated chloroform or TFT for the heavily fluorinated particles using ultrasonic agitation. The composition of NP ligand shell was measured after ligand stripping using I_2 decomposition. Here, 5 mg of NPs were dissolved in deuterated chloroform before 1-3 mg of metallic iodine was added. The solution was gently mixed at 250 rpm using a shaker until complete dissolution of the iodine occurred. It was then allowed to sit overnight to ensure complete disulfide formation. The black precipitate and iodine were removed, and the disulfides were measured using 128 scans on the ^{1}H NMR. The ligand morphology was determined using ^{19}F NMR measurements with 5 mg of NPs were dissolved in a mixture of TFT/C_6D_6 (97/3 wt.%). The particles were dispersed with a bath sonicator and were scanned using a 100-ppm window centered at -100 ppm with 256 scans.

Small-angle X-ray scattering (SAXS)

X-ray experiments were conducted using a SAXSLAB Ganesha at the South Carolina SAXS Collaborative. A Xenocs GeniX3D microfocus source was used with a Cu target to generate a monochromated beam with a 0.154 nm wavelength. The instrument was calibrated using National Institute of Standards and Technology (NIST) reference material 640c silicon powder with the peak position at 2θ 28.44 where 2θ is the total scattering angles. A Pilatus 300 K detector (Dectris) was used to collect the two-dimensional (2D) scattering patterns. Solutions were prepared by diluting the NPs to ~1 wt.% to avoid structure factor contributions. NP solutions were measured within sealed glass capillaries. A blank sample consisting of a capillary with only toluene/TFT was measured under the same conditions for background subtraction. SAXS data were acquired for 30 minutes at room temperature with an X-ray flux of 21.4 M photons per second incident upon the sample and a sample-to-detector distance of 425 mm. Data were processed using SAXSGUI and custom MATLAB scripts. The scattering form factor was fitted as a Gaussian number average distribution of hard spheres with a 25% standard deviation, determined by fitting several samples with the statistical spread as an independent variable. This constraint was needed to prevent irrational fit convergence.

Vapor swelling chamber

The vapor chamber was built in house using a bubbler mounted in a water bath to maintain constant temperature. A dry air line with a flow controller was plumbed into the bubbler to generate vapor at a fixed rate of 27 mL min^{-1}. The same flow was also used as a purge line after bypassing the bubbler. The output line was directed into a large temperature-controlled oven set to 35 °C containing a long copper coil to equilibrate the

vapor temperature before directing the gas phase into a 0.2 L glass chamber housing the QCM crystal. The exhaust line was plumbed from the glass chamber into a fume hood. Glass and metal connectors were used as much as possible to eliminate diffusive uptake of solvents into plastics.

Quartz crystal microbalance measurements

Quartz crystals with 6 MHz resonance frequency were used. NP films were spin coated at 5000 rpm from 1 wt.% solutions onto QCM crystals. The crystal was then measured using a Colnatec Phoenix head and a Colnatec Eon-LT monitor. RC cut QCM crystals were chosen to minimize temperature effects. Each measurement started with a system purge of dry air at the same flow rate of 27 mL min^{-1} followed by vapor exposure until the film reached equilibrium, ranging from 25-50 minutes. Following exposure to each solvent, the crystal was again subjected to a purge to remove physiosorbed solvent and restore the baseline QCM frequency. The changes in QCM resonant frequency were recorded 5 times per second. The frequency decrease corresponding to mass uptake was found to equilibrate with a single exponential decay. All data were measured for at least 1.8 times the fitted time constant (>83% progress towards equilibrium) to yield the equilibrium molecular uptake. The resulting frequency data was analyzed using custom MATLAB R2016b scripts. The changes to QCM resonant frequency were converted to the corresponding mass change using the Z-Match method:

$$\Delta m = \frac{\upsilon_q \cdot \rho_q}{2\pi \cdot z \cdot f_1} \cdot tan^{-1}\left(z \cdot tan\left(\frac{\pi \cdot (f_0 - f_1)}{f_0}\right)\right) = g\ cm^{-2}$$

where Δm is the change in mass (g cm^{-2}), υ_q is the frequency constant (333 600 cm s^{-1}), ρ_q is the density of quartz (2.648 g cm^{-1}), Z is the Z-factor (1 for mass loadings less than 10-20% frequency shift), f_1 is the final resonant frequency, and f_0 is the initial resonant

34

frequency. The NP-film mass (g cm^{-2}) was determined by using the resonant frequency of the bare QCM as f 0 and the resonant frequency with the NP-film as f_1. The molecular mass uptake (g cm^{-2}) was determined similarly by using the resonant frequency of the NP-film as f_0 and the resonant frequency with the NP-film under saturated vapor as f_1. Statistical uncertainty was determined either with repeated measurements or estimated as 10% of the nominal value.

Calculation of solvent-NP interaction

The molecule-NP interaction was compared for each solvent as a function of the NP ligand shell. The molecular uptake for each film was normalized by the NP film mass to yield comparable relative extents of uptake. The ratio of ($g_{molecule}$ cm^{-2})/(g_{film} cm^{-2}) yielded $g_{molecule}$ /g_{film} . The vapor pressure was maintained constant for each solvent since the molecular uptake mass ($g_{molecule}$) is dependent upon vapor pressure.

Ligand surface density calculations

The ligand surface density for NPs was determined using a combination of UV-Vis and quantitative ^{1}H NMR. The concentration of the gold NPs was analyzed using a Shimadzu UV-2450 Spectrometer over an absorbance range of 600 to 400 nm. Samples were prepared at approximately 0.2 mg of NPs per 1 mL solvent and placed in a fused quartz glass cuvette with a 1 cm pathlength. The concentration was calculated using Lambert-Beer law using the absorbance at 508 nm and the extinction coefficient based on the known NP diameter. The extinction coefficients were calculated using the constants k (3.32111) and a (10.80505).[33]

The ligand concentration was quantified after iodine decomposition using ^{1}H NMR spectroscopy with an internal standard of known concentration. Here the ratio of

the internal standard (1,4-difluorobenzene) to the ratio of the α H1 peaks of each ligand

were used to quantify the concentration of each ligand as detailed elsewhere.[34] Iodine

decomposition was carried out by adding 1-3 mg of metallic iodine to the dispersed NPs,

the particles were left to decompose for at least 12 hours to ensure complete disulfide

formation leading to a color change from deep red to clear violet. After twelve hours the

black precipitate was filtered o ff and the solution was taken for ^{1}H NMR analysis.

2.4 Results and Discussion

Fluorinated NP Synthesis and Strategy

In order to determine the interactions and behavior of fluorinated gold NPs a

ligand system must be chosen. Fluorinated thiols are often expensive due to the extensive

amount of fluorine content and limited stability in air. The perfluorinated precursors to
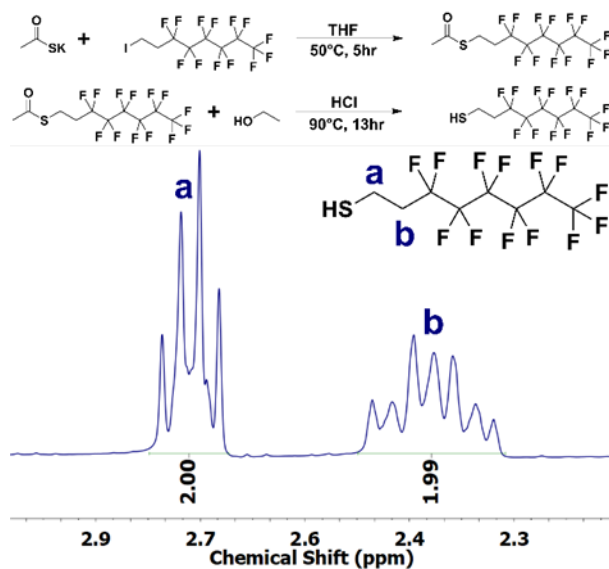
Figure 2.1 PFOT ligand synthesis route
including complete deprotection of the thiol
just prior to use (top) as well as ^{1}H NMR
confirmation of product (bottom).

the thiol compounds are stable in ambient conditions making them easier to work with

and affordable. In order to utilize the NPs for the fluorophobic effect extensive fluorine

36

content was needed in the ligand shell. However, a high inorganic content was desired, so the size of the ligand needed to be considered. The final choice for the fluorinated NPs was a 1H,1H,2H,2H-perfluorooctane thiol (PFOT) as it contains thirteen fluorine atoms and has a chain length of 8-carbons. The synthetic scheme for the PFOT ligand is shown in Figure 2.1. The first reaction is a simple SN2 type nucleophilic substitution where the thioacetate nucleophile displaces the iodine leaving group forming the perfluorinated thioester. The advantage to using the thioacetate nucleophile is that it acts as a protecting group for the thiol functional group which can be oxidized in ambient conditions to the disulfide. The thioester intermediate is stable at ambient conditions and can be deprotected when the fluorinated thiol is needed for synthesis. The deprotection procedure for the fluorinated thiol, PFOT, requires few synthetic steps with a facile cleaning procedure. The thioester can be cleaved by a mixture of concentrated hydrochloric acid and ethanol at reflux for thirteen hours. After three extractions with hexanes the crude thiol is dried using magnesium sulfate prior to vacuum distillation to collect the viscous clear liquid. After deprotection the thiol was stored in a tightly sealed vial under inert atmosphere and was used promptly for NP synthesis.

Once the PFOT ligand was obtained the perfluorinated NPs were synthesized. Gold NPs were chosen due to the numerous synthetic methods available that afford control over the size of the colloid. The first method chosen utilized a weak reducing reagent and a one phase system to produce gold NPs with a uniform size distribution.[35] The NPs were able to be synthesized in a variety of organic solvents and could be done in ambient conditions in a 20 mL scintillation vials. The use of a weak tert-butylamine borane complex allowed for a very slow reduction reaction affording great control over

37

the size of the NPs. The progress of the reaction was also easy to track by eye as the color

continuously changed from colorless, to yellow, to pink, to brown, to a purple, and finally

a vibrant wine-red color. The original ligand used in the synthesis was 1-decane thiol

which would displace the triphenyl phosphine ligand present on the gold precursor. The
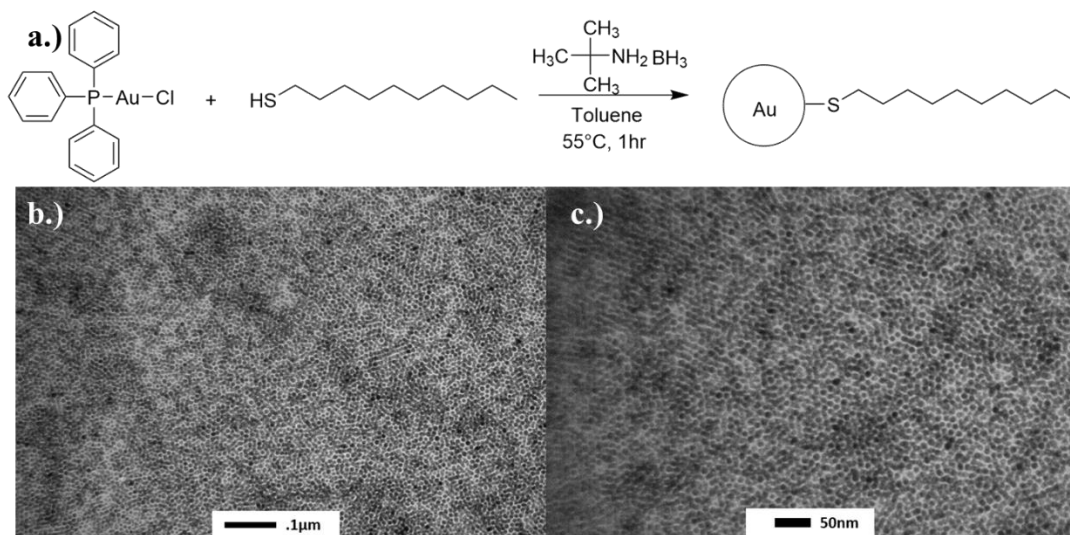
Figure 2.2 Shows the a.) synthetic scheme of the gold NPs ligated with 1-decane thiol, b.) image of the gold nanoparticles with a 100 nm scalebar, and c.) image of the gold NPs with a 50 nm scalebar.

NPs produced from this method are shown in Figure 2.2. TEM images of the gold NPs

shows sub 5 nm gold NPs with a fairly uniform size. This was similar to the results

obtained in the original publication.

With the original synthesis reproducible the perfluorinated NP synthesis was

attempted. A similar procedure was followed with the PFOT substituted for the 1-decane

thiol. The reaction followed a similar reaction at the beginning with the colorless solution

transitioning to yellow, then pink, and then brown. However, one the solution began to

transition to purple a black precipitate was observed settling at the bottom of the

scintillation vial and the purple color began to fade very rapidly. The reaction was

38

repeated multiple times with the precipitation occurring during the transition to purple.

The resulting NPs formed were sonicated heavily to attempt to form a stable suspension

though this was unsuccessful. TEM images of the perfluorinated NPs formed show very

large aggregates (Figure 2.3). Inside of the aggregates the individual NPs are observed.
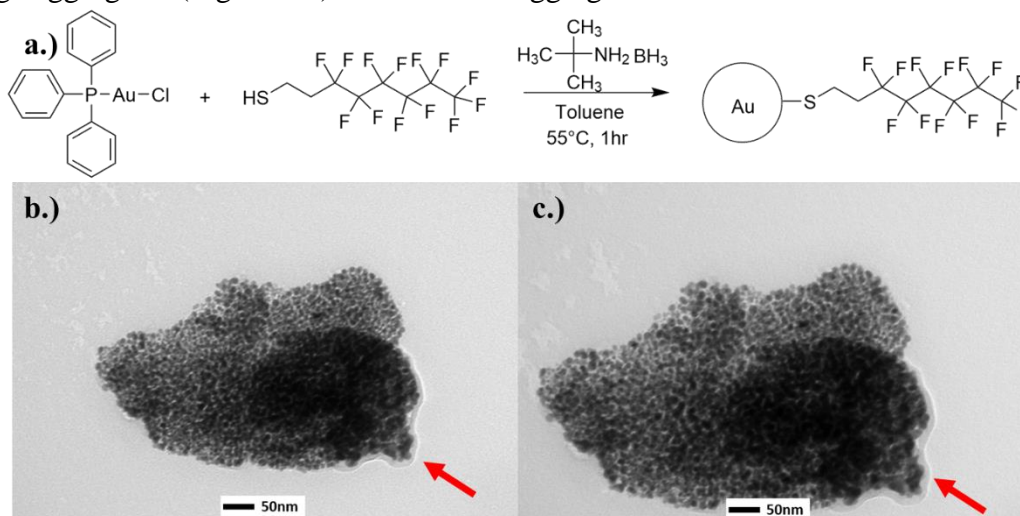
Figure 2.3 Synthesis of the a.) gold NPs ligated with the PFOT ligand, b.) TEM
image of the large aggregate formed during the formation of the gold NPs, and
c.) image of the aggregate at a higher magnification. Red arrows in both b and c
show what appears to be a thick layer of the PFOT ligand.

The red arrows in Figure 2.3b and 2.3c highlight what appears to be a thick layer of the

PFOT ligand. The precipitation of the as-made perfluorinated gold NPs from solution is

due to the insolubility of perfluorinated NPs in common organic solvents. As the NPs are

capped with the highly fluorinated PFOT ligand they become insoluble in the toluene

solvent system leading them to aggregate and ultimately precipitate from solution. As this

occurs the concentration of gold and ligand in solution is altered leading to a loss of

control. Due to the solubility issue a new synthetic method needed to be used that would

avoid the direct synthesis of the PFOT NPs. A new mixed ligand approach would be

implemented to have greater control over the size and fluorinated of the NPs.

Preparation of mixed-ligand NP

The synthesis of the mixed ligand system was carried out using the PFOT ligand and a lipophilic DDT ligand. In order to better understand the effect that changing the ratio of PFOT in the ligand shell would have on the behavior a range of mixed ligand NPs were synthesized under conditions expected to form patchy and stripe-like ligand morphologies. The formation of these morphologies are attributed to ligands with different lengths on a NP of suitable curvature, *e.g.* generally ~2-8 nm in diameter.[36,37] A recent experimental and computational study examined mixtures of fluorophilic and lipophilic ligands on 2-4 nm gold NPs where the length of the ligands were varied across a wide composition range to determine the impact on ligand morphology.[32] Janus regions were observed if the ligands had similar length as the phase separation is driven by the reduction of interfacial area. The flexible lipophilic ligands needed to be >4-6 carbons longer than the stiff fluorinated ligands to form patchy or stripe-like morphologies increasing the interfacial area and free volume. The resulting morphologies were mapped for patchy (0 – 30 mol% fluorinated and 60-100 mol% fluorinated) and stripe-like (30-60 mol% fluorinated) morphologies. These prior works[32] suggest that our selection of DDT and PFOT (4 carbon difference) with 1.8 nm diameter Au NPs will yield patchy and stripe-like ligand morphologies.

Mixed ligand NPs were prepared using standard methods. Murray *et al.*[38] developed a method for mixed ligand NPs using a post-synthesis ligand exchange. This process was later expanded to displace weakly bound amine or phosphorous ligands with stronger binding thiol ligands.[39] The first stage of a ligand displacement involves competitive binding where molar excess or differential binding strength result in

preferential deposition of the new ligand(s). With mixed ligands, the next stage is the

evolution of the ligand shell morphology via continuous ligand exchange with the

solution. The desorption/binding rates as well as the chemical dissimilarities establish the

timeframe for this process.[40] The NP core size is thus constant and is decoupled from the

final ligand chemistry[39,41] (Figure 2.4). The figure highlights the ability to displace the

weaker binding R1 (blue) with the stronger binding R2 (red), R3 (green), or a mixture of

the two. At both ends of the spectra are the mono-ligand NPs which will either be highly

lipophilic for the DDT NPs or fluorophilic for the PFOT NPs. The compositions that are

the most interesting are the NPs with a tunable ligand shell. These particles should have
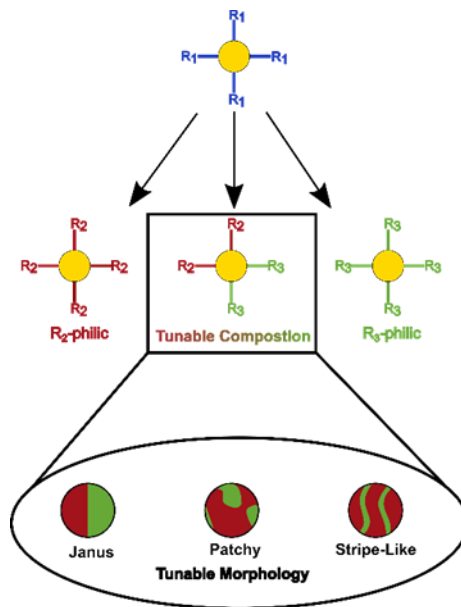
Figure 2.4 NPs with mixed ligand shells can have variable composition and ligand morphology. Displacement of weakly bound ligands (R_1) with strong binding ligands (R_2, R_3) yields systematic NP series with constant NP core size distribution and variable ligand shells.

41

unique interactions with their local environment due to the chemical nature of the ligand shell. These NPs will also have morphologies in the ligand shell that will impact the interactions.

Our synthesis used a procedure for aminated <5 nm[41] Au NPs followed by amine displacement with lipophilic DDT and fluorophilic PFOT ligands. A single-phase method was again chosen to synthesize the NPs. Color changes were also used to determine the progress of the reaction as the complete dissolution of the gold chloride precursor produce a dull yellow solution. After addition of the amine ligands the reaction slowly turned from dull yellow to a dark orange color indicating the reaction was ready to proceed to the reduction and NP formation. Due to the usage of a stronger borohydride reducing reagent the reaction was much faster than the prior method going from dark orange to a dark red color. The reaction was carried out at multiple stirring rates to determine the most favorable conditions for NP formation. It was determined that a higher spin speed yielded greater control over the reaction. This observation is attributed to the higher stir rate leading to faster mixing of the borohydride reducing reagent with the gold precursor solution. Since the reducing reagent is stronger than the previous reaction upon a faster addition is required. At slower spin speeds the mixing of the reducing reagent is slower which may lead to a change in the gold concentration leading to less control.

After synthesis of the as-made aminated NPs the ligand exchange process was performed. The stronger binding DDT, PFOT, or a molar ratio of the two was added to the stirring aminated NP solution immediately post synthesis. During the fifteen minutes at room temperature almost no changes were observed for the ML-FNPs with

small percentages of PFOT in the ligand shell. As the amount of PFOT added during the exchange procedure reached 90% the dark red solution became lighter in color as a black precipitate was formed. As discussed with the previous method this is attributed to the highly fluorinated ML-FNPs becoming soluble in toluene. After fifteen minutes the ML-FNPs were boiled at 120˚C to promote complete exchange of the amine ligand and allow for phase separation to occur. During the boiling process all of the ML-FNPs, including the highly perfluorinated NPs, became soluble in the toluene. As the solutions were cooled to room temperature all remained soluble in the toluene surfactant mixture including the perfluorinated nanoparticles. This is most likely due to the surfactant being trapped in the perfluorinated thiol ligands which increase the stabilization of the suspension.

SAXS was used to confirm the NP size distributions. To attain the size distribution for NPs dilute solutions must be used in order to obtain scattering from the individual NPs in solution. If the sample is too concentrated, then the scattering signal from the NPs will contain contributions from their neighbors.[42] The samples used for SAXS analysis were kept at 1 wt.% to avoid contributions from neighboring NPs. All of the samples were measured in a glass capillary tube and background subtraction was performed to obtain the scattering from the ML-FNPs. Comparison of the Am. NPs to ligand displaced NPs resulted in similar scattering curves with the nearly identical q-positions for local minima and maxima (Figure 2.5). Each dataset was well fitted using a hard sphere form factor with a Gaussian size distribution. The results indicated nominal NP diameters from 1.7-2.1 nm, with some minor differences between the converged fits (Table 2.1).

The results from the size distribution methods revealed important information regarding ligand displacement and the stability of the ML-FNPs. The ligand displacement procedure does not significantly affect the size of the Am. NPs. This could be attributed to the large excess of stabilizing ligands in solution preventing core-core contact of the individual NPs leading to growth. This is shown by the first seven samples listed in Table 2.1. However, after eight months of continuous dispersion, drying, and re-dispersion procedures some growth was observed in the NP samples. The mean diameter of the samples measured after eight months of usage show a significant size change up to 4.8 nm. This could be attributed to aggregation in solvents that do not contain excess free ligand. The size change was also slightly visible by eye as the normally vibrant red color
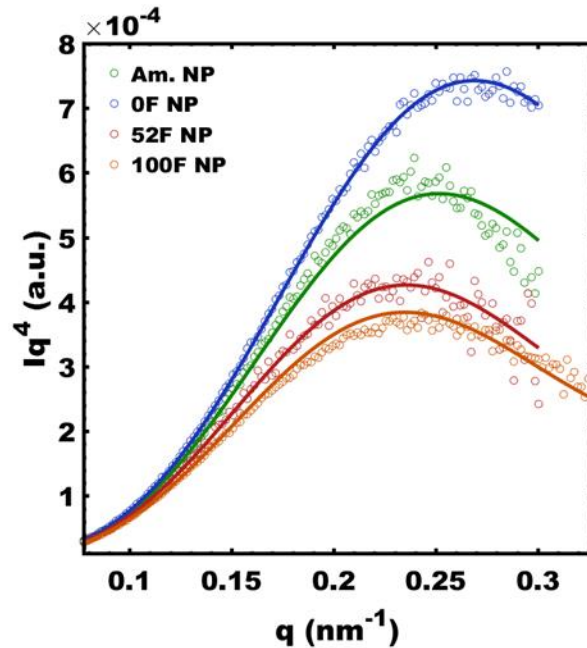
Figure 2.5 Porod plots of aminated, 0F, 25F, 52F, 100F NP solutions. Data points and best-fit lines are indicated. Scattering data are offset vertically for clarity.

became slightly dull. One sample in particular that was stored for more than ten months

after extended usage became non-dispersible in organic solvents.

Table 2.1 NP Dimensions from SAXS analysis by fitting a polydisperse hard sphere form factor model.

PFOT in Ligand Shell (%)	Mean NP Diameter (nm)[†]
Am. NP	1.8
0	1.7
25	1.8
50	2.0
65	2.0
75	2.0
90	2.1
100	2.0
20[‡]	3.0
31[‡]	4.5
39[‡*]	-
52[‡]	2.0
59[‡]	4.8
73[‡]	2.1
93[‡]	2.2

[†] Fitted using a Gaussian distribution of hard spheres with a standard deviation of 25%.
[‡] Measured after 8 months of storage as a powder.
[*] NPs were not dispersible for SAXS measurement after extended storage.

Thus, the ligand displacement procedure was shown to not significantly alter the NP core

size distribution and thus morphology changes are not due to significant size NP changes.

The resulting mixed ligand NPs were rigorously purified before determination of

the ligand surface density and composition. The synthesis solution contained a surfactant

to improve NP solubility, however residual surfactant would influence subsequent

measurements of molecule-NP interactions. The NPs were thus purified with iterative

dispersal/precipitation cycles. The NPs were dissolved in either toluene or TFT and

sonicated for twenty minutes to free the excess ligand and surfactant. Next a poor solvent

for the NPs was added, usually methanol, and the solution was sonicated for another five

minutes to ensure the excess ligand and surfactant were free from the NP ligand shell.

The NPs were collected as a black precipitate using the centrifuge. NPs with less PFOT

content were easier to clean and precipitated after one cycle of the centrifuge. NPs with

high PFOT content often required multiple rounds of the centrifuge during each cleaning
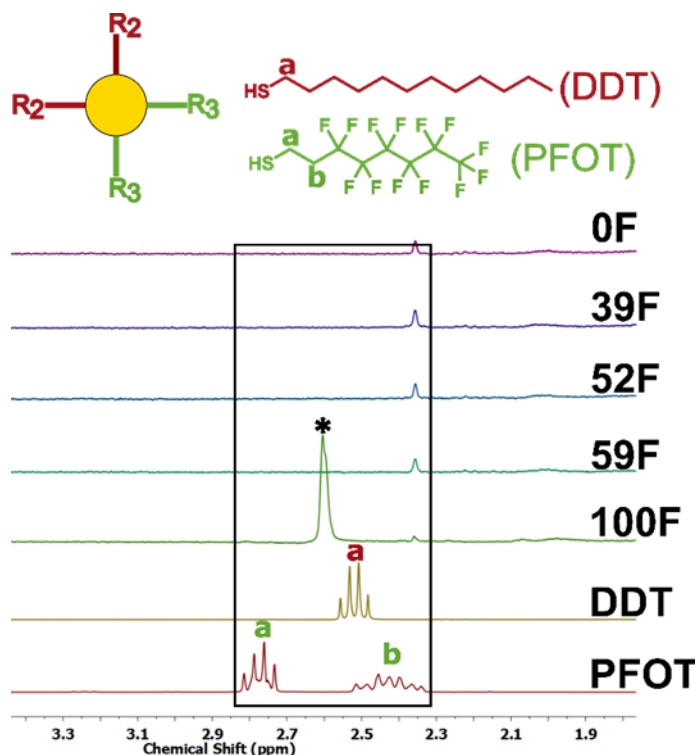
Figure 2.6 NMR of the ligated nanoparticles after washing showing the absence of free ligand. NMR of the DDT thiol is represented by the red a while the free PFOT is denoted at the bottom of the image. *TFT added for solubility. The NPs were named by the mol% of PFOT in the DDT/PFOT ligand shells, see Figure 2.7.

step. The solubility of the NPs changed markedly with the cleaning steps as well

documented before.[43,44] NMR spectra after six wash cycles were without sharp peaks

associated with free-ligand or surfactant (Figure 2.6). The bottom two NMR spectra show

the signal for the pure DDT and PFOT ligands. Both contain very distinct proton signals

with sharp peaks common with unbound molecules that have the ability to freely rotate.

46

The sharp signals indicative of the free ligands in solution are absent from the ML-FNPs indicating that all of the excess DDT and PFOT has been removed. The peaks for the surfactant are also absent from the NMR spectra of the ML-FNPs.

An aliquot of the mixed ligand NPs was then striped of ligands using metallic iodine to improve quantification of the formerly-bound ligand population (Figure 2.7). NMR of NPs with ligands bound to the surface is difficult due to the restricted rotation of the ligands. This leads to broadening of all the hydrogen signals present. The intensity of
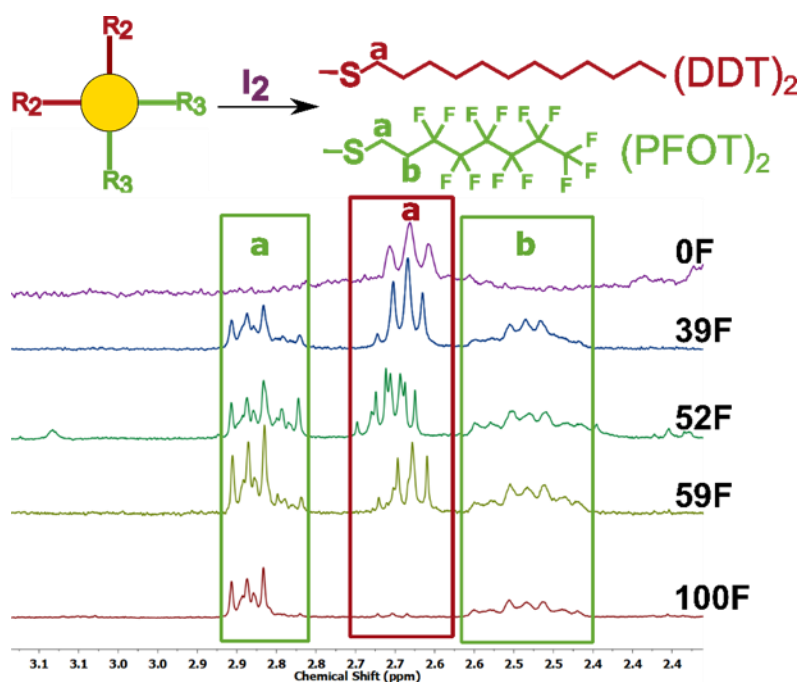
Figure 2.7 The NP bound ligand composition was measured by NMR after ligand stripping with iodine, resulting in the corresponding disulfide mixtures.

the signal is also diminished due to the inability of the ligand molecules to freely rotate. This can lead to inaccurate integration of the ligand ratios. The signal of the DDT and PFOT hydrogens was improved by stripping the ligands from the NP surface allowing for the molecules to freely rotate. A common reagent used for the ligand removal process is metallic iodine which decomposes the gold NPs. This is a destructive technique and is

47

only done with an aliquot of the ML-FNPs. The ligand stripping was carried out for at least twelve hours to ensure complete removal of both the DDT and PFOT. The completion of the ligand stripping is marked with the formation of a black precipitate in the bottom of the solution that is removed prior to NMR. The results of the ligand stripping reaction are shown in Figure 2.7 The 0F-FNPs have a signal located near 2.7 ppm attributed to the DDT ligand. No peaks are present for the PFOT α or β hydrogens. It is important to note that the thiols stripped from the surface of the gold form disulfides which can impact the peak splitting and chemical shift. As the ratio of PFOT in the ML-FNPs was increased peaks at 2.85 and 2.55 ppm appear. These peaks are attributed to the α and β hydrogens, respectively. As expected, the 100F-NPs do not have a detectable signal for the DDT ligand. Though the iodine stripping process is destructive it is both facile and cost effective. The method is not time consuming as the stripping can be performed in a small scintillation vial allowing for multiple ML-FNPs to be stripped consecutively.

The ratio of bound ligands was fully tunable from 0 – 100 mol% PFOT with minor deviation from the exchange solution composition (Figure 2.8 and Table 2.2). Each ML-FNP sample synthesized is represented by a blue square. During the exchange process the molar ratio of the gold and thiol is 1:1. Thus, an excess of the thiol mixture is added to the Am. NP solution which can lead to the slight deviation in the ligand shell composition. A majority of the samples had a higher percentage of PFOT in the ligand shell than the targeted composition. Figure 2.8 does show that a series of ML-FNPs with slight variations in PFOT content were synthesized. This enables greater understanding of small additions of PFOT to the ligand shell.

After the determination ligand shell composition, the density of ligands on the

surface of the NPs was explored. A common method for the determination of the ligand

density is thermogravimetric analysis (TGA). Samples are placed on a precision balance
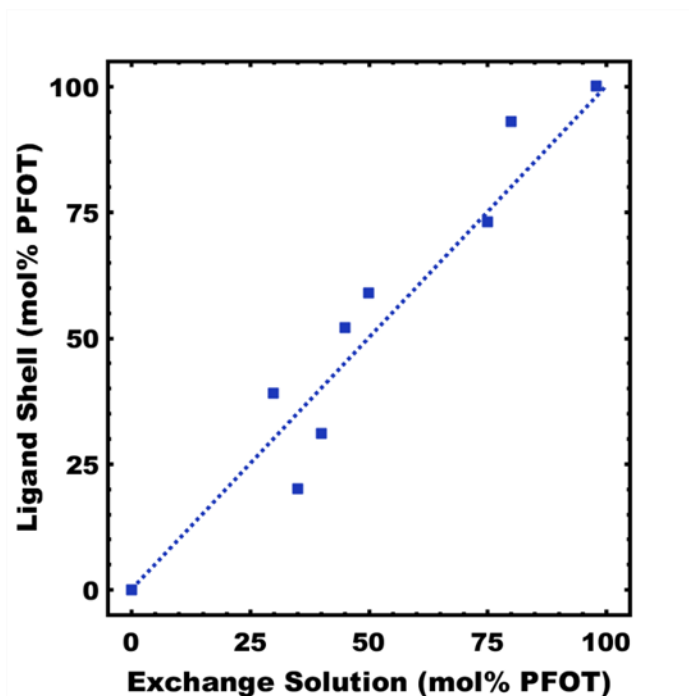
Figure 2.8 Correlation of ligand exchange solution
composition to the composition of bound ligands on
nanoparticle surfaces (DDT and PFOT ligands).

in a furnace and the weight loss of the sample is tracked as the temperature is increased.

The organic ligands would decompose, and the total mass of the gold would be

determined. The downside to TGA is that it is destructive to the sample and requires

close to 10 mg for a more accurate determination of mass loss. Another popular method

to determine the ligand density of a sample is by using NMR with an internal standard. A

benefit to using an NMR based method is that it can be combined with the

experimentation to determine the composition of the ligand shell. Thus, less ML-FNP

sample needed to be destroyed to determine the ligand density allowing for more sample

49

to be conserved for later experiments. By adding an internal standard to the NMR

solution containing the stripped ligands the total concentration of ligands could be

determined. A non-convolved internal standard (1,4-difluorobenzene) was included in the

same ligand stripping experiments to. A fringe benefit of the chosen internal standard is

that it also improves NP solubility. Comparison of the ligand concentration to the NP

concentration determined by optical absorption experiments yielded the surface ligand

density. An example of the UV-Vis and NMR spectra can be found in Figure 2.9a and
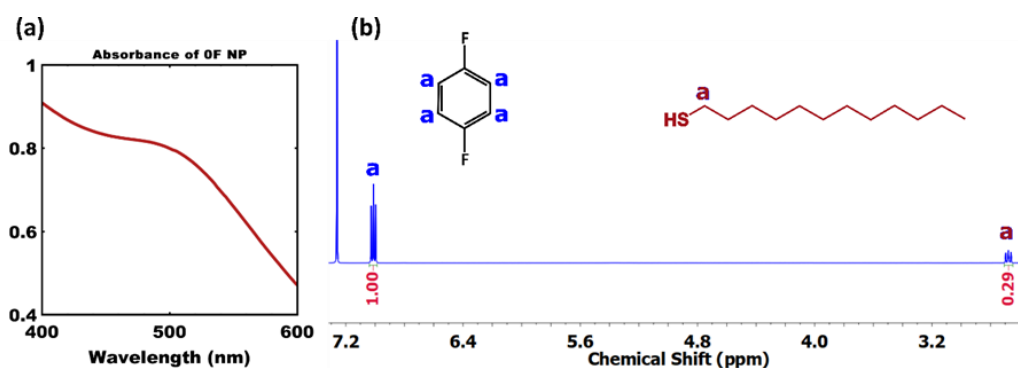
Figure 2.9 Ligand surface density calculations were performed using the (a)
absorbance of the NPs at 508 nm and (b) the ratio of the proton integrations of
the DDT or PFOT ligands and the reference standard at 7.14 ppm. Data are
presented from the 0F NP sample.

2.9b, respectively. The absorbance of the NP solution at 508 nm was used to determine

the NP concentration (Figure 2.9a). The proton signal for the aromatic protons of 1,4-

difluorobenzene is observed as a sharp triplet near 7.1 ppm (Figure 2.9b). The proton

ratio of the 1,4-difluorobenzene and the DDT/PFOT ligands was used to calculate the

concentration of ligands. A small number of standards such as 1,3,5-trifluorobenzene and

1,2,4,5-tetrafluorobenzene were screened as well. The 1,2,4,5-tetrafluorobenzene was

ruled out as the proton signal of the aromatic peak overlapped with the signal from

deuterated chloroform. The 1,3,5-trifluorobenzene was eliminated as the boiling point is

75°C, fifteen degrees lower than 1,2-difluorobenzene.

50

The ligand surface density for all mixed-ligand NPs examined were within the range of 1-5 # per nm^2, consistent with similar reports of NPs without detectable free-ligand[34] (Table 2.2). As stated previously any excess ligand and surfactant from the synthesis and exchange reaction needed to be removed from the ML-FNPs as their presence would impact the interactions of the NPs with small molecules. All of the ML-FNPs synthesized underwent a rigorous cleaning procedure with six dispersion and redispersion cycles with twenty-five minutes of sonication for each wash. The sonication used in the cleaning procedure should not remove bound thiol from the surface of the NP affecting the dispersion ability. This hypothesis was tested using the Am. NPs using the weaker binding amine ligands. The Am. NPs were collected after methanol was added to the as-made NP solution and it was placed in the centrifuge. The Am. NPs were then dispersed in toluene and subjected to the same washing procedure as the ML-FNPs bound with DDT and PFOT. After one cycle of sonication a large fraction were not able to be re-dispersed in toluene. After a second cycle of sonication none of the Am. NPs were able to be re-dispersed in toluene suggesting that the sonic agitation was strong enough to remove the weaker amine ligands. The ML-FNPs bound with the DDT and PFOT are easily dispersed in a favorable solvent system after six cycles of sonication. The ML-FNPs are easily dispersible even after months of storage as a dry powder. Therefore, some of the lower ligand densities observed should not be attributed to the cleaning procedure. A series of purified DDT/PFOT mixed ligand NPs were thus prepared with constant size distribution.

Table 2.2 Ligand shell compositions and surface densities for mixed ligand nanoparticles

NP Batch	Exchange Solution Composition (mol% PFOT)	Ligand Shell Composition (mol% PFOT)	NP Concentration UV-Vis ($Mx10^{-6}$)	Ligand Concentration NMR ($Mx10^{-4}$)	Ligand Surface Density, σ (#/nm^2)
0F	0	0	2.6	1.2	5.2
20F	25	20	0.92	0.45	1.2
31F	40	31	2.8	3.7	3.7
39F	30	39	1.9	0.92	1.5
52F	45	52	2.3	0.59	1.0
59F	50	59	2.1	0.41	1.2
73F	75	73	1.4	0.19	2.5
93F	80	93	1.5	0.22	4.0
100F	98	100	1.7	3.7	4.1

Determination of ligand morphology by ^{19}F NMR

Numerous methods can determine the morphology of mixed ligand NP shells. Common methods include NMR,[45,46] mass spectroscopy,[47] Scanning Tunneling Microscopy,[48] MALDI-TOF,[40] UV-Vis paired with Cryo-TEM,[49] Electron Spin Resonance,[50] Infrared Spectroscopy paired with STM,[51] and contact angle measurements.[52] Here we used the method developed by Pasquato *et al.* to determine the mixed ligand morphology using trends in ^{19}F NMR chemical shifts. The method was demonstrated with similar fluorophilic/lipophilic ligand mixtures and was supported by computational predictions.[32] By using ^{19}F NMR, which has high sensitivity due to the large chemical shift range, small changes in the local environment result in larger chemical shifts. If a ligand is surround by identical neighbors, similar to a mono-ligand film, then the chemical shift is insensitive to composition changes. Interfaces of different ligands have a different chemical shift where the extent of the shift is a weighted average of the local ligand environments. Distinct trends in chemical shift with ligand composition are anticipated for different sequences of ligand morphologies.

The first system studied investigated the affect a branching ligand had on the formation of phase separated domains. The ligands used for this study were 3-methyldodecane-1-thiol (brC12), a twelve-carbon long chain with a branching methyl group, and 1H,1H,2H,2H-perfluorooctane thiol (F6). It is important to note that the F6 used in this study is the exact same ligand we used for our particle synthesis, referred to as PFOT. The chemical shift of both the terminal CF_3 and the 7th CF_2 carbon both show a linear decay as the amount of F6 in the ligand shell is increased (Figure 2.10). The linear

Figure 2.10 Chemical shift variation of (a) CF3 groups and (b) 7-CF2 nuclei increasing the percentage of the fluorinated ligand in the monolayer of NP-brC12/F6. Solid line serves as a guide for the eyes only. Reprinted with permission from Şologan, M.; Marson, D.; Polizzi, S.; Pengo, P.; Boccardo, S.; Pricl, S.; Posocco, P.; Pasquato, L. ACS Nano **2016**, 10, 9316–9325. Copyright 2016 American Chemical Society.

decay suggests that the environment of each F6 ligand is an average of the total composition of the ligand shell. This suggests that the mixture of the brC12/F6 cannot form phase separated domains as the chemical environment of the F6 coincides with the average composition of the ligand shell. Thus, a branching ligand appears to inhibit phase separation by sterically hindering ligand packing.

The second system investigated was a mixture of ligands with equal length. The ligands used were dodecane thiol (C12) and 1H,1H,2H,2H-perfluorododecane thiol (F10) which are both exactly 12 carbons in length. The chemical shift of both the CF_3 and 9th CF_2 exhibits a sharp decay from 0-40% followed by a fairly constant value from 40-100%, respectively (Figure 2.11). The sharp decay up to 40% F10 in the ligand shell
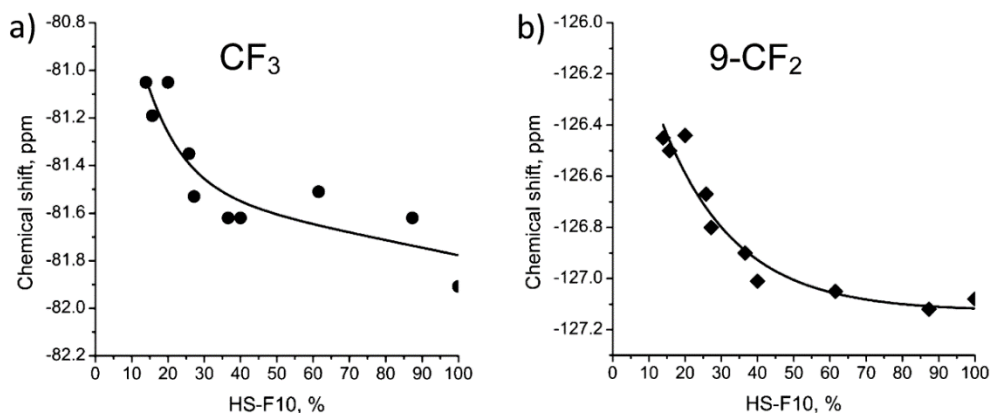
Figure 2.11 Chemical shift variation of (a) CF3 and (b) 9-CF2 nuclei increasing the percentage of the fluorinated ligand in the monolayer of NP-C12/F10. Solid line serves as a guide for the eyes only. Reprinted with permission from Şologan, M.; Marson, D.; Polizzi, S.; Pengo, P.; Boccardo, S.; Pricl, S.; Posocco, P.; Pasquato, L. ACS Nano **2016**, 10, 9316–9325. Copyright 2016 American Chemical Society.

suggests a very large increase in the interface between the C12 and F10 ligand. As the interface grows more F10 ligands are influenced by their C12 neighbor. The ceasing of the chemical shift decay from 40-100% suggests that there is no longer a change in the amount of F10 ligand at the interface and new F8 ligands are being placed in the center of the F10 domain as they experience the same chemical environment. These results are interpreted as the formation of two large phase separated domains of the C12 and F10 ligands, respectively. This is the equivalent to a Janus NP. The theoretical simulations

54

further strengthen the results obtained by ^{19}F NMR as the formation of a Janus type ligand shell was observed for the equal length ligand mixture.

The final system investigated was a mixture of ligands with differing lengths. Here two unique systems were studied in detail. The first was a mixture of ligands with a very large 8-carbon difference in length, the ligands used were hexadecane thiol (C16), an alkyl thiol 16 carbons in length, and the F6 ligand. A linear decay in the chemical shift
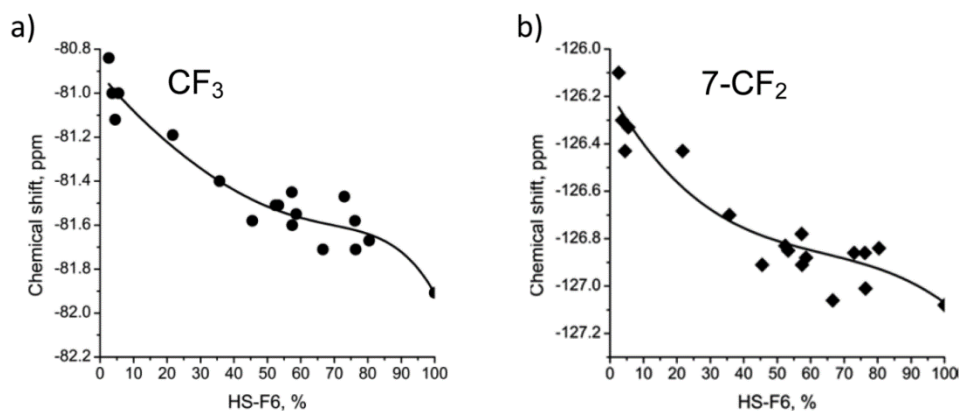
Figure 2.12 Chemical shift variations of (a) CF3 groups and (b) 7-CF2 nuclei increasing the percentage of the fluorinated ligand in the monolayer of NP-C16/F6. Solid line serves as a guide for the eyes only. Reprinted with permission from Şologan, M.; Marson, D.; Polizzi, S.; Pengo, P.; Boccardo, S.; Pricl, S.; Posocco, P.; Pasquato, L. ACS Nano **2016**, 10, 9316–9325. Copyright 2016 American Chemical Society.

was observe from 0-40% F6, followed by a linear region of constant chemical shift, and then another small decay from 80-100% F6 in the ligand shell (Figure 2.12). The linear decay suggests a constant change in the chemical environment. Between 40-80% the fairly constant chemical shift suggests that new F6 ligand added to the ligand shell experiences a similar environment. Finally, when the onset of another decay from 80-100% suggests another change in the morphology of the ligand shell. The theoretical simulations indicated thin stripe-like domains forming around 20% F6 in the ligand shell with a growing interface until 40% of the F6 ligand was present. The growing interface

would allow the taller ligand more free volume and a gain in conformational entropy similar to the results observed in previous studies and consistent with the observed decay in the chemical shift.[36] As more of the F6 was added to the ligand shell it added to the center of the stripe-like domain and the amount at the interface remained constant. These results are also consistent with the chemical shift behavior. Finally, as the amount of F6 was increased above 80% the ratio of ligand at the interface changed causing another decay in the chemical shift.

The final system, and most relevant to the discussion of this thesis, investigates a small difference in ligand length. The ligands used were 1-dodecane thiol (C12) and F6 which have a 4-carbon difference in length. This is the exact ligand system of the ML-FNPs synthesized for the QCM studies. The decay of the chemical shift for both the CF_3
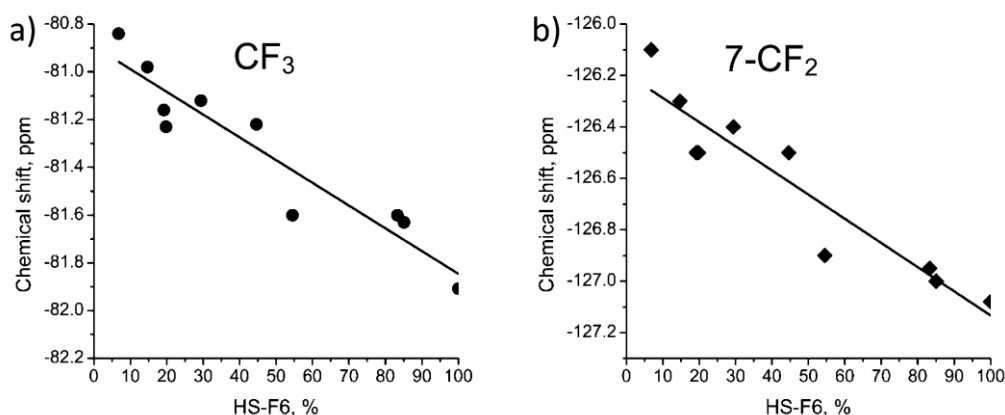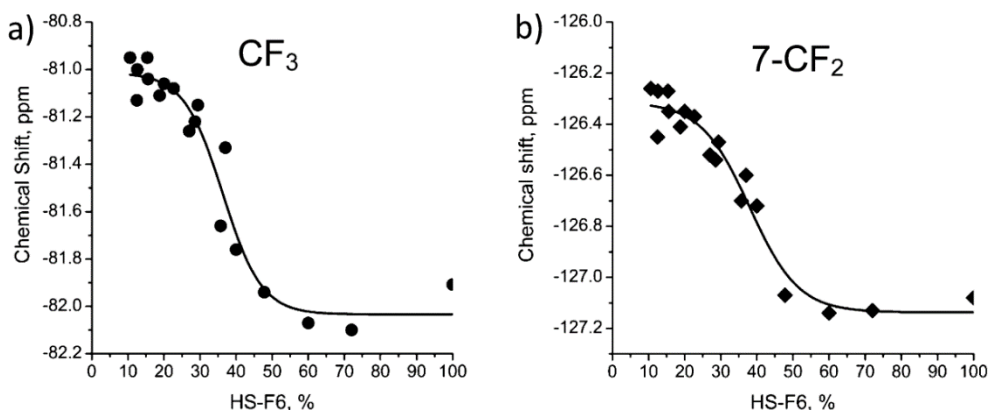

Figure 2.13 Chemical shift variations of (a) CF_3 groups and (b) 7-CF_2 nuclei increasing the percentage of the fluorinated ligand in the monolayer of NP-C12/F6. Solid line serves as a guide for the eyes only. Reprinted with permission from Şologan, M.; Marson, D.; Polizzi, S.; Pengo, P.; Boccardo, S.; Pricl, S.; Posocco, P.; Pasquato, L. ACS Nano **2016**, 10, 9316–9325. Copyright 2016 American Chemical Society.

and 7th CF_2 shows a sigmoidal shape with a plateau from 0-30% F6, followed by a rapid decay from 30-60% F6, and another plateau from 60-100% F6, respectively (Figure 2.13). The plateau regions suggest a fairly constant interface between the C12 and F6

ligands. The rapid decay from 30-60% suggests a growing interface between the C12 and F6 ligands. The second plateau region from 60-100% suggests that as more F6 is added the interface remains constant due to the similar chemical environment felt by the F6 ligands. The simulations run for this system show uniformly sized small patchy regions forming in the ligand shell. Since the ratio of the ligands at the interface are not changing in the small patches the chemical shift would not exhibit a large decay consistent with the observed plateau. After 30% F6 was added elongated patches or stripe-like domains were formed which increased the interface of the C12/F6 allowing for the longer ligand to have greater conformational entropy. The elongated patches and stripe-like domains continued to grow and increase the interface until 60% F6 at which point the domains grew into larger patches. These results support the rapid decay observed in the chemical shift. As more fluorinated ligand was added it filled in the middle of the patches without changing the interface. This is consistent with the second plateau in the chemical shift as the F6 ligands experience a similar environment with its nearest neighbors. Therefore, the sigmoidal shape of the chemical shift should represent patchy morphologies in the plateau regions with an elongated patch or stripe-like domain in the region of rapid decay. Figure 2.13 will be referenced in the discussion of the 19F NMR results on the ML-FNPs used in the QCM study of NP interactions.

The method of tracking the chemical shift decay of the terminal CF3 and 7th CF2 is easy to use. Since ^{19}F has a nuclear spin of ½ and comprises 100% of all naturally occurring fluorine atoms it is highly sensitive to NMR measurements. ^{19}F also has a very wide chemical shift window enabling better resolution of chemically similar fluorine atoms. An example of a common ^{19}F spectra for the ML-FNPs is shown in Figure 2.14.

The CF3 and 7th CF2 peaks are labeled for the PFOT ligand. For each ML-FNP composition the peak center of the two labeled peaks was tracked. Using the chemical shift, the local environment of the PFOT ligand could be investigated using the same
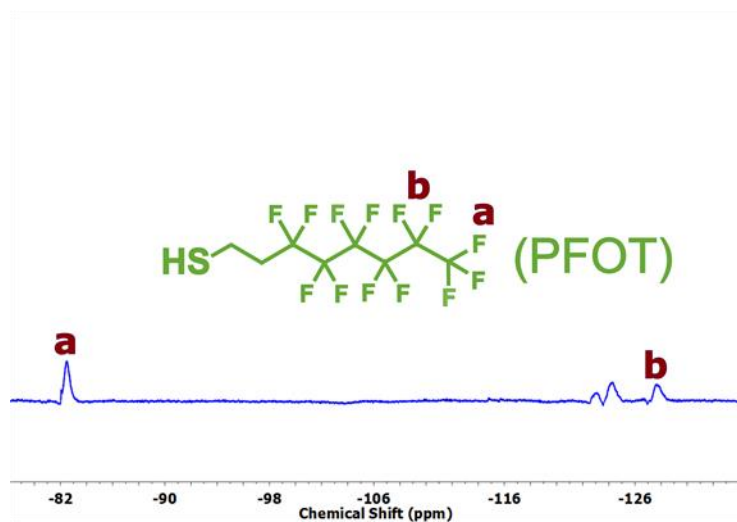
Figure 2.14 Representative ^{19}F NMR spectra for the NP series showing data from sample 73F NP. The chemical shift was tracked to determine the morphology.

methods described for Figure 2.13. Figure 2.14 also shows the two peaks are intense and deconvolved with the other fluorine atoms in the PFOT ligand. One important factor impacting the chemical shift is the solvent system used for the ^{19}F NMR. The solvent environment will alter the chemical shift of the CF_3 and 7th CF_2 groups as they are at the termini of the ligand shell. This must be accounted for in order to analyze the local environment of the ligand shell. A stock solution of constant composition and concentration was used for the entire series of ML-FNPs analyzed by ^{19}F NMR.

The ^{19}F NMR measurements of both the CF_3 group centered near ~80 ppm and the 7th CF_2 group centered near ~127 ppm both exhibited sigmoidal trends in chemical shift with ligand composition for the synthesized NP series (Figure 2.15 and Table 2.3). The CF_3 group (Figure 2.15a) has a more well pronounced plateau region at both low and

high PFOT content with the decay of the chemical shift beginning with the 31F sample.

These results are also consistent with Figure 2.13 where the decay in the chemical shift

occurs once the ligand shell is comprised of 30% fluorinated ligand. The chemical shift

then begins a rapid decay until it reaches a plateau near 70% PFOT in the ligand shell.

The observed decay suggests a constantly increasing interface between the DDT and
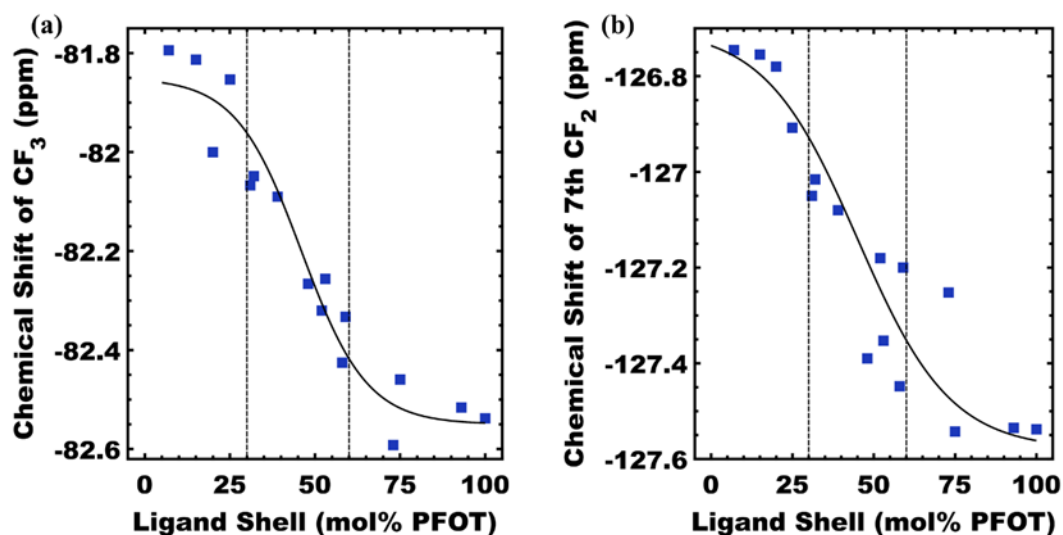
Figure 2.15 Trends of 19F NMR chemical shift for -CF3 (a) and the 7th -CF2- (b) on
PFOT as a function of NP ligand composition (DDT/PFOT). A sigmoidal guide line
is presented. Interpreted transitions in ligand morphology are indicated with dashed
drop lines.

PFOT ligands. As the PFOT content exceeds 73% the chemical shift remains fairly

constant suggesting no change in the interface. The 7th CF_2 plot has a small plateau of

fairly constant chemical shift from 7-20% PFOT in the ligand shell with the decay

beginning with the 25% PFOT sample, respectively. The decay in the chemical shift

continues until 73% PFOT is in the ligand shell. Similar to Figure 2.15a the rapid decay

from 25-73% PFOT suggests a growing interface between the DDT and PFOT ligands.

Finally, another plateau is observed from 75-100% PFOT suggesting a constant local

environment for the PFOT ligand.

59

The vertical lines present in Figure 2.15a and b represent the predicted onset of the elongated patch and stripe-like domain suggested by the ^{19}F NMR experiments and theoretical modelling studies by Pasquato *et. al.*[32] The rapid decay observed in Figure 2.14 fits well within the expected region of stripe-like domain formation. If stripe-like domains were being formed then a large increase in the interface between the DDT and PFOT would occur, this would coincide with a decay in the chemical shift. The results found during the ^{19}F NMR studies of the ML-FNPs support this finding. The plateau regions observed also match well with the results shown in Figure 2.13. Here, patchy domains are expected and would exhibit a fairly steady chemical shift as the local environment in influenced by the fluorinated ligand alone.

Table 2.3 19F NMR shift results for the CF3 and 7th CF2 unit of the PFOT ligand.

NP Batch	CF$_3$ Shift (ppm)	7th CF$_2$ (ppm)
0F	-	-
7F	-81.80	-126.75
15F	-81.81	-126.76
20F	-82.00	-126.78
25F	-81.85	-126.91
31F	-82.07	-127.05
32F	-82.05	-127.02
39F	-82.09	-127.08
48F	-82.27	-127.39
52F	-82.32	-127.18
53F	-82.26	-127.35
58F	-82.43	-127.45
59F	-82.33	-127.20
73F	-82.59	-127.25
75F	-82.46	-127.54
93F	-82.52	-127.54
100F	-82.54	-127.54

Some fluctuations in the chemical shift of the synthesized ML-FNPs are noted, specifically the 20F and 73F samples in 2.15a and the 73F sample in 2.15b, respectively. This may be attributed to the difference in size of the NPs used in both studies. The NPs used for Figures 2.9-12 had an average diameter of 2-4 nm while the ML-FNP series have a diameter of 1.7-2.1 nm, respectively. The slight increase in the surface curvature may be enough to shift the window of observed stripe-like domain formation. For example, the 25F-NPs exhibits a rapidly decaying chemical shift (Figure 2.15b), the decay found in Figure 2.13 does not begin until the ligand shell has over 30% fluorinated ligand. The similarities between Figure 2.13 and 2.15 were expected as the ligand mixtures used are identical. Therefore, the results of the ^{19}F NMR study suggest the ML-FNPs synthesized exhibit patchy and stripe-like morphologies similar to the analogous NP system.[32]

QCM quantification of molecule-NP interactions

A custom QCM apparatus was constructed to quantify molecule-NP interactions. Each NP-film was prepared directly on a quartz crystal by spin coating NP solutions. The NP-film was subsequently exposed to solvent vapor and the mass uptake was quantified by the shifting resonant frequency of the quartz crystal. An advantage of QCM is rapid real-time feedback with high mass-resolution, the use of minute NP quantities, and the ability to measure molecule uptake without requiring a solvation sphere. A schematic of the QCM apparatus (Figure 2.16a) shows the QCM crystal coated with the ML-FNP film located inside of a chamber with two ports. The chamber used was 0.2L glass jar a copper inlet for the molecule vapor and a copper outlet line. The chamber was housed inside of a temperature-controlled environment to ensure a constant temperature during the
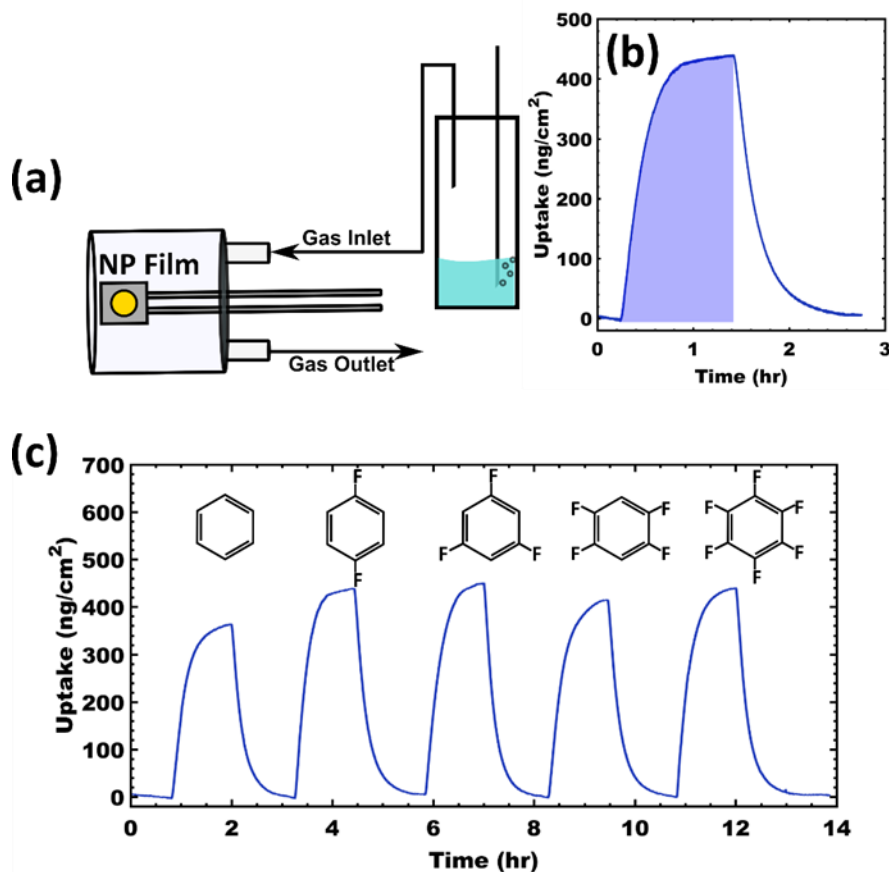
Figure 2.16 (a) Scheme of QCM setup with controlled solvent vapor. (b) A characteristic vapor response curve for the 0F NP film with 1,4-Difluorobenzene where the shaded region represented the solvent uptake. (c) A sequential series of solvent measurements for a 0F NP film with benzene, 1,4-difluorobenzene, 1,3,5-trifluorobenzene, 1,2,4,5-tetrafluorobenzene, and hexafluorobenzene vapor, respectively.

measurements as QCM crystals are also sensitive for thermal fluctuations. The temperature of the molecule bubbler was also held constant to ensure as little temperature fluctuation as possible. As the solvent was generated it entered the temperature-controlled chamber and was fed through 12 feet of hand coiled copper tubing to give ample time for temperature equilibration of the solvent vapor before entering the QCM chamber. The outlet was fed into a fume hood as most of the solvent vapors are toxic.

Early experiments guided our selection of films that were approximately 60 nm thick or less to minimize diffusion time. This thickness was consistently achieved by using a 1 wt% NP solution and a spin speed of 5000 rpm for an even, thin film on the crystal surface. Slower spin speeds (<2000 rpm) resulted in >100 nm thick films with excessive equilibration times. For typical experiments, the frequency response to vapor was exponential with a time constant that ranged for each film from 8-14 minutes. A typical uptake experiment is shown in Figure 2.16b. The uptake of the molecule vapor is tracked real time through changes in the resonant frequency of the QCM crystal. This allows for immediate feedback on the molecule-NP interactions. Using the change in frequency the mass of molecule vapor uptake for each molecule can be calculated using the Z-match method listed in the experimental section. Comparison of the molecule mass uptake to that of the NP-film thus quantifies the relative extent of uptake. The experiment is easily extendable by examining multiple molecule vapors sequentially (Figure 2.16c). To change solvents dry air was purged through the QCM chamber to remove all of the molecule vapor and to return the baseline of the QCM crystal back to the original value recorded at the start of the experiment. During this purge cycle the chamber housing the solvent is isolated and can be interchanged for a new container with the solvent of choice that will be analyzed next. The five solvents used were benzene, 1,4-difluorobenzene, 1,3,5-trifluorobenzene, 1,2,4,5-tetrafluorobenzene, and hexafluorobenzene. All of the molecule vapor series experiments yielded similar curves to the one highlighted in Figure 2.16c. The complete list of molecule vapor series for Each ML-FNP composition can be found in Figures A1-9, The results of these series can be found in Table 2.4. All of the ML-FNPs had a similar mass spun onto the QCM crystal. As stated previously the

amount of molecule uptake will be normalized by the ML-FNP film mass to account for small differences in the film mass. The total molecule vapor uptake for the five solvents is also provided in Table 2.4.

Table 2.4 Mass of the NP films and the molecule uptake measured for each benzene derivative

	Film Mass (g/cm^2)	Estimated Film Thickness $(nm)*$	Ben. (g/cm^2)	Difluoro. (g/cm^2)	Trifluoro. (g/cm^2)	Tetrafluoro. (g/cm^2)	Hexafluoro. (g/cm^2)
0F	2.396E-06	24	3.636E-07	4.380E-07	4.485E-07	4.142E-07	4.399E-07
20F	1.268E-06	13	3.554E-07	4.194E-07	4.338E-07	3.742E-07	4.378E-07
31F	4.486E-06	45	1.216E-06	1.079E-06	1.089E-06	8.552E-07	7.904E-07
39F	5.308E-06	53	5.360E-07	6.497E-07	6.970E-07	6.220E-07	7.192E-07
52F	2.534E-06	25	3.178E-07	3.993E-07	4.422E-07	3.801E-07	4.709E-07
59F	4.566E-06	46	4.994E-07	6.439E-07	6.880E-07	6.282E-07	7.155E-07
73F	3.002E-06	30	7.049E-07	7.887E-07	7.683E-07	8.876E-07	8.446E-07
93F	2.322E-06	23	4.537E-07	5.637E-07	6.075E-07	5.320E-07	5.789E-07
100F	4.387E-06	44	5.057E-07	6.450E-07	8.067E-07	7.587E-07	9.451E-07

Typical experiments yielded 10-35% molecule mass uptake relative to the film mass. To account for variability in molecule uptake repeated measurements were performed. The repeated measurements exhibited 2-10% variation of the absolute uptake values, Table 2.5. The error in calculated in Table 2.5 is included in the plots of molecular uptake vs. PFOT% in the ligand shell. The highest error of 10% was used for the error bars. Molecular uptake values that are within the error bars of another ML-FNP composition will not be considered as a significant change in the molecular interactions.

The effect of ligand morphology on molecular uptake are presented next by comparison of the QCM response of NPs with different mixed ligand compositions.

Table A.5 Data from repeated measurements of molecule vapor uptake into NP films. including statistical variation.

0F NP: Hexafluoro.	Run Number	Relative Uptake Value ($g_{solvent}/g_{film}$)
	1	0.1145
	2	0.1023
	Mean and Stdev	0.1084±0.0087 (8.01%)
43F NP: Hexafluoro.	Run Number	Relative Uptake Value ($g_{solvent}/g_{film}$)
	1	0.00460096
	2	0.004770584
	3	0.004562336
	Mean and Stdev	0.0046±.0001 (2.39%)
43F NP: Trifluoro.	Run Number	Relative Uptake Value ($g_{solvent}/g_{film}$)
	1	0.001988694
	2	0.001890374
	3	0.001713936
	Mean and Stdev	.0019±.0002 (7.47%)
62F NP: Hexafluoro.	Run Number	Relative Uptake Value ($g_{solvent}/g_{film}$)
	1	0.003707888
	2	0.004466173
	3	0.004498251
	Mean and Stdev	.0042±.0005 (10.59%)
62F NP: Trifluoro.	Run Number	Relative Uptake Value ($g_{solvent}/g_{film}$)
	1	0.005478482
	2	0.005274893
	3	0.005126597
	Mean and Stdev	.0053±.0002 (3.34%)

Correlation of ligand morphology to molecule-NP interactions

The simplest approach for series comparisons of molecule-NP interactions is with variable NPs and constant molecule vapor. This eliminates the need to quantify and vary the vapor pressure for direct molecule comparisons.[53] A distinct benefit of our QCM method is the quantification of molecule-NP interactions for non-solvents. The systematic series of mixed ligand NPs prepared above are ideal candidates for the

65

development and testing of this new QCM based approach to probe for non-monotonic trends in molecule – NP interactions with changes to the ligand composition and thus ligand morphology. Our synthesis strategy notably eliminates the nanoparticle size distribution as a variable by using a ligand exchange strategy. Recent experimental and computational work coupled with our ^{19}F NMR measurements suggests a sequence of patchy and stripe-like morphologies here.

First, the uptake of benzene vapor was systematically examined using a range of NP surface compositions (Figure 2.17). NPs with only DDT ligands up took 15 wt% benzene mass and NPs with only PFOT ligands up took 11 wt% benzene mass. These
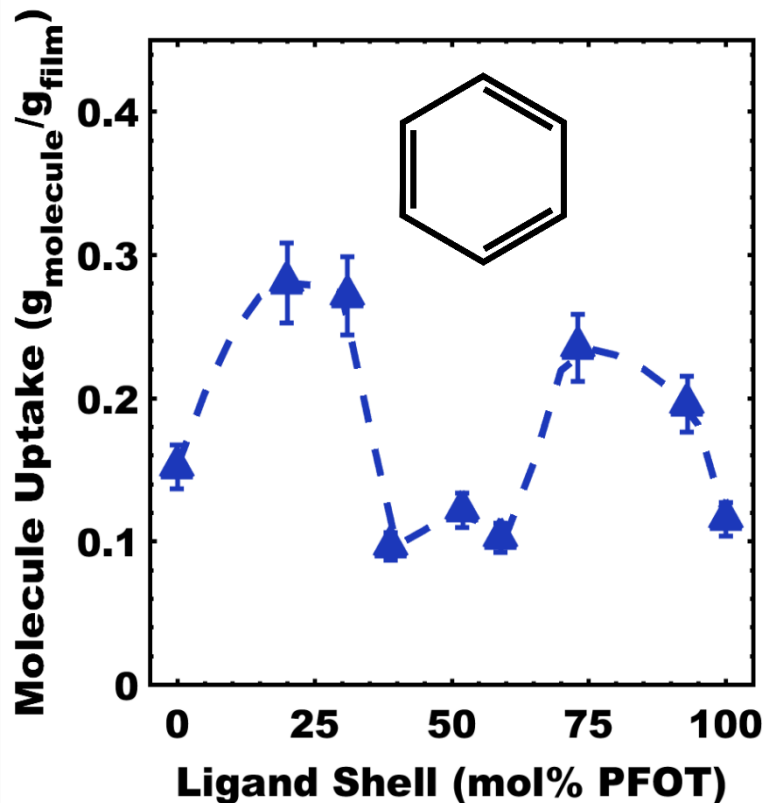
Figure 2.17 Mass uptake of benzene vapor in NP films as a function of PFOT:DDT mixed ligand shell composition.

two extreme points constrain the possible trajectories for monotonic behavior trends to be in intermediate to these two values. If the composition alone dictated the molecular interactions the uptake of benzene is expected to slowly decrease as the PFOT% in the ligand shell is increased, due to benzene and PFOT being highly dissimilar. The ML-FNPs with stripe-like morphologies (39 – 59 mol% PFOT, Figure 2.15) exhibited reduced solvent uptake relative to the two mono-ligand cases, indicative of molecular cavitation. The stripe-like morphology would have a large interface between the DDT and PFOT. The PFOT ligand, more phobic to the benzene, would be shielded by the taller DDT filling the free volume above the shorter ligand. This would restrict access to these regions of the ligand shell and reduce the extent of cavitation similar to phenomena documented before.[13] In contrast, the NPs used here with patchy morphologies (both PFOT-poor and PFOT-rich) exhibited markedly enhanced uptake, indicative of molecular confinement. For example, the 20F NPs up took 28 wt% benzene, a $\sim$2$\times$ increase relative to the 0F NPs despite the addition of a fluorophile. This is similar to the phenomena observed in a similar system where the wider patchy domains were less confined allowing for more solvent to interact with the ligand shell.[13] Clearly, the molecule-NP interaction is sensitive to the character of the ligand morphology. We note that ^{19}F NMR of the 31F-NP was at a transition between patchy and stripe-like morphologies and was thus excluded from discussion of generalized trends due to ambiguity. The trends in uptake may be attributed to the nominal dimension of the ligand domains, increasing when transitioning from stripe-like to patchy morphologies. Molecular confinement, *e.g.* within the gaps between the short and tall ligands, requires that the ligand domains

accommodate both the molecule functionality and dimensions. This was rationalized with a confinement argument in a prior study.[19]

An interesting feature is that even the 100F NPs with mono-ligand PFOT up took 11 wt% benzene; this interaction of benzene would be missed by solubility measurements alone as the 100F NPs are nearly insoluble in benzene. This marked difference between solubility measurements and QCM solvent uptake exhibit the distinction between molecular uptake and the capability to form a favorable solvation shell. Thus, QCM
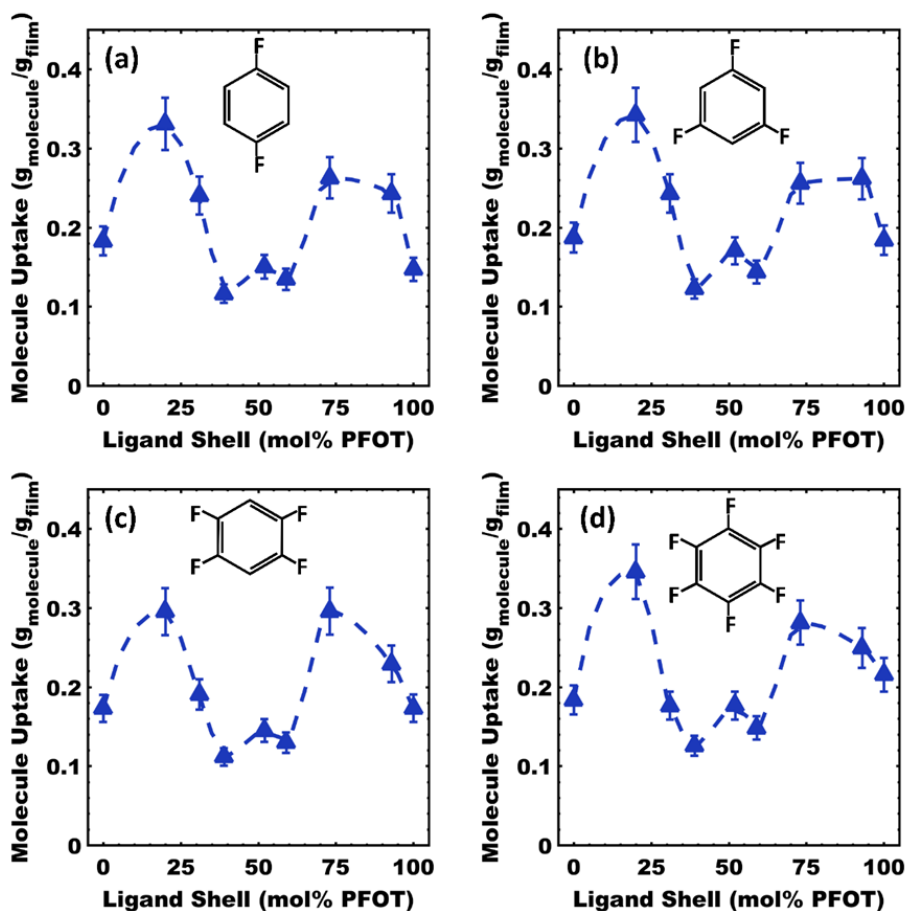
Figure 2.18 Mass uptake of solvent vapors in NP films as a function of PFOT:DDT mixed ligand shell composition. (a) 1,4-difluorobenzene, (b) 1,3,5-trifluorobenzene, (c) 1,2,4,5-tetrafluorobenzene, and (d). Guide lines are indicated with dashes.

enables additional insights to quantify molecule-NP interactions independent of solubility. This capability can possibly be transitioned into determining the interactions of the ML-FNPs with various monomers to obtain a greater understanding of polymer-NP interactions.

Next a systematic series of benzene derivatives were examined with variable extent of fluorination to determine the effect on overall molecule-NP interactions. The derivatives included 1,4-difluorobenzene, 1,3,5-trifluorobenzene, 1,2,4,5-tetrafluorobenzene, and hexafluorobenzene and were deliberately selected without permanent molecular dipoles. Each solvent was examined across the same series of NP compositions and morphologies as above with benzene (Figure 2.18 and Table 2.4). Analogous behavior to benzene was found in all cases where (1) relative to the mono-ligand cases, the patchy NPs exhibited enhanced uptake corresponding to confinement effects and (2) relative to the mono-ligand cases, the stripe-like NPs exhibited reduced solvent uptake corresponding to cavitation effects. Similarly, large changes in nanoparticle solubility by 230-250% were reported for minor composition changes of mixed ligand shells from 8-17 mol%.[19] These generalized behaviors for the aromatic molecule series suggests an important role of the relatively constant molecular shape, size, and presence of the aromatic ring.

As expected with a like-dissolves-like argument, the 0F sample exhibited more uptake of benzene than the 100F, whereas the 100F exhibited more uptake of highly fluorinated (low Hildebrand parameter) benzene derivatives (Figure 2.19). The uptake of hexafluorobenzene is nearly doubled compared to benzene. The systematic increase of fluorine content in the benzene derivatives coincides with a linear increase in the
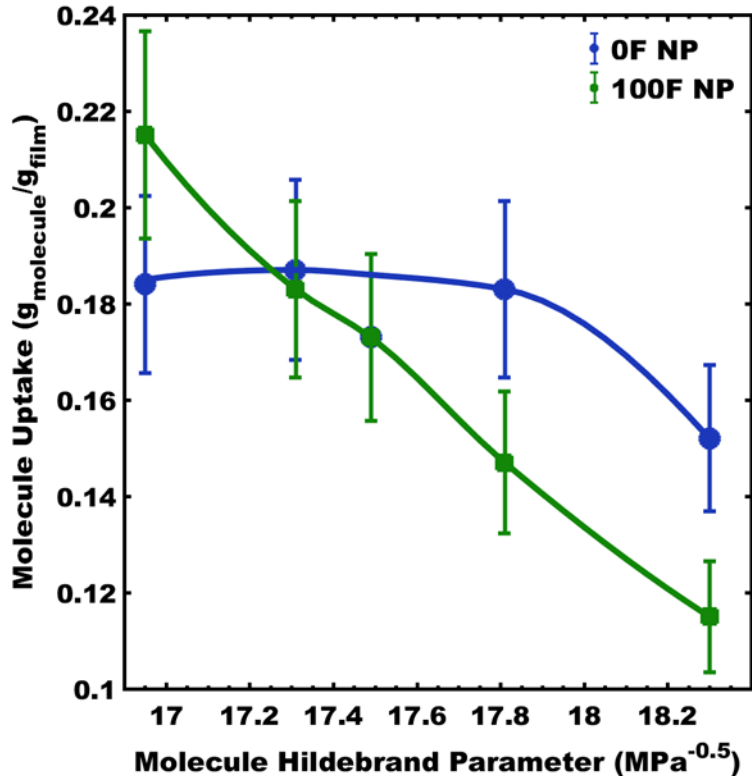
Figure 2.19 Comparison of different benzene derivative uptakes into the 0F and 100F NP films. The Hildebrand solubility parameter for each benzene derivative is used for the x-axis. Comparisons of 0F and 100F NP films are implied, whereas comparisons between particular molecules also include changing vapor pressure.

molecule uptake. These results are consistent with ESR measurements performed on fluorinated mixed ligand NPs in which the monolayers had much stronger binding affinity to highly fluorinated probes compared to the non-fluorinated counterpart.[54] The favorable interaction of PFOT with fluorinated benzene derivatives may be due to either a reduced difference in relative polarizability (dispersion forces) or possibly the presence of weak halogen bonding. Other studies have shown that weakly attractive interactions exist between fluorinated alkanes and electron deficient aromatics.[55,56] Another important observation is the slight increase in uptake for the fluorinated benzene derivatives in the

70

0F-NPs compared to benzene. Although a higher fluorine content should make the derivatives more chemically dissimilar to the lipophilic DDT the Hildebrand solubility parameter does decrease. Hexane, a common lipophilic solvent similar in structure to the DDT ligand has a Hildebrand near 15 MPa$^{-0.5}$. The slight decrease in the Hildebrand may cause the small yet significant uptake.

This newly developed QCM based tool can be implemented in tandem with current analytical methods to probe the NP ligand shell. Currently the morphology of an individual NP cannot be determined but measurements can probe a population NPs to suggest the formation of phase separated domains. Theoretical studies have reinforced the findings that morphologies can be formed in the ligand shell. However, limited quantitative experimental methods have been employed. The ability to record mass uptake of varying molecule vapors on the nanogram scale shows the powerful capabilities of a QCM. In this study it was used to identify behavior consistent with a patterned ligand shell and support ^{19}F NMR measurements that suggested the formation of patchy and stripe-like domains. QCM thus quantifies non-monotonic trends for molecule-NP interactions that are influenced by possible contributions from size/shape, ligand morphology, and chemical nature. This QCM methodology will enable future studies of structure-property relationships for molecule interactions with mixed ligand NPs. This capability is crucial to support further investigations into the molecular mechanisms.

2.5 Conclusions

Synthetic methods to directly synthesize the PFOT NPs failed due to the fluorophobic effect making the as-made NPs insoluble in the reaction media. To overcome this issue NPs ligated with weaker binding amine ligands were synthesized and a mixed ligand

71

shell was achieved through ligand displacement. The ligand displacement approach was able to generate NPs with high PFOT content while maintaining a constant size as determined by SAXS. The ratio of the DDT and PFOT in the ligand shell was determined through NMR of stripped NPs. Though this is a destructive method a standard can be added to the solution to simultaneously determine the total concentration of ligands avoiding the need for TGA and ultimately saving large amounts of sample. The morphology of the NPs was determined through a 19F NMR method that utilized the PFOT in the ligand shell. The ML-FNPs exhibit a patchy ligand shell at low and high percentages of PFOT in the ligand shell. Highly interesting stripe-like domains were observed for ML-FNPs with 30-60% PFOT in the ligand shell. A method to quantify mixed ligand shell molecule-NP interactions was developed that is independent of solvation criteria. A QCM apparatus was used to measure the vapor phase uptake of molecules into solid NP thin films. The NPs uptake was measured with a systematic series of fluorinated benzene derivatives. The relative mass uptake was non-monotonic with NP ligand shell composition in all cases. For the cases examined, patchy ligand morphologies were found to exhibit more molecule uptake than either stripe-like or the analogous mono-ligand NPs. This enhanced uptake was attributed to confinement effects. In contrast, stripe-like morphologies exhibited decreased molecule uptake relative to the mono-ligand NPs, consistent with cavitation effects. These results highlight the role of ligand shell morphology on molecule-NP interactions. Notably the technique enabled measurements with non-solvents as the NPs are analyzed in the solid state allowing for quantification of interactions with non-solvents. The ability to measure interactions without a solvation shell leads to a more complete understanding of molecule-NP

72

interactions. The QCM based method is easily adaptable to numerous NP-molecule systems and can be used in tandem with currently available analytic techniques. Lastly, the enhanced uptake of ML-FNPs exhibiting a patchy morphology show promise for utilization of the fluorophobic effect. By using the enhanced interactions of patchy ML-FNPs the insolubility in common organic solvents may be overcome. These regions of the composition map could be a powerful handle to tune the solubility while maintaining the fluorophobic properties needed for coassembly which will be discussed in Chapter 3.

2.6 References

1. Eustis, S.; El-Sayed, M. A. *Chem. Soc. Rev.* **2006**, *35*, 209–217.

2. Saha, K.; Agasti, S. S.; Kim, C.; Li, X.; Rotello, V. M. *Chem. Rev.* **2012**, *112*, 2739–2779.

3. Ghosh, P.; Han, G.; De, M.; Kim, C. K.; Rotello, V. M. *Adv. Drug Deliv. Rev.* **2008**, *60*, 1307–1315.

4. Nie, Z.; Petukhova, A.; Kumacheva, E. *Nat. Nanotechnol.* **2010**, *5*, 15–25.

5. Aragay, G.; Pons, J.; Merkoçi, A. *Chem. Rev.* **2011**, *111*, 3433–3458.

6. Niu, H.; Wang, S.; Zhou, Z.; Ma, Y.; Ma, X.; Cai, Y. *Anal. Chem.* **2014**, *86*, 4170–4177.

7. Uzun, O.; Hu, Y.; Verma, A.; Chen, S.; Centrone, A.; Stellacci, F. *Chem. Commun.* **2008**, 2, 196–198.

8. Bidoggia, S.; Milocco, F.; Polizzi, S.; Canton, P.; Saccani, A.; Sanavio, B.; Krol, S.; Stellacci, F.; Pengo, P.; Pasquato, L. *Bioconjugate Chem.* **2017**, *28*, 43–52.

9. Stranick, S. J.; Parikh, A. N.; Tao, Y. T.; Allara, D. L.; Weiss, P. S. *J. Phys. Chem.* **1994**, *98*, 7636–7646.

10. Folkers, J. P.; Laibinis, P. E.; Whitesides, G. M. *Langmuir* **1992**, *8*, 1330–1341.

11. Laibinis, P. E.; Fox, M. A.; Folkers, J. P.; Whitesides, G. M. *Langmuir* **1991**, *7*, 3167–3173.

12. Imabayashi, S.; Gon, N.; Sasaki, T.; Hobara, D.; Kakiuchi, T. *Langmuir* **1998**, *14*, 2348–2351.

13. Kuna, J. J.; Voïtchovsky, K.; Singh, C.; Jiang, H.; Mwenifumbo, S.; Ghorai, P. K.; Stevens, M. M.; Glotzer, S. C.; Stellacci, F. *Nat. Mater.* **2009**, *8*, 837–842.

14. Pons-Siepermann, I. C.; Glotzer, S. C. *ACS Nano* **2012**, *6*, 3919–3924.

15. Kim, H.; Carney, R. P.; Reguera, J.; Ong, Q. K.; Liu, X.; Stellacci, F. *Adv. Mater.* **2012**, *24*, 3857–3863.

16. Ghorai, P. K.; Glotzer, S. C. *J. Phys. Chem. C* **2010**, *114*, 19182–19187.

17. Jackson, A. M.; Myerson, J. W.; Stellacci, F. *Nat. Mater.* **2004**, *3*, 330–336.

18. Edwards, W.; Marro, N.; Turner, G.; Kay, E. R. *Chem. Sci.* **2017**, *9*, 125–133.

19. Centrone, A.; Penzo, E.; Sharma, M.; Myerson, J. W.; Jackson, A. M.; Marzari, N.; Stellacci, F. *Proc. Natl. Acad. Sci. U. S. A.* **2008**, *105*, 9886–9891.

20. Şologan, M.; Cantarutti, C.; Bidoggia, S.; Polizzi, S.; Pengo, P.; Pasquato, L. *Faraday Discuss.* **2016**, *191*, 527–543.

21. Stangenberg, R.; Saeed, I.; Kuan, S. L.; Baumgarten, M.; Weil, T.; Klapper, M.; Müllen, K. *Macromol. Rapid Commun.* **2014**, *35*, 152–160.

22. Segets, D.; Gradl, J.; Taylor, R. K.; Vassilev, V. *ACS Nano* **2009**, *3*, 1703–1710.

23. Stebounova, L. V; Guio, E.; Grassian, V. H. Silver *J. Nanopart. Res.* **2011**, *13*, 233–244.

24. Zamborini, F. P.; Leopold, M. C.; Hicks, J. F.; Kulesza, P. J.; Malik, M. A.; Murray, R. W. *J. Am. Chem. Soc.* **2002**, *124*, 8958–8964.

25. Joseph, Y.; Peie, A.; Chen, X.; Michl,J.; Vossmeyer, T.; Yasuda, A. *J. Phys. Chem. C*, **2007**, *111*, 12855 – 12859.

26. Im, J.; Chandekar, A.; Whitten, J. E. *Langmuir* **2009**, *25*, 4288–4292.

27. Ibañez, F. J.; Zamborini, F. P. *Small* **2012**, *8*, 174–202.

28. Hao, R.Z.; Song, H.B.; Zuo, G.M.; Yang, R.F.; Wei, H.P.; Wang, D.B.; Cui, Z.Q.; Zhang, Z.; Cheng, Z.X.; Zhang, X.E. *Biosens. Bioelectron.* **2011**, *26*, 3398–3404.

29. Pavlov, V.; Xiao, Y.; Shlyahovsky, B.; Willner, I. *J. Am. Chem. Soc.* **2004**, *126*, 11768–11769.

30. Ding, Y.; Liu, J.; Wang, H.; Shen, G.; Yu, R. *Biomaterials* **2007**, *28*, 2147–2154.

31. Lesniak, A.; Salvati, A.; Santos-Martinez, M. J.; Radomski, M. W.; Dawson, K. A.; Åberg, C. *J. Am. Chem. Soc.* **2013**, *135*, 1438–1444.

32. Şologan, M.; Marson, D.; Polizzi, S.; Pengo, P.; Boccardo, S.; Pricl, S.; Posocco, P.; Pasquato, L. *ACS Nano* **2016**, *10*, 9316–9325.

33. Liu, X.; Atwater, M.; Wang, J.; Huo, Q. *Colloids Surf., B* **2007**, *58*, 3–7.

34. Smith, A. M.; Johnston, K. A.; Crawford, S. E.; Marbella, L. E.; Millstone, J. E. *Analyst* **2017**, *142*, 11–29.

35. Zheng, N.; Fan, J.; Stucky, G. D. *J. Am. Chem. Soc.* **2006**, *128*, 6550–6551.

36. Singh, C.; Ghorai, P. K.; Horsch, M. A.; Jackson, A. M.; Larson, R. G.; Stellacci, F.; Glotzer, S. C. *Phys. Rev. Lett.* **2007**, *99*, 1–4.

37. Carney, R. P.; DeVries, G. A.; Dubois, C.; Kim, H.; Jin, Y. K.; Singh, C.; Ghorai, P. K.; Tracy, J. B.; Stiles, R. L.; Murray, R. W.; Glotzer, S. C.; Stellacci, F. *J. Am. Chem. Soc.* **2008**, *130*, 798–799.

38. Hostetler, M. J.; Green, S. J.; Stokes, J. J.; Murray, R. W. *J. Am. Chem. Soc.* **1996**, *118*, 4212–4213.

39. Brown, L. O.; Hutchison, J. E. *J. Am. Chem. Soc.* **1997**, *119*, 12384–12385.

40. Luo, Z.; Hou, J.; Menin, L.; Ong, Q. K.; Stellacci, F. *Angew. Chem. Int. Ed.* **2017**, *56*, 13521–13525.

41. Jana, N. R.; Peng, X. *J. Am. Chem. Soc.* **2003**, *125*, 14280–14281.

42. Schnablegger, H.; Yashveer, S. *The SAXS Guide*, 4th ed.; Anton Paar GmbH, 2017.

43. Dass, A.; Guo, R.; Tracy, J. B.; Balasubramanian, R.; Douglas, A. D.; Murray, R. W. *Langmuir* **2008**, *24*, 310–315.

44. Yonezawa, T.; Onoue, S.; Kimizuka, N. *Adv. Mater.* **2001**, *13*, 140–142.

45. Liu, X.; Yu, M.; Kim, H.; Mameli, M.; Stellacci, F. *Nat. Commun.* **2012**, *3*, 1182–1189.

46. Pradhan, S.; Brown, L. E.; Konopelski, J. P.; Chen, S. *J. Nanopart. Res.*, **2009**, *11*, 1895-1903.

47. Harkness, K. M.; Balinski, A.; McLean, J. A.; Cliffel, D. E. *Angew. Chem. Int. Ed.* **2011**, *50*, 10554–10559.

48. Hu, Y.; Wansch, B. H.; Sahni, S.; Stellacci, F. *J. Scanning Probe Microsc.* **2009**, *4*, 24–35.

49. Wang, Y.; Zeiri, O.; Neyman, A.; Stellacci, F.; Weinstock, I. A. *ACS Nano* **2012**, *6*, 629–640.

50. Lucarini, M.; Pasquato, L. *Nanoscale* **2010**, *2*, 668-676.

51. Centrone, A.; Hu, Y.; Jackson, A. M.; Zerbi, G.; Stellacci, F. *Small* **2007**, *3*, 814–817.

52. Pradhan, S.; Xu, L. P.; Chen, S. *Adv. Funct. Mater.* **2007**, *17*, 2385–2392.

53. Emerson, J. A.; Toolan, D. T. W.; Howse, J. R.; Furst, E. M.; Epps, T. H. *Macromolecules* **2013**, *46*, 6533–6540.

54. Boccalon, M.; Bidoggia, S.; Romano, F.; Gualandi, L.; Franchi, P.; Lucarini, M.; Pengo, P.; Pasquato, L. *J. Mater. Chem. B* **2015**, 3, 432–439.

55. Kawahara, S. I.; Tsuzuki, S.; Uchimaru, T. *J. Phys. Chem. A* **2004**, *108*, 6744–6749.

56. Cavallo, G.; Metrangolo, P.; Milani, R.; Pilati, T.; Priimagi, A.; Resnati, G.; Terraneo, G. *Chem. Rev.* **2016**, *116*, 2478–2601.

CHAPTER 3

CONTROLLED ASSEMBLY OF MIXED LIGAND FLUORINATED
NANOPARTICLES UTILIZING THE FLUOROPHOBIC EFFECT

3.1 Abstract

The fluorophobic effect is the phase separation of fluorinated materials from both hydrophilic and lipophilic systems. This has been utilized in block copolymer (BCP) self-assembly as fluorinated BCPs have very high interaction parameters. These properties enable the fluorophobic effect to be a potential handle to control the cooperative assembly of fluorinated materials with BCP systems. Utilizing mixed ligands, the behavior of metal nanoparticles (NPs) can be tuned. Herein, mixed ligand fluorinated NPs (ML-FNPS) will be used to tune the fluorophobic effect as a function of fluorine in the ligand shell. ML-FNPs with varying fluorine content were synthesized and dispersed in poly(styrene) and poly(perfluorooctyl acrylate) homopolymers (H-PS and H-PFOA) at various volume loading percentages. Small angle X-ray scattering (SAXS) of the ML-FNPs in the H-PS revealed aggregate formation at 0.05 volume loading percent with as little as 25% perfluorooctyl thiol (PFOT) in the ligand shell; while an increase the PFOT content lead to enhanced dispersion in the H-PFOA matrix with form factor scattering features being observed at a 0.74 volume loading percent for the highly perfluorinated NPs. Coassembly experiments of the ML-FNPs with a PS-*b*-PFOA diblock copolymer revealed similar results to the dispersion studies. SAXS and transmission electron microscopy (TEM) analysis revealed assembly of the FNPs at the interface between the PS and PFOA domains with as little as 25% PFOT in the ligand shell. As the PFOT content reached 75% and above the FNPs were pushed away from the interface and into the PFOA domains. Utilizing the strength of the fluorophobic effect shown in the diblock copolymer system preliminary multimodal coassembly experiments were performed with an amphiphilic poly(ethylene oxide-*b*-styrene-*b*-perfluorooctyl acrylate) (PEO-*b*-PS-*b*-

PFOA) triblock terpolymer, titania, and the 75F-NPs. SAXS analysis revealed a 10 nm increase in the polymer d-spacing while the primary scattering feature is preserved.

3.2 Introduction

Fluorine modification has become widespread in materials science due to the low surface energies,[1] chemical resistance,[2] and various other properties.[3] One of the most widely used properties is the segregation of fluorinated materials from both hydrophilic and lipophilic phases, often referred to as the fluorophobic effect.[4] It has been used to order liquid crystals,[5] dendrimers,[6] and has assisted in generating long range order in polymer films.[7] Even homopolymer blends that macrophase separate exhibit block copolymer (BCP) like behavior through the segregation of small fluorinated tails.[8]

This remarkable behavior has been incorporated into BCP systems to enhance phase separation. Amphiphilic BCPs can undergo thermodynamically driven self-assembly to decrease the amount of unfavorable interactions, reducing the energy of the system.[9,10] This can lead to the formation of ordered polymer phases, known as morphologies, where the two polymer blocks are separated into distinct domains.[11] The inclusion of fluorine through direct synthesis or *via* chemical modification has been shown to induce stronger phase separation by increasing the chemical dissimilarity of the blocks.[12] The strong phase separation exhibited by fluorinated BCPs has been used in bulk films and in solution to attain multicompartment micelles with three distinct chemical phases.[13,14]

One area where the fluorophobic effect has yet to be utilized is in controlling inorganic nanoparticles (NPs) during the process of BCP coassembly. The use of BCPs as a structuring agent began in 1997 when the self-assembly of poly(isoprene-*b*-ethylene

79

oxide) structured an aluminosilicate precursor.[15] During the self-assembly process, selective intermolecular interactions like hydrogen bonding are used to direct the material to the desired block creating ordered nanocomposites. Hydrogen bonding interactions have successfully structured nanoparticles,[16,17] transition metal oxides,[18-20] and small organic precursors of polymeric resins.[21,22] Even amphiphilic triblock terpolymers have been used to generate complex morphologies with control over the loading of the inorganic material.[23,24] Hydrophilic interactions, like hydrogen bonding, rely on a donor-acceptor based system to pull the material to the correct domain. Here, the acceptor is the hydrophilic polymer block, an example being poly(ethylene oxide), which has heteroatoms like oxygen. The lone pairs of the heteroatom can then interact and pull the hydrogen bond donor into the hydrophilic domain as the BCP self-assembles. Since the inception of BCP coassembly only hydrophilic interactions have been successfully utilized.

In the past hydrophobic interactions have been tested as another possible handle for coassembling inorganic materials with BCPs. Here, metal NPs coated with long chain alkyl thiols or grafted polymer chains have been combined with BCPs containing hydrophobic blocks. When small alkyl thiols are used aggregation occurs and the metal NPs do not disperse in the BCP.[25] Metal NPs coated with long chain alkyl thiols, often 18 carbons or greater, assemble at the interface of the BCP domains and have only been loaded to 2 volume % metal.[26] Thiol functionalized polymer chains grafted to the surface of metal NPs have allowed for successful coassembly away from the interface but suffer from low metal loading percentages.[27] One approach, utilizing small molecules guides, has achieved high metal loading percentages through hydrophobic interactions. In these

80

systems 3-n-pentadecylphenol (PDP) was combined with alkyl thiol coated metal NPs and a poly(styrene-b-4-vinylpyridine) (PS-*b*-P4VP) BCP.[28,29] The PDP formed a hydrogen bonding network with the P4VP block to form a phase separated hydrophobic microdomain inside the P4VP block. The alkyl thiol coated NPs were then segregated to this domain and loadings up to 70% were achieved before structuring was lost. If the PDP was not present the metal NPs would aggregate and be expelled from the BCP. Although this method has enabled structuring of metal NPs it still relies on hydrogen bonding interactions.

In order to attain multimodal coassembly, where two populations of nanoparticles can be selectively guided to two phases of material, a new intermolecular interaction orthogonal to hydrogen bonding is needed. The key to multimodal coassembly is directing two populations of NPs to two chemically distinct domains, this would allow for high control over the exact location of NP loading with no cross-over. This is a distinct process from triconstituent coassembly, where two or more populations of materials are loaded into the same domain of a BCP system, which has been accomplished before.[30] To do this an intermolecular interaction that is orthogonal to hydrogen bonding is needed. One possible interaction that has orthogonality is the fluorophobic effect. Since fluorinated materials are immiscible in hydrophilic and lipophilic phases the fluorophobic effect could be utilized to selectively load NPs in fluorinated domains. If successful, the fluorophobic effect could be employed in tandem with hydrogen bonding interactions to achieve multimodal coassembly.

For the fluorophobic effect to be a viable handle for coassembly four criterion must be met. First, the inorganic material must have a selective interaction with a single

block to facilitate loading and not phase separation from the BCP. Second, the inorganic NP used must have a small diameter to avoid chain stretching which is entropically unfavorable.[31] Third, the ligands used to stabilize and direct the NP should be small to increase the volume of metal per NP.[16] Finally, the inorganic NP must have high solubility in a common solvent system. If the NP cannot be combined with the BCP system than coassembly is infeasible. The first three criterion are acheivable for the fluorophobic effect as the interaction is selective as discussed earlier. Synthetic methods are available for the synthesis of metal NPs with small diameter and perfluorinated thiols.[32] The largest hurdle is the low solubility of fluorinated materials in most common solvent systems. A method to control the solubility of the fluorinated NPs needs to be employed if the fourth and final criterion is to be met.

Mixtures of ligands have exhibited hybrid behavior in NP systems impacting properties like solubility. For example, mixed ligand NPs (ML-NPs) with extensive lipophilic or fluorine content have exhibited solubility in aqueous media.[33,34] Even with modest fluorine content ML-NPs soluble in water have exhibited accurate fluorine sensing through the fluorophobic effect.[35] Here, the addition of small amount of perfluorinated alkyl molecules induced aggregation and precipitation from the aqueous solution. The small molecules interacted with the small fluorinated thiols shielded by the long hydrophilic ligands increasing the observed fluorine content leading to precipitation. This hybrid behavior is determined by the chemical composition and morphology of the ligand shell.[36] Recently, a series of fluorinated ML-NPs (ML-FNPs) were shown to have enhanced interactions with small molecules due to the morphology of the ligand shell.[37] The ML-FNPs even had enhanced interactions with non-fluorinated solvent molecules

when the composition of the ligand shell was mostly fluorinated. These results suggest that the fluorophobic effect and solubility can be tuned using ML-FNPs to meet the final criterion of coassembly.

Herein, ML-FNPs with small perfluorooctyl thiol (PFOT) and long 1-dodecane thiol ligands (DDT) are used to tune the fluorophobic effect and solubility. First the fluorophobic effect will be evaluated through dispersion experiments of the ML-FNPs in both lipophilic poly(styrene) and fluorophilic poly(perfluorooctyl acrylate) (H-PS and H-PFOA) homopolymers. Next, the ML-FNPs were coassembled with a PS-*b*-PFOA diblock copolymer to determine the assembly behavior as a function of PFOT content in the ML-FNP ligand shell. Finally, the ML-FNPs exhibiting enhanced small molecule interactions were dispersed in THF with titania and an amphiphilic triblock terpolymer. This is the first example of multimodal coassembly accomplished by controlling the loading of two chemically distinct nanoparticle populations with hydrogen bonding and the fluorophobic effect.

3.3 Experimental Methods

Materials

Gold trichloride (99.9%) was obtained from Strem Chemical and stored under inert atmosphere. α, α, α-Trifluorotoluene (≥ 99%, TFT) and anhydrous iodine lumps (99.99%, under argon) were obtained from BeanTown Chemical. Tetrabutylammonium borohydride (≥ 98%) and didodecyldi-methylammonium borohydride (≥ 98%) were purchased from TCI America and stored under argon atmosphere before use. Methyl-2-bromopropionate (≥ 97%) was purchased from TCI America and used as received. Tris[2-(dimethylamino)ethylamine] (99%, Me$_6$TREN) was purchased from Alfa Aesar

and stored under inert atmosphere. Potassium thioacetate (98%), benzene (99%), and 1-dodecane thiol (98%, DDT) were obtained from Alfa Aesar and used as received. 1H,1H,2H,2H-Perfluoro-1-iodooctane iodide (≥ 95%) and 1H, 1H, 2H, 2H-perfluorooctan-1-ol (≥ 97%) were obtained from Matrix Scientific and used as received. Chloroform-D (99.8%) was purchased from Cambridge Isotope Laboratories Inc. and used as received. Toluene (≥ 99.5%) obtained from Fisher Chemical was subjected to four cycles of freeze – pump – thaw (FPT) and dried over molecular sieves prior to use. Acryloyl chloride (96%) and tetrahydrofuran (THF) were purchased from Fisher and used as received. Basic aluminum oxide and octyltrichlorosilane (97%) and Titanium(IV) isopropoxide (TTIP, >98%) was purchased from Acros Organics and used as received. Styrene (99%) was purchased from Acros Organics and the inhibitor was removed using a basic aluminum column just prior to use. Triethylamine (≥ 99.5%, TEA) was purchased from Millipore Sigma and used as received. Chloroform was purchased from VWR International and dried over 50 wt.% molecular sieves prior to use. Copper(I) bromide (99.99%), tin(II)-ethylhexanoate (92.5-100%), and anhydrous cyclohexane were purchased from Sigma Aldrich and stored under inert atmosphere prior to use. Poly(ethylene oxide) methyl ether (PEO, Mn = 5000 g/mol), 4-(dimethylamino) pyridine (DMAP), and N,N-dicyclohexylcarbodiimide (DCC) were purchased from Sigma Aldrich and dried in a vacuum oven prior to use. Hydrochloric acid (37%), hydrofluoric acid (48%), and dimethylformamide (DMF) were also purchased from Sigma Aldrich and used as received. Clear Electrical-Insulating grade Mica was purchased from McMaster-Carr. Silicon wafers with a 100 nm oxide layer were purchased from Silicon Quest

International. Ruthenium tetroxide 0.5% stabilized aqueous solution was purchased from Electron Microscopy Sciences and used as received.

1H, 1H, 2H, 2H-Perfluorooctyl acrylate (FOA) synthesis

In a round bottom flask 1H, 1H, 2H, 2H-perfluorooctan-1-ol and TEA were combined in a 1:1.2 molar ratio along with anhydrous and methanol-free chloroform. The reaction vessel was sealed with a rubber stopper and the vessel was sparged with flowing nitrogen to remove excess oxygen. Next the vessel was placed in an ice bath and then acryloyl chloride in a 1.2 molar ratio was added dropwise. The reaction was allowed to come to room temperature over a 12-hour period. The crude PFOA was collected and washed three times with 100 mL of deionized water to remove excess TEA and acryloyl chloride. The crude FOA was then washed with 1.65 mL of hydrochloric acid diluted with 20 mL of deionized water. The crude FOA was stabilized using methoxyphenol and was then dried over magnesium sulfate for 12 hours. The magnesium sulfate was removed using filtration and the excess chloroform was removed through evaporation before the crude thiol was purified through vacuum distillation and combined with 0.5 wt.% methoxy phenol to inhibit auto polymerization. The final purity and structure were verified using ^{1}H NMR spectroscopy (Figure 3.1).

Poly(perfluorooctyl acrylate) (PFOA) synthesis

In a common procedure, inhibitor was removed from 2 mL of FOA monomer using a column of basic alumina. The monomer was placed into a 50 mL Schlenk flask along with a stir bar. Next 26 µL of methyl-2-bromopropionate was added to the FOA monomer. The flask was then sealed with a glass stopper before excess oxygen was removed from the flask using four cycles of FPT. Under inert atmosphere solutions

containing 0.17 mg of copper(I) bromide, 7.7 µL of tin(II)-ethylhexanoate, and 6.7 µL of Me$_6$TREN were added to the polymerization solution. The flask was sealed under inert atmosphere and removed from the glovebox. The reaction was stirred for 20 minutes prior to being added to a silicone oil bath heated to 90°C. After 15 hours the flask was removed from the oil bath and cooled to room temperature before the reaction was diluted with TFT. The polymer was then purified through dialysis against TFT. The excess solvent was removed through evaporation. The molar mass was verified using ^{1}H NMR spectroscopy (Figure 3.4).

Poly(styrene-*b*-perfluorooctyl acrylate) (PS-*b*-PFOA) synthesis

Step 1: Poly(styrene) (PS-MI) macroinitiator synthesis

In a common procedure, inhibitor was removed from 22 mL of styrene monomer using a column of basic alumina. The monomer was placed into a 100 mL Schlenk flask along with a stir bar. Next 97 µL of methyl-2-bromopropionate was added. The flask was then sealed with a glass stopper before excess oxygen was removed from the flask using four cycles of FPT. Under inert atmosphere solutions containing .6 mg of copper(I) bromide, 28 µL of tin(II)-ethylhexanoate, and 24 µL of Me$_6$TREN were added to the polymerization solution. The flask was sealed under inert atmosphere and removed from the glovebox. The reaction was stirred for 20 minutes prior to being added to a silicone oil bath heated to 90°C. After 15 hours the flask was removed from the oil bath and cooled to room temperature before the reaction was diluted with chloroform. The polymer was then purified through precipitation into cold methanol and was collected after residual solvent evaporated. The molar mass dispersity was measured using GPC and the structure and molar mass were verified using ^{1}H NMR spectroscopy (Figure 3.4).

Step 2: PS-*b*-PFOA diblock copolymer synthesis

In a common procedure, inhibitor was removed from 2.1 mL of FOA monomer using a column of basic alumina. The monomer was placed into a 50 mL Schlenk flask along with a stir bar. Next the 3.12 g of the PS-MI was added in a 1:35 molar ratio to the PFOA monomer along with TFT to solvate the reaction. The monomer molarity for each polymerization was held constant at 0.46 moles of PFOA per liter of TFT. The flask was then sealed with a glass stopper before excess oxygen was removed from the flask using four cycles of FPT. Under inert atmosphere solutions containing .3 mg of copper(I) bromide, 16 µL of tin(II)-ethylhexanoate, and 14 µL of Me₆TREN were added to the polymerization solution. The flask was sealed under inert atmosphere and removed from the glovebox. The reaction was stirred for 20 minutes prior to being added to a silicone oil bath heated to 90˚C. After 24 hours the flask was removed from the oil bath and cooled to room temperature before the reaction was diluted with TFT. The polymer was then purified through precipitation into cold methanol and was collected after excess solvent was evaporated. The molar mass dispersity was measured using GPC and the structure and molar mass were verified using ^{1}H NMR spectroscopy.

Poly(ethylene oxide-b-styrene-b-perfluorooctyl acrylate) (PEO-*b*-PS-*b*-PFOA) synthesis

Step 1: PEO-Br macroinitiator synthesis

The PEO-Br macroinitiator was synthesized using a Steglich esterification.[37] A common procedure involved dissolving 2.0 grams of the dried PEO into a round bottom flask containing 100mL of anhydrous chloroform and was stirred. Next 0.21 mL of 2-bromopropionic acid was added dropwise to the stirring mixture. The round bottom flask

was placed into an ice bath before 0.99 grams of DCC and 0.195 grams of DMAP was added simultaneously. The ice bath was removed after ten minutes and the reaction was stirred overnight at room temperature. The resulting solution was gravity filtered to remove the urea byproduct and the filtrate was collected and precipitated into 500 mL of hexane chilled to 0˚C. The crude PEO-Br was then dissolved in 100 mL of chloroform and washed with a 100 mL aliquot of DI water. This process was repeated three times and the organic layer was collected and precipitated into 500 mL of hexanes chilled to 0˚C. The product was collected using gravity filtration and allowed to air dry overnight. The product was characterized using ^{1}H NMR and GPC (Figure 3.19).

Step2: Poly(ethylene oxide-b-styrene) (PEO-*b*-PS) synthesis

In a common procedure, inhibitor was removed from 10 mL of styrene monomer using a column of basic alumina. The monomer was placed into a 50 mL Schlenk flask along with a stir bar. Next the 2.0 grams of the vacuum dried PEO-Br macroinitiator was added in a 1:200 molar ratio to the styrene monomer along with 1.6 mL of dimethylformamide to solvate the reaction. The flask was then sealed with a glass stopper before excess oxygen was removed from the flask using four cycles of FPT. Under inert atmosphere solutions containing .3 mg of copper(I) bromide, 13 µL of tin(II)-ethylhexanoate, and 11 µL of Me$_6$TREN were added to the polymerization solution. The flask was sealed under inert atmosphere and removed from the glovebox. The reaction was stirred for 20 minutes prior to being added to a silicone oil bath heated to 90˚C. After 24 hours the flask was removed from the oil bath and cooled to room temperature before the reaction was diluted with chloroform. The polymer was then purified through precipitation into methanol chilled in a dry ice and isopropanol bath. The PEO-*b*-PS was

collected using gravity filtration and dried in ambient conditions. The molar mass dispersity was measured using GPC and the structure and molar mass were verified using ^{1}H NMR spectroscopy (Figure 3.19).

Step3: PEO-*b*-PS-*b*-PFOA triblock terpolymer synthesis

In a common procedure, inhibitor was removed from 1.0 mL of styrene monomer using a column of basic alumina. The monomer was placed into a 50 mL Schlenk flask along with a stir bar. Next the 3.46 grams of the vacuum dried PEO-*b*-PS macroinitiator was added in a 1:30 molar ratio to the FOA monomer along with 10.8 mL of TFT to solvate the reaction. The flask was then sealed with a glass stopper before excess oxygen was removed from the flask using four cycles of FPT. Under inert atmosphere solutions containing .1 mg of copper(I) bromide, 3.4 µL of tin(II)-ethylhexanoate, and 3.8 µL of Me$_6$TREN were added to the polymerization solution. The flask was sealed under inert atmosphere and removed from the glovebox. The reaction was stirred for 20 minutes prior to being added to a silicone oil bath heated to 90°C. After 24 hours the flask was removed from the oil bath and cooled to room temperature before the reaction was diluted with TFT. The polymer was then purified through precipitation into methanol chilled in a dry ice and isopropanol. The PEO-*b*-PS-*b*-PFOA was collected using gravity filtration and dried in ambient conditions. The crude polymer was then dialyzed against pure TFT to remove excess monomer. This process was repeated three times before the excess solvent was removed to collect the pure PEO-*b*-PS-*b*-PFOA. The molar mass dispersity was measured using GPC and the structure and molar mass were verified using ^{1}H NMR spectroscopy (Figure 3.19).

Hydrophobic substrate surface modification

In a common procedure, the substrates, mica or silicon wafers, were cut into 1x1 cm squares. The substrates were then sonicated for thirty minutes in isopropanol followed by sonication in a 1:1 molar ratio of deionized water and isopropanol. Next the substrates were subjected to thirty minutes of oxygen plasma. Under inert atmosphere the substrates were placed into a glass jar and submerged in cyclohexane. Next 0.35 mL of trichlorooctylsilane was added and the flask was sealed and removed from the glovebox. Under flowing nitrogen 0.25 mL of hydrochloric acid was added to the solution before it was sealed for 4 hours at room temperature. After 4 hours the substrates were removed from the silane solution and rinsed with toluene, isopropanol, and water before being stored.

Mixed ligand nanoparticle synthesis

Nanoparticles with constant dimension and variable ligand composition and ligand morphology were prepared as described previously.[37] The final nanoparticles have ligand coronas composed of DDT and 1H, 1H, 2H, 2H-Perfluoro-1-octanethiol (PFOT) ligand. The custom PFOT ligand was synthesized as described previously.[37]

Ex situ sol preparation

A stock solution of hydrophilic sol was prepared by adding 2.5 mL of TTIP to 0.6 mL of concentrated hydrochloric acid in an 8 mL glass scintillation vial stirring at 600 rpm. Upon addition of the TTIP an exothermic reaction produced a sol solution with a light-yellow color. The solution was stirred for 10 minutes prior to 1 mL of anhydrous THF being added to the vial.

Polymer and nanoparticle film casting

      A stock solution with a concentration of 0.5 g of homopolymer per 1 mL of TFT was made. An aliquot of the homopolymer solution was then added to a 1-dram glass vial. Next a stock solution of ML-NPs with a concentration of 5.77 mg per 1 mL of TFT was made and an aliquot was added to the homopolymer solution. The solvent was then removed from the vial through evaporation. Once the homopolymer and ML-NP mixture were dry, 1.2 mL of TFT was added to produce the desired mixture at the desired concentration. The mixture was sonicated for 15 minutes to ensure homogeneous dispersion. Thin films were prepared by spin coating onto the substrates with a hydrophobic surface treatment at a rate of 1000 rpm for 30 seconds under constant dry air flow producing a film ~50 nm thick. The spin coating was carried out using a home-built spin coater[39] with the tupperware being cleaned between each film being cast. Films were coated with a range of nanoparticle loadings based upon the target volume percent of nanoparticles using equation 1 below.

$$Vol.\% = \frac{\left(\frac{M_{NP}\, g}{\rho_{NP}\, \frac{g}{mL}}\right)}{\left(\frac{M_{polymer}\, g}{\rho_{polymer}\, \frac{g}{mL}}\right)} * 100\%$$

A similar procedure was used for casting of the PS-*b*-PFOA with the ML-NPs. Films were cast with a 0.52 ML-NP volume loading percent. An example composite film was produced by combining 32 mg of the PS-PFOA with 0.52 mg of 25F ML-NPs was spun cast onto a hydrophobic silicon substrate at 2000 rpm for ten seconds. Film morphology and ML-NP coassembly were analyzed using SAXS and TEM (Figure 3.5 – 3.15). Bulk films of the PEO-b-PS-b-PFOA were cast using THF into a teflon dish with a 1.5-inch diameter and a depth of 1.5 inches at 55˚C.

QCM measurements of film thickness

A custom made QCM apparatus was used to measure the mass of spin coated films on analogous quartz substrates prepared using the same hydrophobic surface treatment. The QCM apparatus, temperature equilibration, and flowing inert gas are described in detail elsewhere.[37]

Small angle X-ray scattering (SAXS) measurements

X-ray experiments were conducted using a SAXSLab Ganesha at the South Carolina SAXS Collaborative. A Xenocs GeniX3D microfocus source was used with a Cu target to generate a monochromic beam with a 0.154 nm wavelength. The instrument was calibrated using National Institute of Standards and Technology (NIST) reference material 640c silicon powder with the peak position at $2\theta = 28.44°$ where 2θ is the total scattering angle. A Pilatus 300 K detector (Dectris) was used to collect the two-dimensional (2D) scattering patterns. All SAXS data were acquired with an X-ray flux of ~21.4 and 1.7M photons per second incident upon the sample and a sample-to-detector distance of 452.1 mm and 1502.1mm, respectively. Transmission SAXS was measured normal to sample substrates to observe the purely in-plane morphology.

Molecular characterization

All proton nuclear magnetic resonance (^{1}H NMR) spectra were recorded on Bruker Avance III HD 400. All NMR samples were prepared in chloroform-D. Molecular weight (Mn) and molar mass dispersity (Đ) were determined using a Waters gel permeation chromatography (GPC) instrument equipped with a 515 HPLC pump, a 2410 refractive index detector, and three styragel columns (HR1, HR3, and HR4 in the effective molecular weight range of 0.1–5, 0.5–30, and 5–600 kg mol1 respectively).

THF was used as the eluent at 30˚ C at a flow rate of 1 mL per minute. The GPC was calibrated with PS standards (2570, 1090, 579, 246, 130, 67.5, 34.8, 18.1, 10.4, 3.4, 1.6 kg mol^{-1}) obtained from Polymer Laboratories.

Transmission electron microscopy (TEM) imaging

Thins films were isolated from the silicon substrates using a "lift-off" method. Silicon substrates were immersed into a hydrofluoric acid bath consisting of 2 parts deionized water and 1 part 51 wt.% hydrofluoric acid in water. Films were collected from the surface of the etching solution and deposited onto 300 mesh copper grids and were placed into a fume hood to dry. Once dry the films were stained using aqueous ruthenium tetroxide vapor. Grids were placed onto a silicon staining mat in a plastic petri dish and 2-4 drops of the fresh staining solution was added next to the grid, the petri dish was then covered for 15 minutes. Bulk films were sectioned using a Leica UC7/FC7 cyro-ultramicrotome to a thickness of 50 nm, the film sections were collected and placed onto copper grids. All films were imaged using a JEOL 1400 Plus TEM with an accelerating voltage of 120 keV.

3.4 Results and Discussion

Polymer Synthesis

To test the fluorophobic effect, and the ability to use it as a directing interaction in BCP coassembly, a fluorinated BCP must be prepared. There are a variety of fluorinated monomers commercially available ranging from fluorinated styrene derivatives to fluorinated methacrylates. For our system, a fluorinated acrylate that had the same chemical structure as the PFOT ligand was chosen to ensure the best possible match between the ML-FNPs and the BCP. This monomer is commercially available in small

quantities and is fairly expensive, so it was made in house. The monomer was made via a

Fischer esterification between acryloyl chloride and a perfluorinated alcohol as shown in

Figure 3.1. The monomer was successfully synthesized in a single step and purified using

a simple vacuum distillation. The chemical structure of the monomer was confirmed

using ^{1}H NMR (Figure 3.1). The reaction was easily scaled up to the multi-gram scale

without needed special glassware or different reaction conditions. The entire synthesis

can be carried out in under 48 hours. Once made, the monomer needed to be stored with

inhibitor to avoid auto polymerization in ambient conditions.
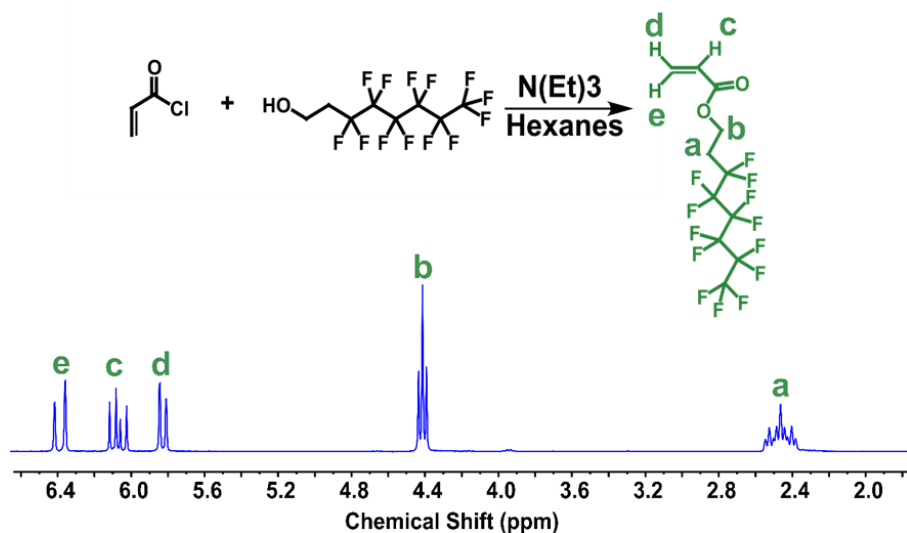

Figure 3.1 Synthetic scheme of the FOA monomer using a Fischer
Esterification (top) and NMR of the FOA monomer (bottom) with the
three acrylic protons between 5.6-6.4 ppm while the protons of the
perfluorinated ester tail are located at 2.4 and 4.4 ppm, respectively.

To synthesize both the H-PS and H-PFOA homopolymers Activator Regenerated

Electron Transfer Atom Transfer Radical Polymerization (ARGET-ATRP) was used.[40]

This method is highly advantageous as it utilizes a controlled radical which affords high

levels of control over the molecular weight and dispersity of the polymer chains.

94

ARGET-ATRP is also compatible with a wide array of monomer chemistries, including perfluorinated monomers, making it useful for this study. Since ARGET-ATRP is compatible with a wide array of monomers BCP synthesis is fairly facile and control over the chemical composition is afforded. Lastly, since a reducing agent is used to regenerate the activator, the amount of copper needed for the polymerization process is minimal. This makes the purification process much simpler and reduces the cost of each polymerization. The synthetic scheme for the H-PFOA is shown in Figure 3.2. The initiator, 2-bromopropionoate, was chosen as it has been shown to be a favorable initiator for acrylate monomers as they are not as reactive. The ligand, Me$_6$TREN, was chosen as
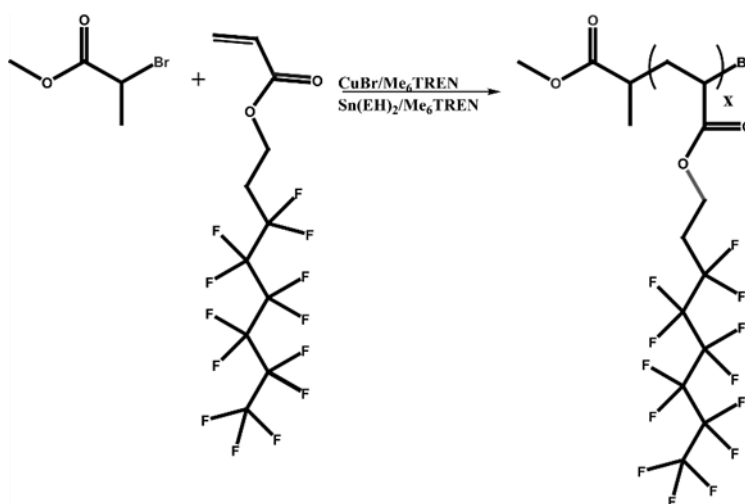

Figure 3.2 Polymerization scheme for the PFOA homopolymer using ARGET-ATRP.

it has been shown to increase the rate of ATRP reactions which would cut down on the polymerization time. Another important factor influencing the choice of Me$_6$TREN was that this polymerization needed to be carried out in solution. This is due to the insolubility of the copper, tin, and initiator in the fluorinated monomer. Solution

95

polymerizations have slower reaction times than bulk, so a faster ligand was chosen to offset this.

A non-fluorinated block is needed for the BCP coassembly experiments, so PS was chosen. PS has been made using every controlled radical method and is heavily used in the literature. The synthetic scheme of PS *via* ARGET-ATRP is shown in Figure 3.3a. This polymerization was carried out in the bulk state, meaning no solvent was added, as the styrene monomer solvates the initiator, copper, and tin. Once the polymerization is complete cleaning of the crude H-PS is very easy. Since PS is a glassy polymer at room temperature, the glass transition (T_g) of styrene is 100˚C, it can be collected by precipitation into cold methanol. After excess monomer was removed the H-PS could be
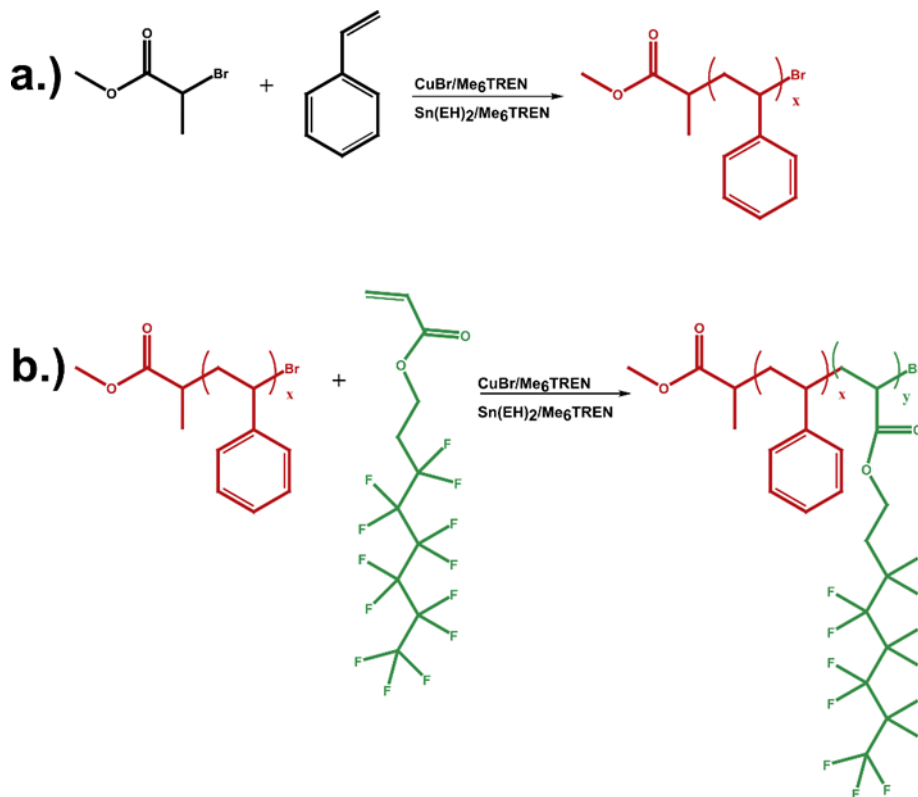

Figure 3.3 Polymerization scheme for the a.) PS macroinitiator and b.) PS-b-PFOA diblock copolymer synthesized using ARGET-ATRP.

used for the dispersion studies which will be discussed shortly. The purified H-PS was also used as a macroinitiator for the synthesis of the fluorinated BCP.

Another advantage of controlled radical methods is that they are considered living. A living method allows for subsequent polymerization off of the newly made polymer chain. For ARGET-ATRP, monomer addition occurs when the bromine is shuttled from the polymer chain to the copper activator. The newly active radical can add a monomer prior to the copper shuttling the bromine back creating a dormant radical. This process of shuttling the bromine, to activate and deactivate the radical, affords control. If the reaction is carefully stopped, being quenched without the presence of oxygen, the end of the newly grown polymer chain is capped with a bromine. By adding monomer and copper another block can be grown off of the chain end utilizing the bromine as the initiator. Thus, the process is deemed living and multiple blocks can be grown from the active chain end. ^{1}H NMR had shown the as-made H-PS chain was capped with a bromine, so it was used as a macroinitiator for the polymerization of the PS-*b*-PFOA BCP (Figure 3.3b).

The results of the polymerization of the H-PFOA, H-PS, and PS-b-PFOA are shown in Figure 3.4 and Table 3.1. ARGET-ATRP was successfully used to synthesize the three polymers as shown by NMR analysis (Figure 3.4a-c). The H-PFOA has four proton signals that can be used to ascertain the molar mass of the polymer chain (M_n). The alkyl protons in the carbon backbone are located between 1-2 ppm, respectively. The -CH_2 unit directly connected to the perfluorinated tail is shifted downfield to 2.5 ppm. The -CH_2 connected to the oxygen of the ester is shifted furthest downfield to 4.25 ppm. The H-PS NMR (Figure 3.4b) has alkyl backbone peaks, in similar locations as the H-

97

PFOA, from 1-2 ppm, respectively. The characteristic aromatic protons are located between 6-7.5 ppm, respectively. The presence of these peaks confirms growth of the H-PS polymer. Finally, the PS-*b*-PFOA diblock spectrum is shown in Figure 3.4c. The presence of the aromatic protons near 6-7.5 ppm confirm the presence of the PS block. The characteristic peaks of the H-PFOA polymer are found at 2.5 and 4.25 ppm, respectively, suggesting growth of the PFOA block off of the PS macroinitiator. GPC
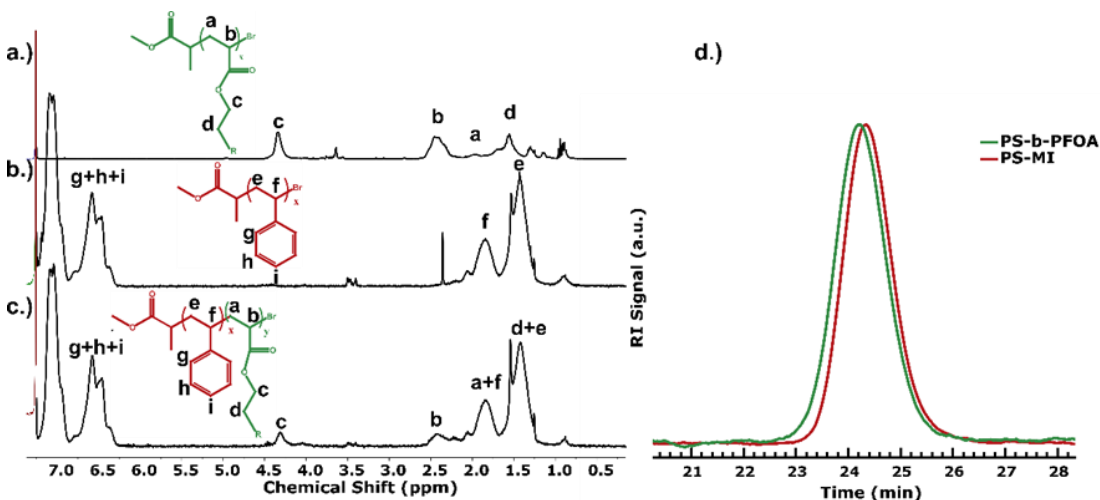

Figure 3.4 NMR spectra for the a.) PFOA homopolymer, b.) PS homopolymer and macroinitiator, c.) PS-*b*-PFOA diblock copolymer where R = C_6F_{13}, and d.) GPC trace for the PS macroinitiator and PS-*b*-PFOA diblock copolymer.

analysis confirmed growth of the PFOA block (Figure 3.4c). The PS-b-PFOA (green) has a visible shift to a faster retention time from the PS macroinitiator (red). This shift signals growth of the PFOA domain from the macroinitiator. The GPC curves have a monomodal distribution suggesting little to no termination has occurred. The results of the NMR and GPC analysis are shown in Table 3.1. The H-PS had an M_n = 12,144 g/mol and a molar mass dispersity (Đ) = 1.16 showing the polymerization was controlled. NMR analysis of the H-PFOA shows an M_n = 4,598 g/mol showing growth of the polymer chain. It is important to note that GPC measurement of the H-PFOA Đ was unattainable as the

98

perfluorinated homopolymer is insoluble in THF which is the solvent system for the GPC used. NMR of the PS-*b*-PFOA BCP shows that a PFOA block of $M_n = 5,434$ g/mol was grown off of the PS macroinitiator that had an $M_n = 12,144$ g/mol bringing the total $M_n = 17, 578$ g/mol, respectively. The weight fraction of the PFOA block was 31% making it the minority block. GPC analysis shows a Đ = 1.15 suggesting controlled growth of the PFOA off of the PS macroinitiator.

Table 3.1 Polymer Characterization.

Sample	$M_{n\ PEO}$ (g/mol)[a]	$M_{n\ PS}$ (g/mol)[a]	$M_{n\ PFOA}$ (g/mol)[a]	$M_{n\ Total}$ (g/mol)[a]	Đ[b]
PEO-Br	5000	-	-	5000	1.06
PS-MI	-	12,144	-	12,144	1.16
PFOA	-	-	4,598	4,598	1.30
PS-*b*-PFOA	-	12,144	5,434	17,578	1.15
PEO-*b*-PS	5000	22,704	-	27,704	1.34
PEO-*b*-PS-*b*-PFOA	5000	22,704	8,117	35,821	1.28

[a] obtained from ^{1}H NMR analysis, [b] obtained from GPC analysis.

Dispersion experiments of the ML-FNPs

The interactions used to coassemble inorganic materials with block copolymers must be selective to one phase of the BCP. This enables high levels of control over the placement of the inorganic. If high loadings are to be achieved, the interaction must favor mixing of the inorganic in the BCP system over phase separation. Therefore, the energy of the inorganic mixing with the BCP must be lower than de-mixing. Hydrogen bonding between the donor and acceptor lower the energy of the system ultimately leading to mixing. For the fluorophobic effect to promote mixing, the dispersion experiments should show the NPs being expelled, or aggregating, in the H-PS environment due to the unfavorable interactions. While the NP and the H-PFOA should show mixing,

represented by dispersion. This would suggest a favorable match between the ligand shell of the ML-FNPs and BCP promoting the use of the fluorophobic effect.

To probe the viability of the fluorophobic effect, dispersion experiments of the ML-FNPs in the H-PS at a constant loading percentage were performed. In a dilute NP solution, a form factor peak would be observed if dispersion was occurring. If NP-NP correlation is observed at such a low volume percentage aggregation is occurring as the NPs are being force together. If the NPs aggregate at low volume loading percentages, it would suggest incompatibility with lipophilic systems. The ML-FNPs with varying fluorine content were dispersed in the H-PS at a loading of 0.05 vol.%. Thin films of each sample were spun onto glass treated with a hydrophobic capping layer to improve the quality of the thin film. The dispersion state was determined by the presence of a structure factor peak at 2 nm^{-1} that is consistent with NP-NP correlations in SAXS. The results of these dispersion studies are shown in Figures 3.5-14, respectively.

Similar dispersion experiments were conducted with the ML-FNPs in the H-PFOA over a range of volume loading percentages. The ML-FNPs with varying PFOT content were dispersed at loading percentages of 0.05, 0.22, 0.37, 0.52, and 0.74 vol.%, respectively. Thin films were spun onto the same glass substrates treated with the hydrophobic capping layer to improve thin film quality. The dispersion state was then analyzed using SAXS measurements. The presence of a structure factor peak at 2 nm^{-1} or a form factor peak was used to characterize the dispersion state. If a form factor peak is observed, it suggests the H-PFOA is acting as a good solvent for the ML-FNPs. This indicates a favorable interaction between the PFOTand the H-PFOA polymer. The results of the dispersion experiments are found in Figures 3.5-14, respectively.

The first ML-FNPs tested were the 0F-NPs. The ligand shell is completely composed of the hydrophobic DDT ligand. This sample would act as a control for the dispersion studies as no PFOT is present in the ligand shell. These exact NPs have also been used in previous studies testing the effectiveness of hydrophobic interactions for coassembly. It has been documented that the DDT ligated NPs do not disperse in BCP systems, phase separating at a loading percentage higher than the 0.05 vol.%. The dispersion results of the 0-FNPs in the H-PS and H-PFOA are shown in Figure 3.5. The 0F-NPs do not show a structure factor peak in the H-PS suggesting that aggregation is not occurring. At this low concentration aggregation is not expected between the two hydrophobic materials. Dispersion of the 0F-NPs in the H-PFOA was extremely difficult as the two materials are highly immiscible. Even after 30 minutes of sonication the red layer of 0F-NPs was observed phase separating from the H-PFOA layer in trifluorotoluene (TFT). Heating of the solution was avoided as the gold NPs can ripen and grow if exposed to elevated temperatures. Films of the solution were spun onto the glass substrate although dispersion is not expected. No structure factor peak was observed with the 0F-NPs at the lowest vol.%. This is most likely a combination of the macrophase separation from the H-PFOA and the small quantities of NPs added causing most to be expelled from the substrate as it was drying. Multiple areas of the thin film were measured all yielding the same result. Repeat experiments were attempted yielding similar results. Even when the solvent was increased to further dilute the sample macrophase separation of the NPs from the H-PFOA was observed. This behavior is attributed to the large difference in chemistry between the alkyl ligand of the NP and the perfluorinated tail of the acrylate.

As the loading of the 0F-NPs was increased a slope change was observed in the low q-region as well as a peak near 0.8 nm^{-1}. These results suggest large scale aggregation in the thin films. The peak at low q may be correlations of NP clusters on the surface of the thin film as the NPs and H-PFOA are immiscible. This is expected as the 0F-NPs and the H-PFOA have a large chemical dissimilarity and the mixture exhibited macrophase separation.

Dispersion experiments of the 25F-NPs show the fluorophobic effect begin to occur (Figure 3.6). A structure factor peak near 2 nm^{-1} is observed for the 25F-NPs in the
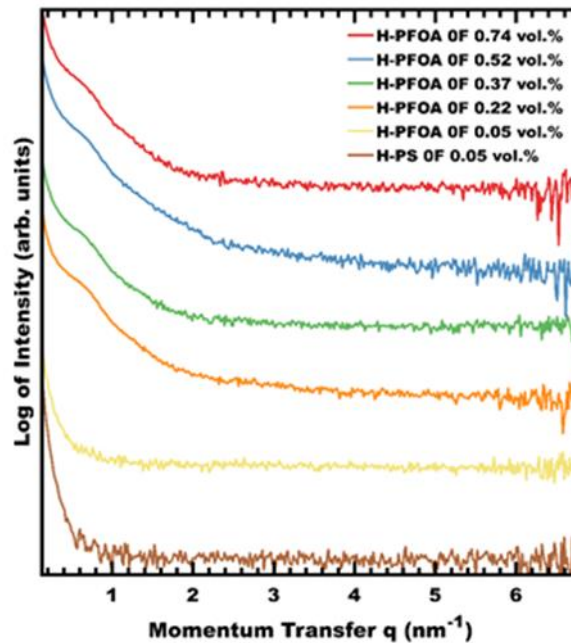

Figure 3.5 Dispersion experiments of the 0F-NPs in the H-PS and H-PFOA.

H-PS consistent with aggregation. The presence of aggregation with just 25% PFOT in the ligand shell suggests that even low amounts of fluorine are sufficient to generate
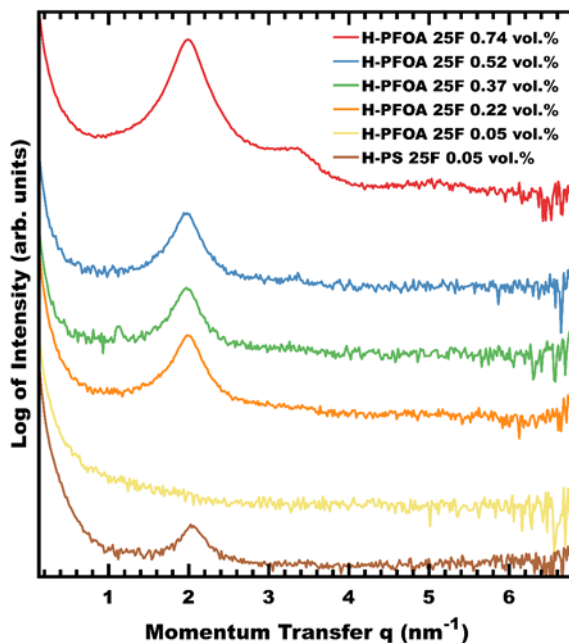
Figure 3.6 Dispersion experiments of the 25F-NPs in
the H-PS and H-PFOA

unfavorable interactions. The unfavorable interactions with the lipophilic H-PS lead to

aggregation to reduce the number of interactions. Thins films of the 25F-NPs and H-

PFOA do not show structure factor occurring until the loading percentage exceeds 0.05

vol.% suggestive of dispersion. Once the NP loading reaches 0.22 vol.%, a very intense

structure factor peak is observed. The results from dispersion of the 25F-NPs suggest that

low fluorine content in the ligand shell induces immiscibility with the chemically

dissimilar H-PS. However, the aggregation in the H-PFOA at low loadings is indicative

of incompatibility with the fluorinated polymer chains. This is contradictory to the small

molecules screened with the QCM, as these particles had increased interactions with all

of the molecule vapors. Thus, the composition appears to play a more substantial role

than the ligand shell morphology.

103

As the fluorine content is increased to 31%, the ML-FNPs are still incompatible with the H-PFOA at higher loadings (Figure 3.7). Aggregation of the 31F-NPs is observed in the H-PS thin film as a prominent structure factor peak is observed at 2 nm^{-1}. These results again show that the addition of more PFOT increases the chemical dissimilarity with the H-PS leading to de-mixing and aggregation. Dispersion of the 31F-NPs in the H-PFOA also shows incompatibility as the NPs aggregate at low loadings. A
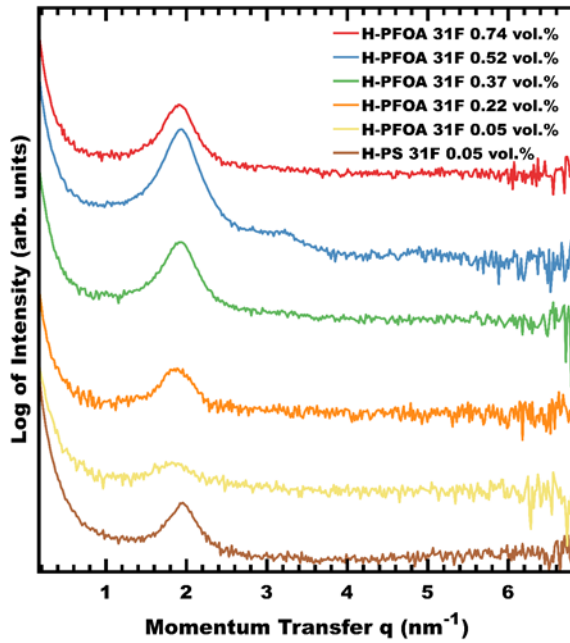

Figure 3.7 Dispersion experiments of the 31F-NPs in the H-PS and H-PFOA.

fairly weak scattering feature is observed at a loading of 0.05 vol.%. Although weak, it suggests the 31-FNPs are aggregating in the H-PFOA. An increase in the NP loading coincides with the structure factor peak becoming more prominent. These results strengthen the theory of ML-FNPs with low PFOT content being incompatible with the perfluorinated H-PFOA. One interesting observation is that the 31F-NPs are aggregating at a lower vol.% than the 25F-NPs. This may be due to the structure of the ligand shell. In

104

the QCM studies, discussed in chapter 2 of this thesis, the 31F-NPs are the transition

point from the patchy morphology to the stripe-like domains (Figure 2.15). Thus, the

31F-NPs had a large and significant decrease in molecule uptake when compared to the

20F-NP films as the PFOT was shielded from the molecule vapor. This may explain the

aggregation in the H-PFOA at a lower vol.% than the 25F-NPs as the fluorinated thiol

may be shielded from the H-PFOA. This would make the ligand shell appear

hydrophobic leading to behavior akin to the 0F-NPs.
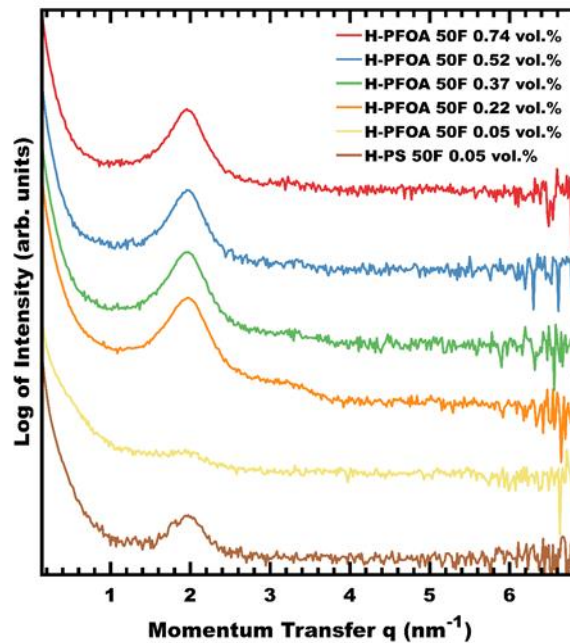

Figure 3.8 Dispersion experiments of the 50F-NPs in
the H-PS and H-PFOA.

As the amount of fluorine in the ligand shell is further increased to 50%, the ML-

FNPs exhibit incompatibility with the H-PFOA (Figure 3.8). The 50F-NPs are

incompatible with the H-PS as aggregation is observed at low loading percentages. This

continues the trend of PFOT addition inducing the fluorophobic effect. In the H-PFOA,

there is no structure factor peak present at a loading of 0.05 vol.%. As the loading is

105

increased to 0.22 vol.% a prominent structure factor peak, with signs of a secondary

shoulder at 3 nm^{-1}, is observed. The secondary peak is suggestive of the 50F-NPs packing

within the clusters being formed. The structure factor peak remains as the loading of the

50F-NPs is increased. Curiously, the intensity of the structure factor peak remains

consistent. These results show that the ligand shell needs a majority of the fluorinated

thiol for good chemical compatibility as 50% is not sufficient.

As the percent fluorination in the ligand shell exceeds 50%, the ML-FNPs are still

immiscible in the H-PFOA (Figure 3.9). Aggregation is observed in the H-PS as the 52F-
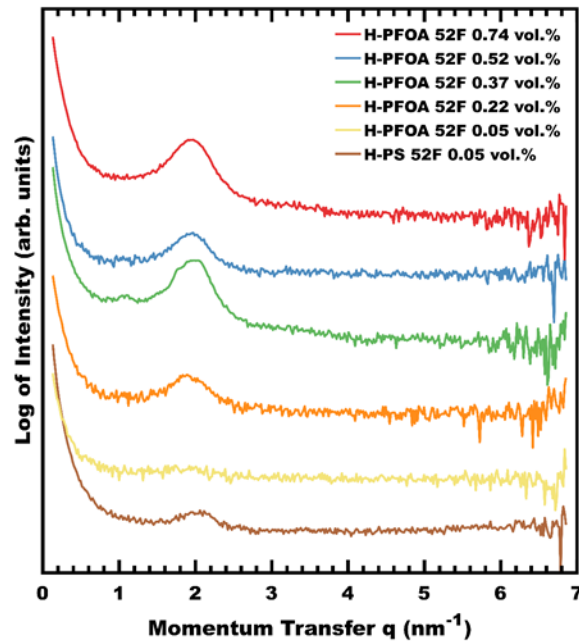

Figure 3.9 Dispersion experiments of the 52F-NPs in
the H-PS and H-PFOA.

NPs are a majority fluorinated, making them immiscible with the lipophilic H-PS

environment. At 0.05 vol.%, the 52F-NPs are dispersed in the H-PFOA as a structure

factor peak is not present. As the loading is increased to 0.22 vol.%, a structure factor

peak is observable at 2 nm^{-1} indicating aggregation. The structure factor peak is visible in

all of the films with loadings of 0.22 vol.% and above. Although the ligand shell is now a majority, the small increase was not enough to enhance the chemical compatibility. Based on the dispersion results observed the fluorophobic effect is very sensitive to DDT content. To improve miscibility in the H-PFOA significant increases in the amount of PFOT are needed.

With a definitive majority of PFOT in the ligand shell a decrease in the structure factor peak is observed (Figure 3.10). As expected, the 65F-NPs are insoluble in the H-PS domain which is evident from the structure factor peak located at 2 nm^{-1}. The intensity
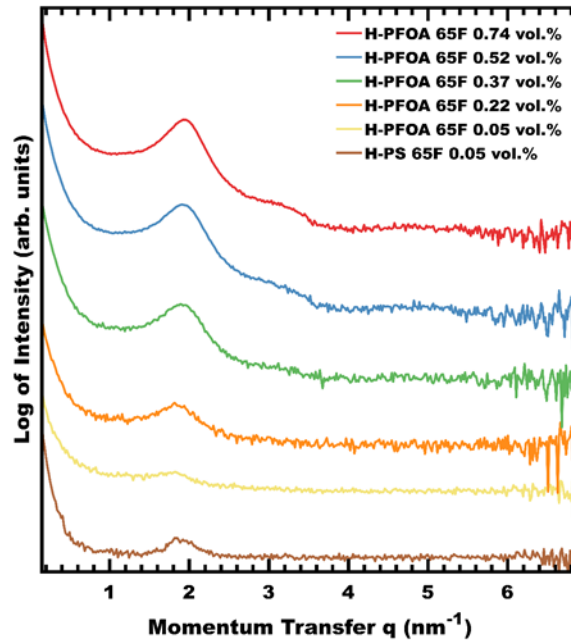

Figure 3.10 Dispersion experiments of the 65F-NPs
in the H-PS and H-PFOA.

of the peak is not as strong as past samples but is still visible. In the H-PFOA the 65F-NPs are able to be dispersed with very low loadings. Similar to the previous samples, there is a structure factor peak present as the loading reaches 0.22 vol.%. However, a decrease in the intensity of the structure factor peak has coincided with an increase of

107

PFOT in the ligand shell. This is evident with the structure factor peak for the 0.22% which is less intense and more-broad than prior ML-FNPs, respectively. This is a sign that the chemical compatibility is increasing.

Dispersion experiments with the 75F-NPs continue the subtle trend of greater compatibility with the H-PFOA (Figure 3.11). The 75F-NPs have a patchy morphology in the ligand shell and show significant enhancements in their interactions with small molecules. This does not translate to greater enhancement with the H-PS, as the 75F-NPs aggregate due to the majority PFOT in the ligand shell. In the H-PFOA, there is no sign
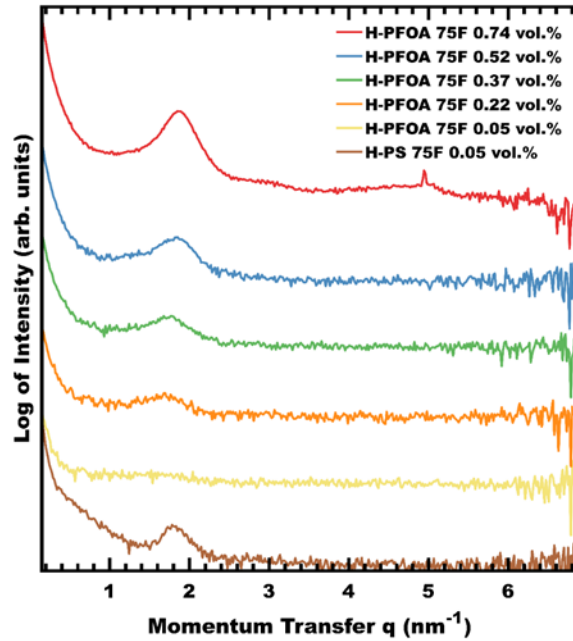

Figure 3.11 Dispersion experiments of the 75F-NPs
in the H-PS and H-PFOA.

of aggregation at the lowest loading of the ML-FNPs. As the vol.% is increased to 0.22, there is a very broad peak observed near 1.9 nm^{-1}. This structure factor peak is barely visible, signaling better compatibility as the ligand shell has large domains of the PFOT.

Even at 0.37 and 0.52 vol.% loading the structure factor peak has diminished and broadened compared to ML-FNPs with lower PFOT content.

As the PFOT domains continue to grow, the ML-FNPs appear to have greater dispersion in the H-PFOA matrix (Figure 3.12). Two intense peaks are observed for 85F-NPs in the H-PS signaling aggregation. The incompatibility between the ML-FNPs and
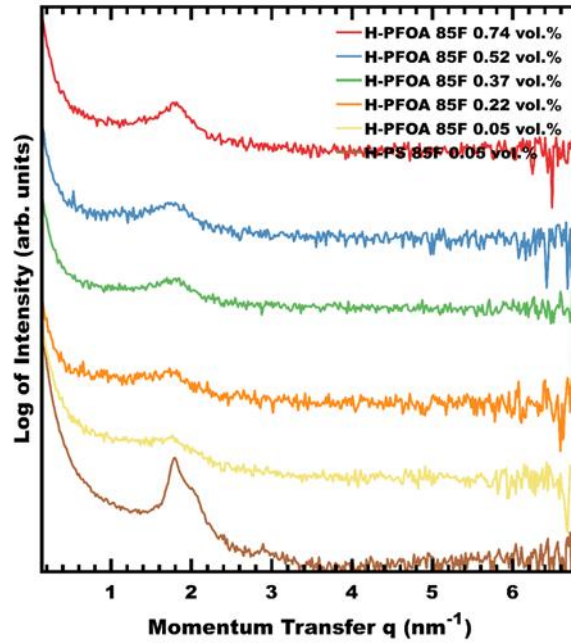

Figure 3.12 Dispersion experiments of the 85F-NPs
in the H-PS and H-PFOA.

the H-PS is continually increasing as the PFOT percentage is increased. Dispersion of the 85F-NPs in the H-PFOA shows greater chemical compatibility. No structure factor peak is observed in the 0.05 and 0.22 vol.% loading samples. Even at 0.37 and 0.52 vol.% loading the structure factor peak has decreased in intensity and is barely observed from the baseline, respectively. With a large majority PFOT the ML-FNPs are becoming a better match to the perfluorinated PFOT.

With more than 90% PFOT in the ligand shell, the loading has exceeded 0.37 vol.% before aggregation occurs (Figure 3.13). Continuing the trend, the 93F-NPs are chemically incompatible with the H-PS as aggregation is occurring. The structure factor
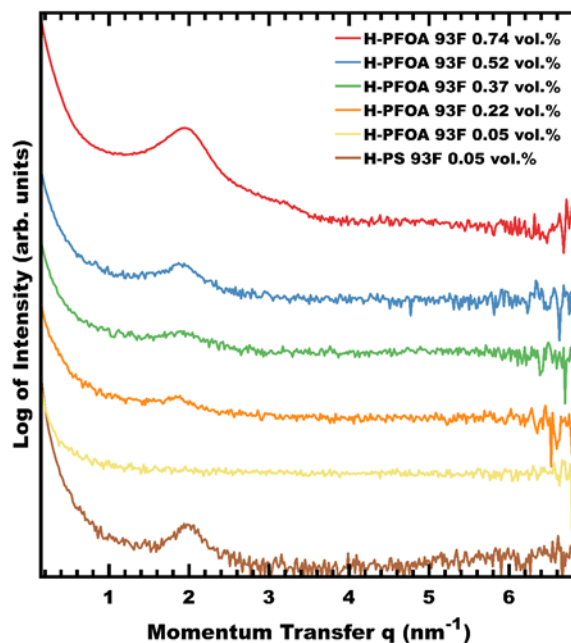

Figure 3.13 Dispersion experiments of the 93F-NPs in the H-PS and H-PFOA.

peak at 2 nm^{-1} is absent from the dispersions with H-PFOA until a loading of 0.52 vol.% is reached. This again points to enhanced interactions with the PFOA matrix, as the structure factor peak is no longer present until the vol.% exceeds 0.50. Remarkably, aggregation is still observed with as little as 7% DDT in the ligand shell.

The last two plots will be discussed together as the ligand shell for the 98F and 100F-NPs is perfluorinated, and both show high compatibility with the H-PFOA (Figure 3.14 and 3.15). Both the 98F and 100F-NPs aggregate in the H-PS matrix. This shows that any amount of PFOT in the ligand shell of the ML-FNPs induces aggregation in the H-PS. As a structure factor peak was observed with the 25F-NPs and persisted through
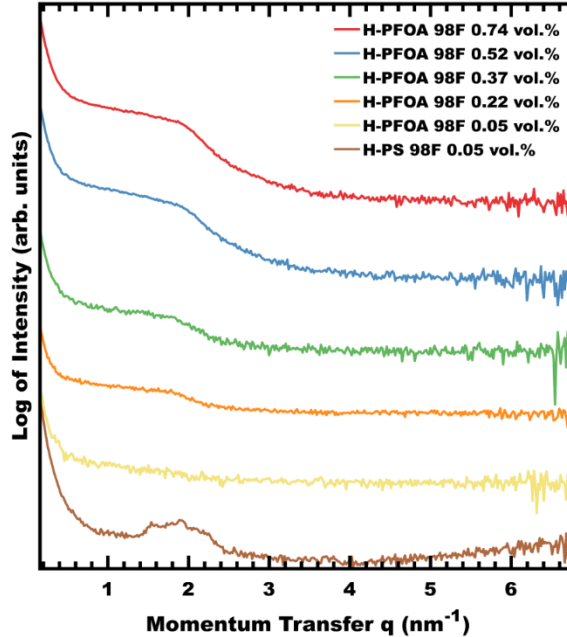
110

Figure 3.14 Dispersion experiments of the 98F-NPs
in the H-PS and H-PFOA.

the 100F-NP sample. This suggests that the fluorophobic effect is directive, as the ML-

FNPs are incompatible with the lipophilic PS and should push the NPs from the PS

domain of the BCP during coassembly. In the H-PFOA matrix, the perfluorinated ML-

FNPs exhibit high compatibility as the scattering curves show a form factor for all of the

loading percentages. The form factor is scattering from individual NPs in solution, this

feature is only observed when NPs do not have correlations with other NPs. Thus,

sufficient distance must be between the individual NPs. The presence of a form factor

peak suggests that the H-PFOA is acting as a good solvent for the 98F and 100F-NPs.

Both show form factor curves up to 0.74 vol.%, respectively.

By combining the results of the individual dispersion experiments a map can be

built to show the overall trend in dispersion as a function of PFOT in the ligand shell

111

(Figure 3.16). The dispersion map includes the ML-FNPs with the H-PFOA at all of the loading percentages analyzed. The blue circles represent ML-FNP dispersion and the red triangles represent aggregation. The shaded blue region of the plot is a guide for the eyes to help elucidate the observed trends. Dispersion in the H-PFOA appears to be influenced
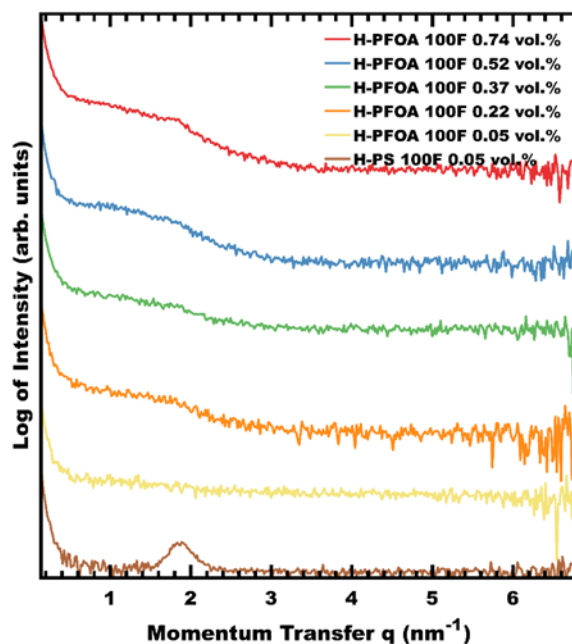

Figure 3.15 Dispersion experiments of the 100F-NPs
in the H-PS and H-PFOA.

by the chemical composition of the ligand shell alone with morphology playing an insignificant role. The 25F and the 75F-NPs were found to have enhanced uptake with all of the molecular environments screened using the QCM (Figure 2.17 and 2.18) and had a patchy ligand shell as determined by ^{19}F NMR (Figure 2.15). The enhanced interactions with small molecules did not translate to enhanced interactions with the large macromolecules of H-PFOA. As discussed in chapter 2, the size of the molecule plays an important role in determining whether it will interact with the mixed ligand shell or be excluded due to unfavorable entropy.[36] The polymer chains are much larger, and the

fluorinated tail of the acrylate block is rigid which would restrict access to interdigitate with the ligand shell. These two factors may explain why there was not an enhancement in the dispersion behavior. Only one sample, the 31F-NPs, appears to have significant
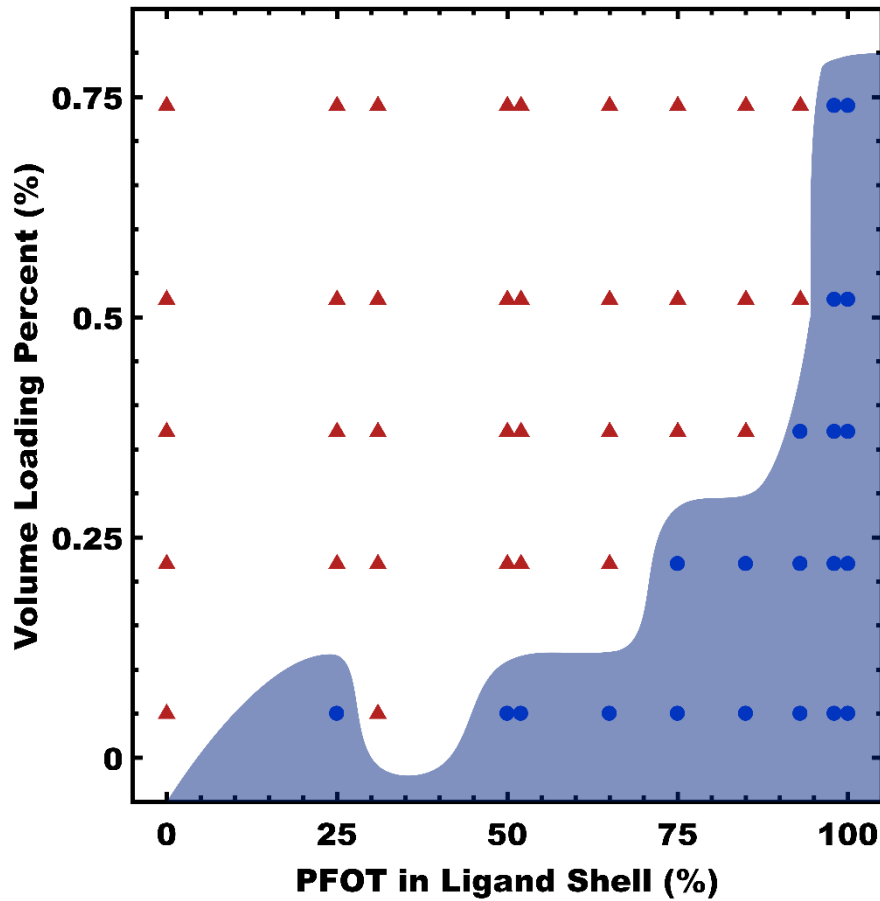
Figure 3.16 Plot of the ML-FNPs volume loading percentage vs. PFOT in the ligand shell. The blue circles indicate dispersion in H-PFOA, and the red triangles represent aggregation. Blue line is a guide for the eyes only.

morphology effects. The 31F-NP were predicted to be stripe-like by ^{19}F NMR (Figure 2.15) and QCM revealed a significant decrease in the uptake behavior. In fact, the uptake was similar to the fully hydrophobic 0F-NPs. This may explain why the 31F-NPs

www.manaraa.com

aggregate in the H-PFOA at 0.05 vol.% while the 25F-NPs disperse as the PFOT ligands may be shielded from interaction with the H-PFOA.

The favorable match of the PFOT ligand and the H-PFOA is apparent with the rapid increase in dispersion as shown by Figure 3.16. The loading of the ML-FNPs remained below 0.22 vol.% until the ligand shell was composed of 75% PFOT. The steady increase in the loading achieved prior to the appearance of aggregation coincides with an increase in the PFOT% in the ligand shell. Remarkably, even 7% DDT in the ligand shell is enough to drive aggregation at higher loading percentages. This highlights the mismatch of the alkyl thiol with the fluorinated homopolymer. Only when the ligand shell was completely fluorinated did the ML-FNPs shown true dispersion in the H-PFOA with the appearance of the form factor peak. The results suggest that the fluorophobic effect it very effective in generating a mismatch between the ML-FNPs and the H-PS but is very selective as only the perfluorinated ML-FNPs had a match with the H-PFOA.

Coassembly experiments of the ML-FNPs with the PS-*b*-PFOA diblock copolymer

Thin films of the PS-*b*-PFOA and ML-FNPs were spun to examine the coassembly through the fluorophobic effect. The PS-*b*-PFOA and ML-FNP were combined with TFT and agitated using an ultrasonicator bath to generate a homogenous solution prior to spin coating onto glass and silicon substrates. Early thin films showed signs of dewetting on both substrates with most of the solution being expelled during the spin coating process. This was due to the unfavorable interaction of the non-polar block copolymer solution with the polar surface of both the glass and silicon substrates. To remedy this issue a non-polar surface coating was applied to the substrates allowing for a more homogeneous thin film to be produced without dewetting. The thickness of the thin

114

films was optimized by spin coating the solution onto a QCM crystal which can be used to calculate and approximate film thickness. Using the QCM based method a film with an approximate thickness of 50 nm was produced from a 1.7 wt.% polymer solution that was spun onto the substrate at 1000 rpm. An optimal thickness of 50 nm was chosen as film sections should be near 50 nm for TEM analysis. All of the films were sonicated for 15 minutes prior to casting to ensure homogeneity. This time should not damage the ML-FNPs as they undergo six cleaning cycles with 20 minutes of sonication in each cycle which had not cause aggregation or particle growth. The BCP should also be free of damage as a recent study had shown no chain scission with 5 hours of consecutive sonication.[41]

Once the spin coating conditions were determined a series of thin films of the PS-*b*-PFOA diblock copolymer and the ML-FNPs with a 0.50 vol.% loading were spun onto glass and silicon substrates. The thin films spun onto glass were analyzed using SAXS (Figure 3.17). A single loading percentage was used so that a direct comparison for all of the ML-FNPs could be made. Here, the coassembly ability of the ML-FNPs as a function of ligand shell composition would be evaluated. Similar to the homopolymer dispersion experiments the appearance of a structure factor peak near 2 nm^{-1} would indicate NP-NP correlations and aggregation since the loading is still in the regime of a dilute solution. The presence of a polymer separation peak is also important as the coassembly of the ML-FNPs should not disrupt BCP self-assembly. If the primary scattering feature of the BCP is not present it would suggest that the ML-FNPs are disrupting the polymer ordering which indicates failure in coassembly.

The coassembled thin film containing the 0F-NPs show the disappearance of the primary scattering feature at 23.5 nm consistent with the self-assembly of the PS-b-PFOA diblock copolymer. It is important to note that there is not a feature at 2 nm^{-1} consistent with aggregation. However, the loss of the BCP peak suggests the 0F-NPs are incompatible with the BCP system and failure of coassembly. For all of the ML-FNPs with PFOT in the ligand shell a scattering feature near 24 nm is observed. The
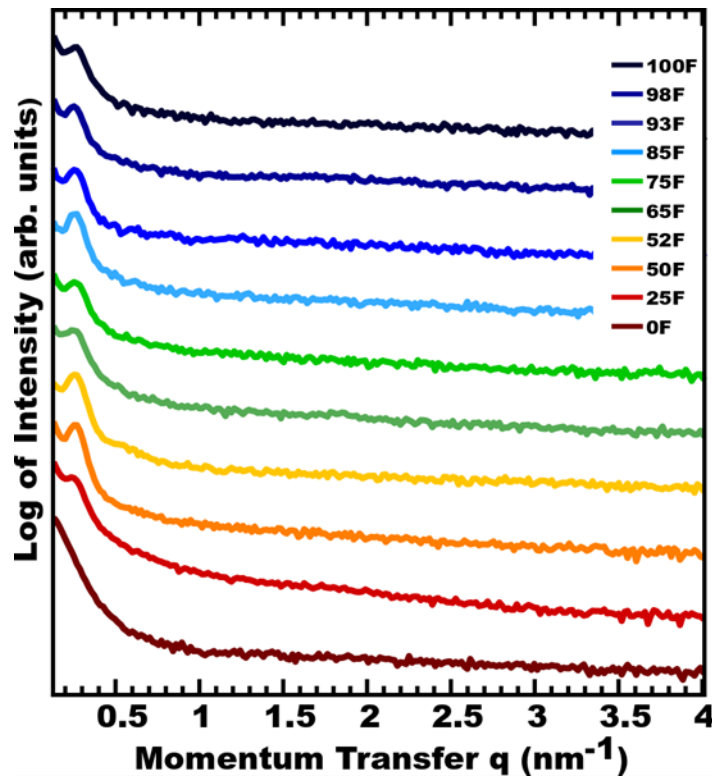

Figure 3.17 SAXS data of the PS-*b*-PFOA diblock copolymer and the ML-FNPs thin films. A primary peak with a 24 nm d-spacing is observed for all films other than the 0F FNPs.

preservation of the primary scattering feature and slight shift to a higher d-spacing suggest incorporation into the block copolymer system. There is also no structure factor peak at 2 nm^{-1} suggesting that dispersion in the BCP is occurring. These results suggest that even small amounts of fluorine in the ligand shell are sufficient to induce

116

compatibility with the BCP. Here, ML-FNPs with just 25% fluorine appear to coassemble with the BCP instead of aggregating. It is hypothesized that the strong repulsion from the PS block is forcing the ML-FNPs to segregate into the PFOA block during the BCP self-assembly and then the NPs are frozen in place once the PS becomes glassy. This can be explained through the behavior observed in the homopolymer films.

In the simpler ML-FNP homopolymer studies the sole interaction was between the NP and the polymer matrix. In the H-PS any particle containing PFOT aggregated at 0.05 volume loading percent indicating unfavorable interactions with the H-PS. This suggests the ML-FNPs are being pushed from the H-PS through the fluorophobic effect. In the H-PFOA only NPs with high PFOT content had dispersion at high volume loading percentages. Even the 75F-NPs aggregated at 0.22 volume loading percent, respectively. This suggests that there is a chemical match between the ligand shell and the PFOA when the ligand shell is highly perfluorinated. The final and very important observation is that at the lowest volume loading percent, 0.05, the ML-FNPs were more compatible with the H-PFOA than in the H-PS. In the BCP system there are three interactions occurring opposed to the single interaction probed in the homopolymer dispersion studies. Here, there is the interaction between the PS and PFOA block inducing self-assembly into phase separated domains. At the same time the ML-FNPs are interacting with the PS block and the PFOA block. As this is occurring the ML-FNPs are being pushed from the PS domain into the PFOA domain due to the slight preference due to the PFOT in the ligand shell. As the film rapidly dries the PS becomes glassy trapping the system. This could explain why ML-FNPs with minimal fluorine content appear to coassemble with

the BCP instead of aggregating. To confirm this hypothesis real space images were taken and will be discussed shortly.

The coassembly of the ML-FNPs with the PS-*b*-PFOA was evaluated using TEM analysis. For TEM, polymer films must be under 100 nm in thickness or the quality of the image is low as few electrons can penetrate through the entire film. Normally, polymer films are cast in bulk, collected, and sectioned into 50 nm thick slices. If this method was used the resulting sections would not be comparable to the series spun onto glass and analyzed using SAXS in Figure 3.17 as the kinetics of bulk casting and spin coating are vastly different. For an accurate comparison thin films needed to be spun onto a substrate under the same conditions and removed for TEM analysis. The films being produced using spin coating are estimated to be 50 nm using QCM analysis. Therefore, the thickness of the as-spun films should be within the acceptable thickness regime. To remove the films from the substrate a special "lift-off" technique needed to be implemented.[42] Thin films were prepared for TEM analysis by spin coating silicon wafers that had a 100 nm layer of silica on the surface. This allowed for the films to be lifted from the surface of the substrate as it was submerged into a concentrated hydrofluoric acid bath. The films collected were then stained using ruthenium tetroxide vapor which will stain the PS domain through interaction with the unsaturated aromatic rings.[43] Thus the PS domain will appear slightly darker than the PFOA domain providing contrast.

TEM imaging revealed a disorder structure for the phase separated PFOA domains with the size and shape of the domain showing large variation (Figure 3.18). During spin coating the solvent is quickly evaporated forcing the self-assembly process to rapidly occur. Since PS is the majority block it will become glassy trapping the PFOA

118

domains when the solvent is no longer present stopping the phase separation process. This could explain the disordered structure and negligible shift in the d-spacing observed in the SAXS experiments. Large aggregates of the 0F-NPs that were phase separated from both the PS and PFOA domains (Figure 3.18a). This is consistent with the behavior
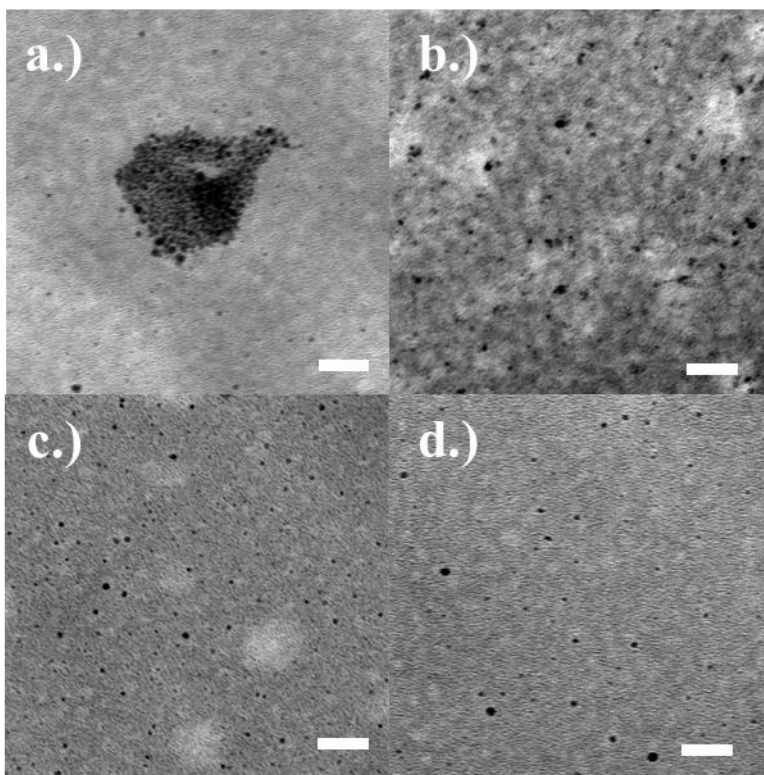

Figure 3.18 TEM images of the a.) 0F-NPs, b.) 25F-NPs, c.) 75F-NPs, and d.) 98F-NPs. The lighter domain is the PFOA and the darker domain is the PS matrix stained using ruthenium tetroxide. The gold NPs appear as the dark spheres. Scalebar is 50 nm.

of purely hydrophobic NPs with small alkyl ligands.[28] The BCP is still showing a phase separated structure suggesting that the 0F-NPs are being expelled from the film allowing the BCP to still order. The presence of the aggregates which are 75-150 nm in size could explain why the polymer phase separation peak is missing in Figure 3.17. The broad size distribution of the aggregates would lead to a broad sloping peak in low q which would

washout the BCP scattering features. The 25F-NPs are being incorporated in the BCP system and not phase separating (Figure 3.18b). However, the 25F-NPs are all aligning at the interface between the PS and PFOA domains. In all of the images taken the 25F-NPs are directly at the interface with a portion of the dark NPs being located in both domains. This points to a mismatch between the NPs and both polymer domains as they are being forced to the interfacial area. This can be explained as the small amount of PFOT in the ligand shell is not sufficient to assemble the NPs in the PFOA indicating a mismatch. At the same time the PFOT induces the fluorophobic effect expelling the NP from the PS domain. As the amount of PFOT is increased the NPs appear to successfully coassemble with PFOA domain of the BCP (Figure 3.18c and d). The 75F-NPs show all of the NPs assembling within the PFOA domain with no cross-loading into the PS. Some of the NPs are located near the interface but the entire particle is located in the PFOA domain unlike the 25F-NPs which sat directly on the interface. A large portion of the 75F-NPs are also found sitting in the center of the PFOA domain. This suggests that at higher PFOT percentages there is enough of a match between the ligand shell and the PFOA to successfully coassemble the NPs through the fluorophobic effect. At the same time the extensive PFOT content expels the 75F-NPs from the PS domain entirely due to the large dissimilarity in chemistry. Remarkably, this is done with small ligands less than 10 carbons in length. In hydrophobic systems large polymer grafted ligands were required to assemble the particles and loadings less than 0.5 volume percent are achieved.[27] The use of hydrogen bonding small molecules was also not needed for this approach to be successful.[28] Similar observations were found with the 98F-NPs as most of the NPs are found inside the PFOA domain.

120

Multimodal Coassembly with the PEO-b-PS-b-PFOA triblock terpolymer

The BCP coassembly results show that the ML-FNPs with a majority PFOT in the ligand shell successfully assemble into the PFOA domain. Thus, the ligand shell of the ML-FNPs needs to be highly fluorinated for the correct match to occur. All of the BCP and ML-FNPs were cast from a highly hydrophobic solvent system, trifluorotoluene (TFT), as no hydrophilic materials were present. For multimodal coassembly to work a more hydrophilic solvent system than TFT will need to be employed as materials like
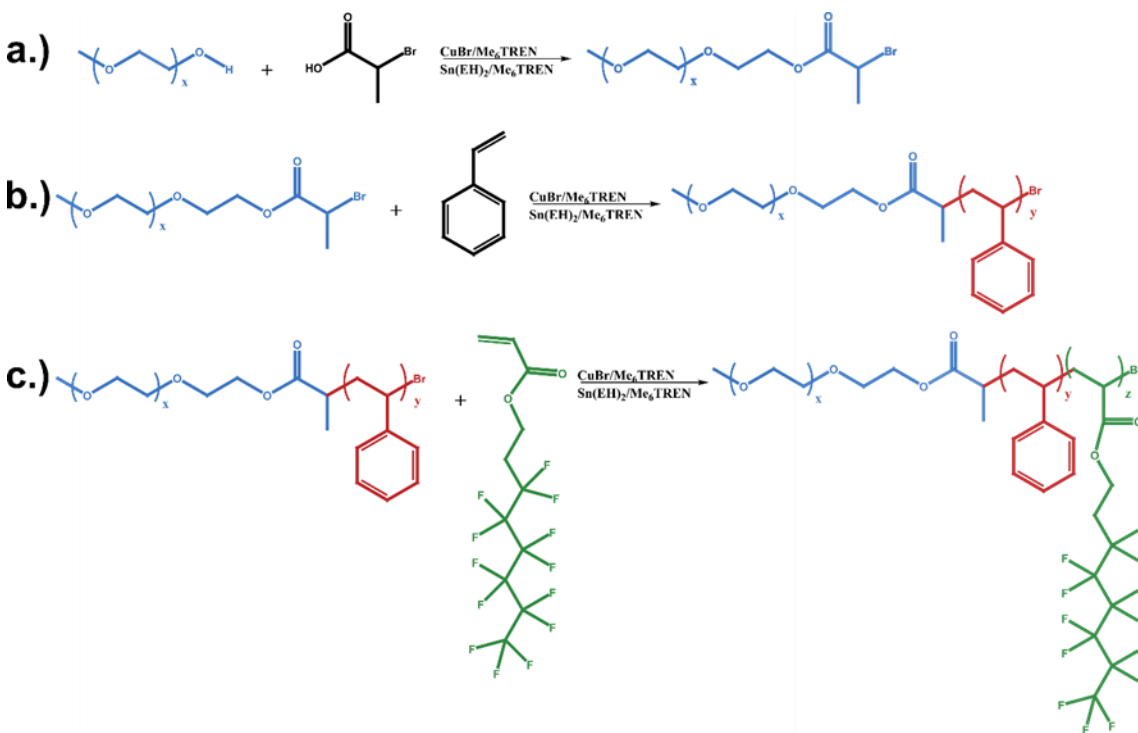

Figure 3.19 Synthetic scheme for the a.) PEO-Br macroinitiator, b.) PEO-b-PS diblock copolymer and c.) PEO-b-PS-b-PFOA triblock terpolymer synthesized using ARGET-ATRP.

titania phase separate from TFT. The QCM results in chapter 2 show that the 100F-NPs have decreased interactions with all of the molecules screened. Solubility experiments confirm this behavior as the 100F-NPs are only soluble in fluorinated solvents, so they are not a viable option for multimodal coassembly. The 75F-NPs had enhanced interactions (Figure 2.17 and 2.18) with small molecules and these NPs exhibit solubility

in solvents like THF. Combining the BCP coassembly results with the QCM experiments point to the 75F-NPs as the ideal option for multimodal coassembly as the fluorine content is enough to assemble them in the PFOA domain while the solubility is enhanced by the mixed ligand shell.

Multimodal coassembly experiments were conducted using an amphiphilic PEO-*b*-PS-*b*-PFOA triblock terpolymer with a was synthesized using ARGET-ATRP (Figure 3.19). The triblock terpolymer was designed to incorporate a hydrophilic, lipophilic, and fluorophilic block in a non-frustrated system which should exhibit strong microphase separation. The synthetic procedure was straight forward and involved minimal steps. First a hydrophilic PEO macroinitiator was synthesized using a Steglich esterification between 2-bromopropionic acid and a commercially available 5,000 g/mol PEO end capped with an alcohol. The resulting PEO macroinitiator has the same initiator groups used to synthesize the PS macroinitiator shown in Figure 3.3. Using the same polymerization method, the PS block was grown off of the PEO macroinitiator to generate a PEO-*b*-PS BCP end capped with a bromine. Finally, the PFOA block was grown off of the PEO-*b*-PS macroinitiator following the exact same procedure used to make the PS-*b*-PFOA diblock. NMR and GPC were used to confirm the synthesis of the PEO-*b*-PS-*b*-PFOA triblock terpolymer (Figure 3.20). ARGET-ATRP afforded control over the M_n and Đ (Table 3.1 and Figure 3.20). NMR analysis shows successful growth of the PS from the PEO macroinitiator as the characteristic peaks of the aromatic phenyl ring appear between 6.5-7.3 ppm (Figure 3.20b). GPC confirmed the growth as there is a large shift to a faster retention time from the PEO (blue) to the PEO-*b*-PS (red), respectively. PFOA growth was confirmed by the characteristic proton signals of the

122

acrylate tail at 2.5 and 4.25 ppm, respectively. GPC analysis shows a slight shift to faster retention times after growth of the PFOA block (green). The total Mn = 35,821 g/mol with 5,000 g/mol PEO, 22,704 g/mol PS, and 8,117 g/mol PFOA, respectively. That corresponds to a weight fraction of 14% for PEO, 63% PS, and 23% PFOA, respectively.
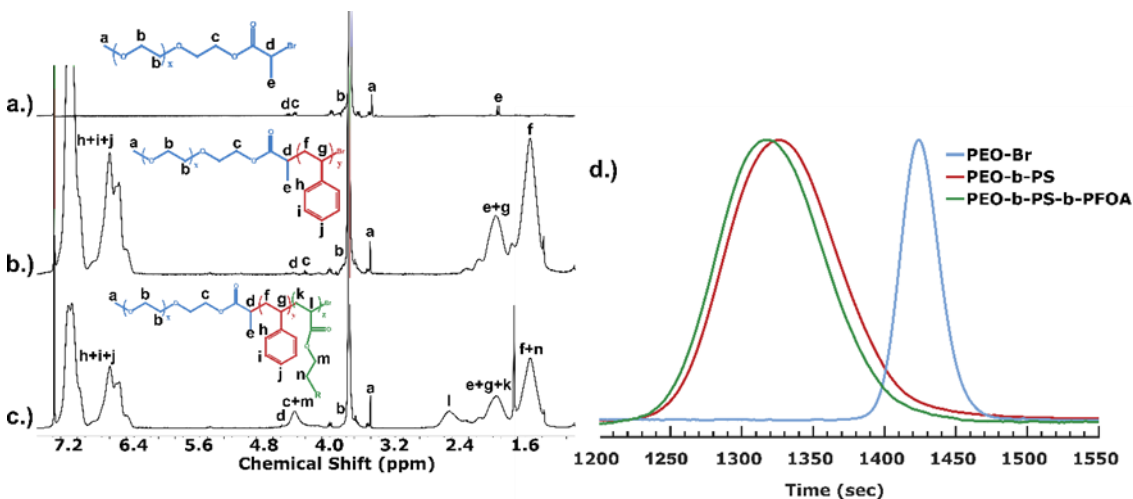

Figure 3.20 NMR spectra for the a.) PEO-Br macroinitiator, b.) PEO-*b*-PS diblock copolymer, c.) PEO-*b*-PS-*b*-PFOA triblock terpolymer where R = C_6F_{13}, and d.) GPC trace for the PEO-Br macroinitiator, PEO-*b*-PS diblock copolymer, and PEO-*b*-PS-*b*-PFOA triblock terpolymer.

The immiscibility of hydrophilic, lipophilic, and fluorophilic materials make solvation in a simple organic solvent non trivial. The PEO-*b*-PS-*b*-PFOA is soluble in select solvents such as THF and TFT. However, if TFT is used the hydrophilic titania precipitates from solution upon dropwise addition. If THF was used as the solvent the highly perfluorinated ML-FNPs precipitated from solution. To overcome the solvation limitations ML-FNPs with a significant percentage of DDT were employed as enhanced interactions of these particles were documented in previous studies.[37] The 75F-NPs were chosen as the incorporation of just 25% of the oily DDT ligand greatly enhances solubility in the THF while maintaining the fluorophobic interactions observed in the coassembly experiments with the PS-*b*-PFOA diblock copolymer. THF was able to

disperse the PEO-*b*-PS-*b*-PFOA, titania, and 75F-NPs into a homogeneous solution with a slight red tint. No phase separation was observed for this mixture indicating that the 75F-NPs are able to enhance the solubility for multimodal coassembly.

The solution of the PEO-*b*-PS-*b*-PFOA, titania, and 75F-NPs was cast, and the assembly behavior was analyzed using SAXS. Titania was chosen as the it functions as a hydrogen bonding donor and will coassemble with the hydrogen bond accepting PEO block. This will function as the hydrogen bond donor-acceptor part of coassembly. The titania is also higher Z than the polymer domains which will provide added contrast to the PEO block. Although it is higher Z there is still a significant difference between Ti and Au which will provide contrast between the two inorganic populations. This will be needed to ensure proper identification of the domains and the locations of the inorganic NPs. Thin films of the PEO-*b*-PS-*b*-PFOA, titania, and 75F-NPs were originally prepared in a similar procedure with the PS-*b*-PFOA films. However, the hydrofluoric etching procedure that is used to dissolve the silica resulting in "lift off" of the thin film also dissolved the titania NPs resulting in destruction of the structure and loss of contrast. Therefore, bulk films were cast to avoid the use of hydrofluoric acid. SAXS of the resulting bulk films point to the first successful multimodal coassembly (Figure 3.21). The as cast polymer film has a sharp primary scattering feature with a d-spacing of 32.5 nm and a subtle secondary shoulder (green curve). This suggests microphase separation of the three polymer blocks in the as-cast film. Since there are only two scattering features the morphology of the bulk film cannot be fit. Upon incorporation of the 75F-NPs the primary scattering feature shifts to a higher d-spacing of 34.5 nm without diminishing the primary scattering feature or the secondary shoulder (red curve). This
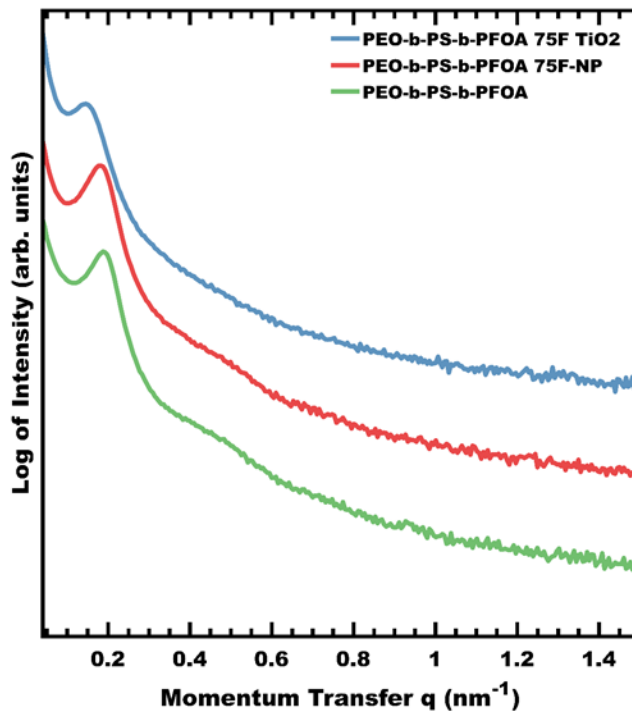
Figure 3.21 SAXS data of the PEO-*b*-PS-*b*-PFOA polymer film, PEO-*b*-PS-*b*-PFOA + 75F-NP film, and PEO-*b*-PS-*b*-PFOA + 75F-NP + TiO$_2$ composite films. A shift of the primary scattering feature to lower q indicates a growing d-spacing.

suggests inclusion of the 75F-NPs into the BCP domain with no disruption in the BCP

ordering. This was expected as the 75F-NPs successfully coassembled with the PS-*b*-

PFOA system. Finally, when both the 75F-NPs and the titania are incorporated the

primary scattering feature shifts to a higher d-spacing of 41.7 nm with slight weakening

of the primary scattering feature and loss of the secondary feature (blue curve). The

primary scattering feature suggests that the coassembly of both inorganic NPs does not

disrupt the BCP ordering. The large increase in the d-spacing is suggestive of a large

change in the domain sizes. This would be consistent with successful coassembly as

numerous studies have shown large changes in the d-spacing and a resulting change in

125

the morphology of the system.[23] These results are very promising as two inorganic materials with highly dissimilar chemistry were combined with an amphiphilic terpolymer containing three immiscible polymer blocks. Being able to solvate this system without phase separation and loss of the BCP scattering features is a very promising sign pointing to successful coassembly. In order to validate the SAXS results films are being sectioned for TEM since the etching method destroys the films. Images of the films are currently being taken.

3.5 Conclusion

The fluorophobic effect and its influence on the dispersion and coassembly of ML-FNPs with varying amount of fluorine in the ligand shell was systematically studied with homopolymer, diblock copolymer, and triblock terpolymer systems. Dispersion experiments in the H-PS revealed aggregation of ML-FNPs with as little as 25% PFOT in the ligand shell at NP loadings of just 0.05 vol.%. The addition of PFOT creates a chemical dissimilarity inducing the fluorophobic effect pushing the NPs from the H-PS. The dispersion and loading percentage of the ML-FNPs in the H-PFOA increased only when the ligand shell was predominately fluorinated as even 7% DDT lead to aggregation at moderate loading percentages. Form factor scattering features for the perfluorinated NPs in the H-PFOA show a favorable match between the PFOT ligand ans the H-PFOA which suggests the fluorophobic effect has an attractive force between the inorganic NP and fluorinated polymer. Coassembly experiments of the ML-FNPs with the PS-*b*-PFOA diblock copolymer further support the observations of incompatibility with the H-PS and greater compatibility with the H-PFOA. ML-FNPs containing just 25% PFOT in the ligand shell dispersed in the BCP assembling at the interface of the

126

polymer domains while the purely lipophilic NPs were expelled from both domains and formed large aggregates. Here, minor amounts of PFOT are able to assemble the NPs with the BCP but are insufficient in assembling the NPs to the correct polymer domain. As the amount of PFOT was increased to 75% the NPs were observed assembling inside the PFOA domain pointing to successful coassembly as no NPs were observed inside the PS domain. Similar behavior was observed for the 98F-NPs. Remarkably, the fluorophobic effect can be used as an interaction to coassemble particles with small ligands and without added small molecules. Finally, preliminary multimodal coassembly experiments of the ML-FNPs with hydrophilic titania and an amphiphilic PEO-*b*-PS-*b*-PFOA triblock terpolymer were enabled by using the ML-FNPs. The use of 75F-NPs overcomes the solubility limitations of fluorinated materials and has enough PFOT to facilitate the fluorophobic effect. A homogeneous mixture of the terpolymer and the two chemically dissimilar inorganic materials was achieved in THF and films show no indications of macrophase separation. SAXS experiments suggest the first successful multimodal coassembly as the primary scattering feature is preserved while shifting from 32.5 nm to 41.7 nm upon addition of both the TiO_2 and 75F-NPs. TEM experiments of the terpolymer films are ongoing.

3.6 References

1. Ma, M.; Hill, R. M. *Curr. Opin. Colloid Interface Sci.* **2006**, *11*, 193–202.

2. Pagliaro, M.; Ciriminna, R. *J. Mater. Chem.* **2005**, *15*, 4981–4991.

3. Dolbier, W. R. *J. Fluor. Chem.* **2005**, *126*, 157–163.

4. Percec, V.; Johansson, G.; Ungar, G.; Zhou, J. *J. Am. Chem. Soc.* **1996**, *118*, 9855–9866.

5. Johansson, G.; Percec, V.; Ungar, G.; Smith, K. *Chem. Mater.* **1997**, *9*, 164–175.

6. Percec, V.; Glodde, M.; Johansson, G.; Balagurusamy, V. S. K.; Heiney, P. A. *Angew. Chemie Int. Ed.* **2003**, *42*, 4338–4342.

7. Houbenov, N.; Milani, R.; Poutanen, M.; Haataja, J.; Dichiarante, V.; Sainio, J.; Ruokolainen, J.; Resnati, G.; Metrangolo, P.; Ikkala, O. *Nat. Commun.* **2014**, *5*, 4043.

8. Shen, J.; Hogen-Esch, T. *J. Am. Chem. Soc.* **2008**, *130*, 10866–10867.

9. Thomas, E. L.; Anderson, D. M.; Henkee, C. S.; Hoffman, D. *Nature* **1988**, *34*, 598–601.

10. Bates, F. S. *Science* **1991**, *251*, 898–905.

11. Matesen, M. W.; Bates, F. S. *Macromolecules* **1996**, *29*, 1091–1098.

12. Hillmyer, M. A.; Lodge, T. P. *J. Polym. Sci. Part A Polym. Chem.* **2002**, *40*, 1–8.

13. Skrabania, K.; Berlepsch, H. V.; Böttcher, C.; Laschewsky, A. *Macromolecules* **2010**, *43*, 271–281.

14. Moughton, A. O.; Hillmyer, M. a.; Lodge, T. P. *Macromolecules* **2012**, *45*, 2–19.

15. Templin, M.; Franck, A.; Du Chesne, A.; Leist, H.; Zhang, Y.; Ulrich, R.; Schädler, V.; Wiesner, U. *Science* **1997**, *278*, 1795–1798.

16.Warren, S. C.; Messina, L. C.; Slaughter, L. S.; Kamperman, M.; Zhou, Q.; Gruner, S. M.; DiSalvo, F. J.; Wiesner, U. *Science* **2008**, *320*, 1748–1753.

17. Lin, Y.; Daga, V. K.; Anderson, E. R.; Gido, S. P.; Watkins, J. J. *J. Am. Chem. Soc.* **2011**, *133*, 6513–6516.

18. Yang, P.; Zhao, D.; Margolese, D. I.; Chmelka, B. F.; Stucky, G. D. *Nature* **1998**, *396*, 152.

19. Fan, J.; Boettcher, S. W.; Stucky, G. D. *Chem. Mater.* **2006**, *18*, 6391–6396.

20. Boettcher, S. W.; Fan, J.; Tsung, C.-K.; Shi, Q.; Stucky, G. D. *Acc. Chem. Res.* **2007**, *40*, 784–792.

21. Liang, C.; Hong, K.; Guiochon, G. A.; Mays, J. W.; Dai, S. *Angew. Chem. Int. Ed.* **2004**, *43*, 5785–5789.

22. Meng, Y.; Gu, D.; Zhang, F.; Shi, Y.; Cheng, L.; Feng, D.; Wu, Z.; Chen, Z.; Wan, Y.; Stein, A.; Zhao, D. *Chem. Mater.* **2006**, *18*, 4447–4464.

128

23. Stefik, M.; Mahajan, S.; Sai, H.; Epps, T. H.; Bates, F. S.; Gruner, S. M.; DiSalvo, F. J.; Wiesner, U. *Chem. Mater.* **2009**, *21*, 5466–5473.

24. Stefik, M.; Wang, S.; Hovden, R.; Sai, H.; Tate, M. W.; Muller, D. A.; Steiner, U.; Gruner, S. M.; Wiesner, U. *J. Mater. Chem.* **2012**, *22*, 1078–1087.

25. Balazs, A. C.; Emrick, T.; Russell, T. P. *Science.* **2006**, *314*, 1107-1110.

26. Bockstaller, M. R.; Lapetnikov, Y.; Margel, S.; Thomas, E. L. *J. Am. Chem. Soc.* **2003**, *125*, 5276–5277.

27. Chiu, J. J.; Kim, B. J.; Yi, G.-R.; Bang, J.; Kramer, E. J.; Pine, D. J. *Macromolecules* **2007**, *40*, 3361–3365.

28. Zhao, Y.; Thorkelsson, K.; Mastroianni, A. J.; Schilling, T.; Luther, J. M.; Rancatore, B. J.; Matsunaga, K.; Jinnai, H.; Wu, Y.; Poulsen, D.; Fréchet, J. M. J.; Paul Alivisatos, A.; Xu, T. *Nat. Mater.* **2009**, *8*, 979.

29. Kao, J.; Xu, T. *J. Am. Chem. Soc.* **2015**, *137*, 6356–6365.

30. Liu, R.; Shi, Y.; Wan, Y.; Meng, Y.; Zhang, F.; Gu, D.; Chen, Z.; Tu, B.; Zhao, D. *J. Am. Chem. Soc.* **2006**, *128*, 11652–11662.

31. Warren, S. C.; DiSalvo, F. J.; Wiesner, U. *Nat. Mater.* **2007**, *6*, 156–161.

32. Dass, A.; Guo, R.; Tracy, J. B.; Balasubramanian, R.; Douglas, A. D. Murray, R. J. *Langmuir* **2008**, *1995*, 310–315.

33. Uzun, O.; Hu, Y.; Verma, A.; Chen, S.; Centrone, A.; Stellacci, F. *Chem. Commun.* **2008**, 2, 196–198.

34. Bidoggia, S.; Milocco, F.; Polizzi, S.; Canton, P.; Saccani, A.; Sanavio, B.; Krol, S.; Stellacci, F.; Pengo, P.; Pasquato, L. *Bioconjugate Chem.* **2017**, *28*, 43–52.

35. Niu, H.; Wang, S.; Zhou, Z.; Ma, Y.; Ma, X.; Cai, Y. *Anal. Chem.* **2014**, *86*, 4170–4177.

36. Kuna, J. J.; Voïtchovsky, K.; Singh, C.; Jiang, H.; Mwenifumbo, S.; Ghorai, P. K.; Stevens, M. M.; Glotzer, S. C.; Stellacci, F. *Nat. Mater.* **2009**, *8*, 837–842.

37. Marsh, Z. M.; Lantz, K. A.; Stefik, M. *Nanoscale* **2018**, *10*, 19107–19116.

38. Stefik, M.; Sai, H.; Sauer, K.; Gruner, S. M.; Disalvo, F. J.; Wiesner, U. *Macromolecules* **2009**, 42, 6682-6687

39. The Spin Coater Online, http://www.stefikgroup.com/spin-coater/, **2017**.

129

40. Jakubowski, W.; Min, K.; Matyjaszewski, K. *Macromolecules* **2006**, *39*, 39–45.

41. Lantz, K. A.; Sarkar, A.; Littrell, K. C.; Li, T.; Hong, K.; Stefik, M. *Macromolecules* **2018**, *51*, 6967–6975.

42. Welch, M. E.; Ober, C. K. *ACS Macro Lett.* **2013**, *2*, 241–245.

43. Sawyer, L. C., Grubb, D. T., Meyers, G. F., Eds.; Springer New York: New York, NY, 2008; pp 130–247

CHAPTER 4

SUMMARY AND SUGGESTIONS FOR FUTURE WORK

4.1 Summary

The overarching goal of this dissertation was to control two populations of chemically dissimilar nanoparticles using fluorophobic interactions alongside hydrogen bonding interactions. Fluorophobic interactions were chosen as fluorinated materials are immiscible with hydrophilic materials and lipophilic materials leading to segregation even with minimal fluorination. The fluorophobic effect is also selective as shown by the numerous examples of selective segregation of fluorinated materials into the same domain in preexisting literature. To prove that the fluorophobic effect would be a new handle for BCP coassembly where hydrophobic forces had failed a few key questions needed to be addressed. First, can the solubility of fluorinated NPs be controlled while tuning the fluorophobic nature of the NPs. Second, is the interaction selective in that fluorinated NPs will go to the correct domain, and third can the fluorophobic effect coassembled the fluorinated NPs to the correct polymer domain.

The solution to the solubility was addressed in chapter 2 using ML-FNPs. The use of a mixed ligand shell enables hybrid behavior as the ligand shell is the interface between the metal NP and the local environment. By adjusting the composition, the chemical nature and morphology are altered. Both significantly impact the overall behavior so being able to understand the roles each have is crucial. Many methodologies currently exist for elucidating the structure of the ligand shell, but the field lacks quantitative experimental methods to probe the behavior. If the fluorophobic effect and the solubility are to be tuned and controlled a new highly quantitative method for determining the behavior of the NPs was needed. To this end, a QCM based method was

employed that was able to measure the mass uptake of various molecular vapors without the need for tedious solvation measurements. The impact that the ligand shell morphology had on the behavior was able to be determined when paired with a method that can elucidate the morphology. Here, a ^{19}F NMR method used as the fluorinated PFOT ligand is highly sensitive to the molecular environment. The mixture of PFOT and DDT used for the ML-FNPs formed patchy morphologies when the PFOT percentage was under 30% and over 70% of the ligand shell, respectively. The composition range that spanned between 30-70% PFOT was found to formed stripe-like domains.

When the ML-FNPs interacted with the series of molecule vapors the morphology was found to dominate the behavior of the ML-FNPs. The patchy ML-FNPs had enhanced interactions with all of the vapors chosen regardless of fluorine content in the molecular vapor. This was consistent for patchy particles with a minority PFOT and majority PFOT, respectively. ML-FNPs with a stripe-like domain had significantly reduced uptake when compared to the patchy NPs and in most cases had less uptake than the mono-ligand NPs. This is most likely due to the increased interface between the DDT and PFOT restricting the free volume available for the molecule vapor to occupy. This is consistent with the currently hypothesized mechanisms of cavitation and confinement. The non-monotonic behavior observed is consistent with the growing volume of studies focusing on the behavior of ML-NPs. Two key outcomes were achieved during this ML-FNP study. First, the solubility of the fluorinated NPs can be controlled by using ML-FNPs as the addition of an alkyl thiol greatly enhanced the interactions with small molecules even when the ligand shell is predominantly fluorinated. This was a milestone toward multimodal coassembly as the main hurdle was the insolubility of fluorinated

133

materials. Second, the lack of quantitative methods to determine ML-NP behavior is troubling. The development of the QCM based method is a nice addition that can be implemented for most NP-molecule systems providing quantitative feedback.

With a new tool to control and tune the properties of the ML-FNPs in hand the fluorophobic effect as a tool for BCP coassembly was implemented. To do this the ML-FNPs were introduced to a series of polymer environments testing chemical compatibility using dispersion experiments. The polymers were synthesized using ARGET-ATRP which is a well known controlled radical method. Using ARGET-ATRP a H-PS, H-PFOA, PS-*b*-PFOA BCP, and PEO-*b*-PS-*b*-PFOA BCP were successfully synthesized. The most-simple system was the dispersion of the ML-FNPs with varying fluorine content in both the H-PS and H-PFOA as one interaction is being probed; can the fluorophobic effect disperse the NPs in the H-PFOA and can it repel them from the H-PS. In the ML-FNP and H-PS system the NPs aggregated when PFOT was incorporated into the ligand shell. All of the ML-FNPs with low to high fluorine content were repelled from the H-PS at a volume loading percentage of 0.05 vol.%. Thus, the fluorophobic effect does show selectivity as the ML-FNPs are immiscible with the H-PS. In the H-PFOA a very interesting trend was observed, the morphology does not appear to impact the dispersion behavior in the macromolecular environment. Contrary to the hypothesis that the morphology would drastically impact the dispersion and coassembly behavior the composition of the ligand shell was the main influence. The ML-FNPs aggregated in the H-PFOA at loading percentages greater than 0.05 vol.% until the ligand shell was 75% PFOT. Even with 93% PFOT in the ligand shell aggregation occurs at moderate loading percentages. Only when the ligand shell was devoid of DDT did the ML-FNPs disperse at

loading percentages greater than 0.74 vol.%. Thus, the PFOT ligand is chemically compatible with the H-PFOA and there is some attractive interaction as the H-PFOA behaves as a good solvent for the ML-FNPs. This suggested that the fluorophobic effect is selective and the small ligands can coassemble the ML-FNPs into the H-PFOA domain. However, these results contradict the QCM experiments as the morphology appeared to play an insignificant role in the dispersion. This is most likely due to the size of the H-PFOA and rigid fluorinated tails making it difficult to interdigitate with the ligand shell.

Next, coassembly with a BCP system revealed that the fluorophobic effect can be used as a new handle for directing inorganic materials. The ML-FNPs were combined with the amphiphilic PS-*b*-PFOA BCP, the nanocomposite material was analyzed with SAXS and TEM. As expected, the purely hydrophobic 0F-NPs were incompatible with the BCP as large aggregates were formed and expelled from the film. This confirmed previously published results that small hydrophobic ligands are a mismatch for coassembly and are excluded from the BCP system. Remarkably, when fluorination was added to the ligand shell the ML-FNPs were incorporated into the BCP and aggregation was avoided. The 25F-NPs dispersed into the BCP matrix at a 0.50 volume loading percent. Although dispersion in the BCP occurred the 25F-NPs assembled at the interface between the PS and PFOA domain. The incompatibility with both domains cast the 25F-NPs to the interface as the energy for incorporation into either domain would be too high. As the ligand shell became heavily fluorinated coassembly through the fluorophobic effect was finally observed. The 75F-NPs and 98F-NPs coassembled into the BCP and assembled in the PFOA domain. No cross-loading of the NPs into the PS domain was

135

observed in these films as the high fluorine content pushed the NPs away from the PS and away from the interface. This again highlights the strong push to segregate the fluorinated materials. Even with DDT ligand present the high fluorine content of the ligand shell was enough to make the 75F-NPs compatible with the PFOA domain. The results are significant as this is the first documented use of the fluorophobic effect for coassembly, it was accomplished through small ligands, and a donor-acceptor based system was not needed.

Finally, the first ever multimodal coassembly was attempted utilizing the fluorophobic effect alongside hydrogen bonding interactions. Combining the enhanced interactions of patchy ML-FNPs with small molecules and the extensive fluorine content to utilize the fluorophobic effect for coassembly the 75F-NPs were chosen. The 75F-NPs were combined with titania and an amphiphilic PEO-*b*-PS-*b*-PFOA BCP in THF without any macrophase separation occurring. Casting of bulk films revealed that during self-assembly no phase separation occurred as the BCP scattering features were observed in SAXS, The d-spacing of the composite also increased by more than 10 nm indicating incorporation of the inorganics into the BCP domain. These preliminary results suggest that the fluorophobic effect is compatible with hydrogen bonding interactions if a mixed ligand approach is utilized.

4.2 Suggestions for Future Work

The use of ML-FNPs as a method to tune the solubility and fluorophobic effect was successful and the behavior of the NPs was largely influenced by the composition and morphology of the ligand shell. Throughout this thesis the same ligand mixture of the long DDT and short PFOT was used. Here, the longer ligand was hydrophobic while the

136

shorter ligand was fluorinated. As the ligand shell formed patchy and strip-like domains the taller DDT could shield the PFOT from interacting with the local environment by occupying the free volume above the shorter ligand. This heavily influenced the behavior with small molecules. An interesting study would be to reverse the ligand lengths to see if the interactions with small molecules and macromolecules is influenced. A mixture of 1-hexane thiol and 1H,1H,2H,2H-perfluorodecane thiol could be utilized as there is a 4-carbon difference with the fluorinated ligand being taller. Therefore, if this system were to form stripe-like domains the hydrophobic ligand would be shielded from the local environment and these NPs may behave similar to the purely fluorinated NPs. The ability to coassemble with less fluorine content in the ligand shell may be possible although the solubility may be impacted as well. Finally, to round out the study a mixture of 1-octane thiol and PFOT could be used as these ligands have an equal length. These would be expected to form a Janus morphology which should exhibit unique behavior compared to the ML-FNPs used in this study as no stripe-like domains should form. Coassembly studies should show assembly at the interface across all compositions using only small ligands as opposed to grafted polymer ligands.

137

APPENDIX A

CHAPTER 2 SUPPORTING INFORMATION
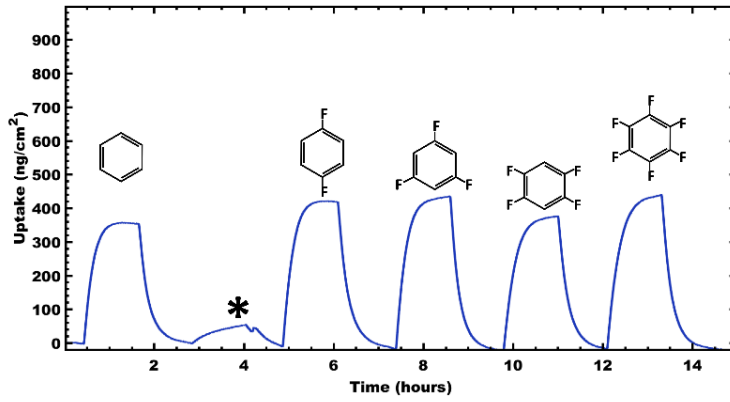
Figure A.1 QCM measurement of a series of molecule vapors using 20F NPs, the asterisk corresponds to a gas line disruption during the experiment.
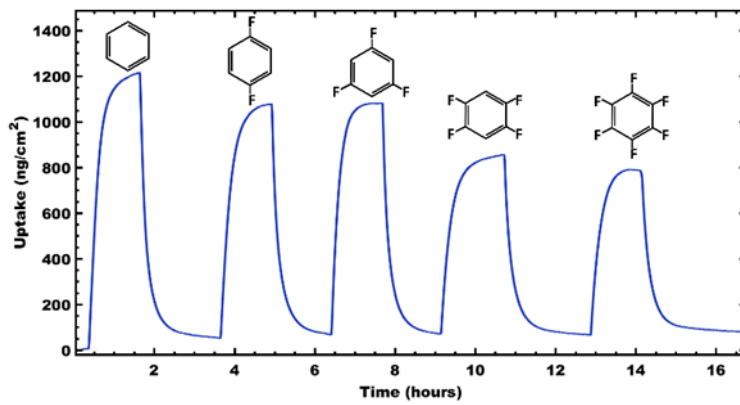
Figure A.2 QCM measurement of a series of molecule vapors using 31F NPs.

139
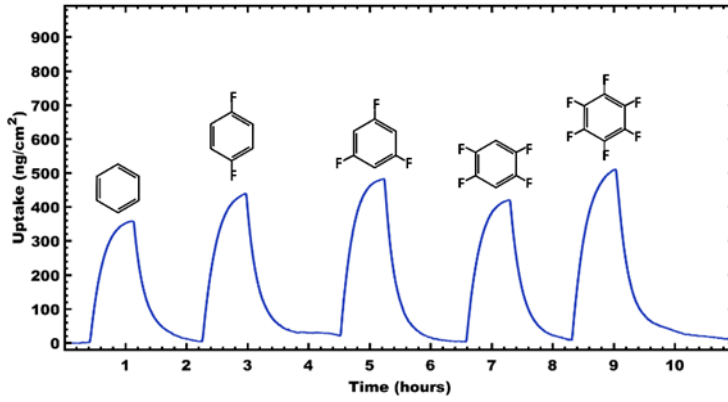
Figure A.3 QCM measurement of a series of molecule vapors using 52F NPs.
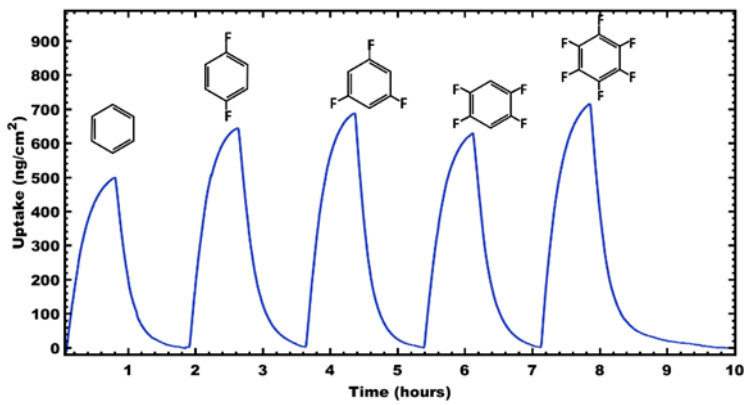
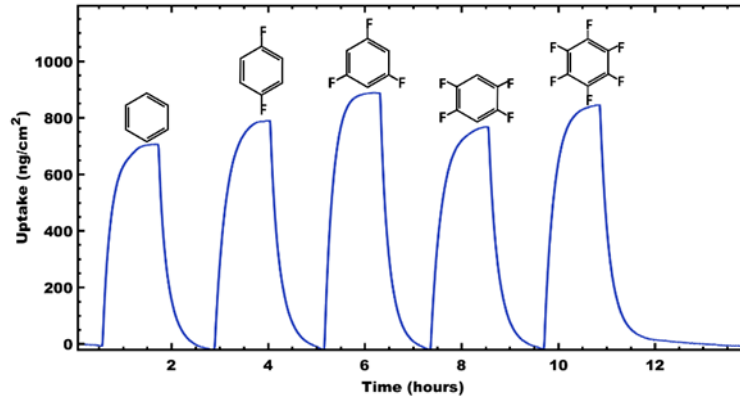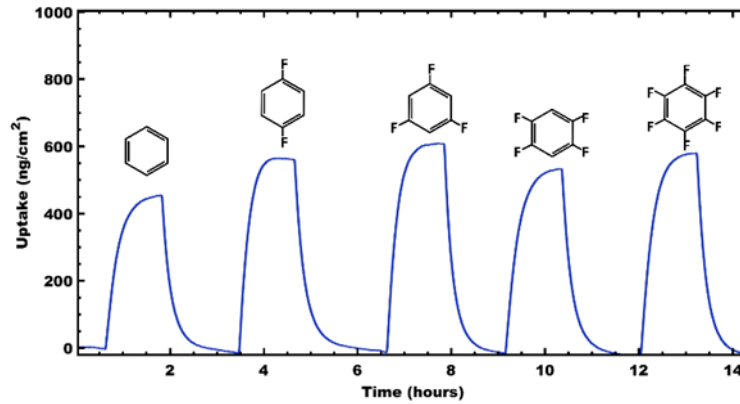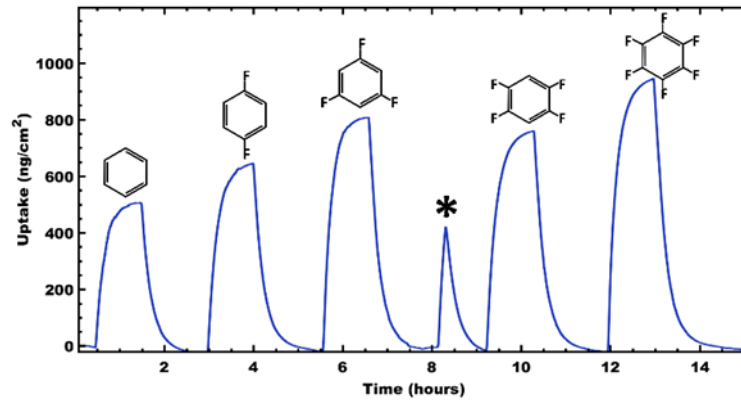Figure A.4 QCM measurement of a series of molecule vapors using 59F NPs.

Figure A.5 QCM measurement of a series of molecule vapors using 73F NPs.

Figure A.6 QCM measurement of a series of molecule vapors using 93F NPs.

141

Figure A.7 QCM measurement of a series of molecule vapors using 100F NPs. The asterisk corresponds to a gas line disruption during the experiment.

APPENDIX B

PERMISSION TO REPRINT

QCM detection of molecule–nanoparticle interactions for ligand shells of varying morphology

In all cases the Ref. XX is the XXth reference in the list of references.

If you are the author of this article you do not need to formally request permission to reproduce figures, diagrams etc. contained in this article in third party publications or in a thesis or dissertation provided that the correct acknowledgement is given with the reproduced material.

Reproduced material should be attributed as follows:

• For reproduction of material from NJC:

[Original citation] - Reproduced by permission of The Royal Society of Chemistry (RSC) on behalf of the Centre National de la Recherche Scientifique (CNRS) and the RSC

• For reproduction of material from PCCP:

[Original citation] - Reproduced by permission of the PCCP Owner Societies

• For reproduction of material from PPS:

[Original citation] - Reproduced by permission of The Royal Society of Chemistry (RSC) on behalf of the European Society for Photobiology, the European Photochemistry Association, and RSC

• For reproduction of material from all other RSC journals:

[Original citation] - Reproduced by permission of The Royal Society of Chemistry

If you are the author of this article you still need to obtain permission to reproduce the whole article in a third-party publication with the exception of reproduction of the whole article in a thesis or dissertation.